The Dissertation Committee for Christopher Scott Reilly certifies that
this is the approved version of the following dissertation:

Scattering of Aligned H_2 from Si(100)

Committee:

_____

Greg O. Sitz, Supervisor

_____

Daniel Heinzen

_____

Michael Downer

_____

Graeme Henkelman

_____

Keji Lai

Scattering of Aligned H_2 from Si(100)

by

Christopher Scott Reilly

Dissertation
Presented to the Faculty of the Graduate School of
The University of Texas at Austin
in Partial Fulfillment
of the Requirements
for the degree of
Doctor of Philosophy

The University of Texas at Austin
December, 2019

Dedicated to Mom and Dad.

Acknowledgements

I would like to acknowledge my advisor Greg Sitz and my lab mate Andy Hutchison for the help they have provided during my doctoral program.

Greg is a remarkably conscientious advisor whose office door is always open; I am happy to admit that I was never able to commiserate with other graduate students when they complained of their advisors' negligence or rudeness. Perhaps more importantly though, Greg is endlessly curious, always welcoming my physics questions with genuine interest (no matter their relevance to the research at hand!). It is inspiring to observe how after decades in physics his joy for the subject seems in no way diminished.

Andy is an unerringly pleasant lab mate – a welcome antidote to the often frustating and isolating aspects of experimental physics. Andy embodies scientific virtue and diligence, prioritizing evidence and sound arguments without interference from the ego in the effort to really get to the bottom of things. Through Andy I am inspired to attack unfamiliar problems with fearlessness.

Scattering of Aligned H_2 from Si(100)

Christopher Scott Reilly, Ph.D.

The University of Texas at Austin, 2019

Supervisor: Greg Sitz

The field of chemical dynamics seeks to understand the path to reaction. What are the roles played by the different degrees of freedom possessed by the reactants? In surface physics/chemistry the reaction under consideration is often unimolecular, i.e. the adsorption of a molecule onto or its desorption from some surface. In this case the participating degrees of freedom are the translation, vibration, and rotation of the impinging/departing molecule. The studies described in this dissertation focus on the rotational degrees of freedom. Using optical excitation it is possible to both prepare an aligned ensemble of molecules and detect changes in the ensemble's alignment induced by scattering from the surface. From these changes information is obtained about the nature of torques applied to a molecule along the path to reaction.

The particular system studied is a hydrogen molecule (H_2) scattering from a single crystal silicon surface oriented in the (100) direction. In contrast with the metal surfaces typically studied in gas-surface dynamics, the silicon surface exhibits highly directional (covalent) bonding, which may be expected to give rise to strong coupling between the surface and an impinging molecule's angular momentum. Our experiment measures the likelihood of a *reorienting* collision, where the magnitude of the molecule's angular momentum is preserved but its direction changed.

An initial laser pulse transforms a beam of H_2 molecules from a supersonic molecular beam originating as an unaligned ensemble in the $j = 1$ rotational state to an aligned ensemble the $j = 3$ state. The excited molecules are aligned in a plane determined by the polarization of the exciting laser radiation so that ensembles can be prepared with their bonds lying preferentially parallel (helicoptering) and perpendicular (cartwheeling) to the surface plane. The rotationally excited molecules are then allowed to scatter from the Si(100) surface, and the alignment of the scattered $j = 3$ molecules is resolved by measuring modulation in the ionization yield with the polarization of the ionizing radiation from a second laser pulse. By comparing

the results of this procedure obtained with the ionizing laser running parallel to the Si(100) dimers to those obtained with the laser running at 45°, we can discriminate between changes to alignment originating from corrugation in the molecule-surface potential with the bond's polar (θ) and azimuthal angle (ϕ) relative to the surface normal.

The results of the experiment indicate substantial but not complete reduction in alignment of the scattered molecules. Quantifying the alignment using the cylindrically symmetric component of the quadrupole moment of the ensemble's bond angle probability distribution, we find alignment survival ratios ranging between 50-70%, with our measurements indicating better survival (60-70%) for the cartwheeling molecules than the helicopters (50-60%). Futher, measurements at different azimuthal surface orientations of the scattered alignment of molecules impinging with cartwheeling alignment yield a complete determination of the scattered bond angle distribution. The results indicate a weak corrugation in the molecule-surface potential with the bond angle's azimuthal coordinate.

Quantum mechanical scattering calculations performed by the author using a model potential developed by Brenig and Pehlke [*Prog. Surf. Sci.*, **83**, 263 (2008)] are also presented. The model is found to predict qualitatively different alignment survivals than are observed in our measurements, though in both experiment and theory the degree realignment is found to be substantial.

Contents

List of Figures

List of Tables

List of Symbols

- B: the rotational constant (60.853cm^{-1} for H_2)

- j: total angular momentum quantum number

- LEED: low energy electron diffraction

- m: magnetic quantum number

- MCP: microchannel plate

- ϕ: azimuthal angle

- REMPI: resonantly enhanced multi-photon ionization

- ρ: density operator, or a particular multiplet of definition angular momentum

- s: reaction path coordinate

- $S(\theta)$: the measured ionization signal as a function of the probe polarization angle

- SMB: supersonic molecular beam

- SRP: stimulated Raman pumping

- SRE: stimulated Raman emission

- θ: polar angle, or, equivalently, the angle of the probe laser polarization.

- z: molecular-surface distance

Chapter One: Introduction

Presented in the dissertation are measurements of the alignment of H_2 molecules scattered from the Si(100) surface for multiple incident molecular alignments. The work is organized into six chapters.

Following this brief outline, we begin in Chapter 2 with a simplified description of our measurement so that the reader may have a firm grasp of the larger picture as we move on to the finer details. In the remaining sections of the chapter we then break down each of the main components of the experiment. The chapter also serves as an introduction for our starring actors – the H_2 molecule and the Si(100) surface.

To provide context and motivation for the work presented here we move on in Chapter 3 to a survey of gas-surface dynamics, focusing primarily on the role played by angular momentum. In Chapter 4 we treat the subject of quantum mechanical angular momentum, developing concepts that will be used heavily in the interpretation of our results.

In Chapter 5 we continue the discussion from the previous chapter, focusing on the exhange of angular momentum between the molecule and surface. We first work out the implications of surface symmetry on the form of the angular momentum exchange, and then describe some quantum dynamics calculations for H_2/Si(100) system performed by the author, arriving at a prediction for the alignment of scattered molecules under the various initial conditions studied in our experiment.

Finally in Chapter 6 we present the measurements from our experiment. These measurements are then analyzed, yielding our main results. We close the dissertation with a brief discussion of these results, along with some suggestions for further research. A few special topics are addressed in the appendices.

Chapter Two: Experimental

In the community of gas-surface dynamics our experiment would be classified as "state-to-state" or "pump-probe". These experiments seek to uncover facets of the molecule-surface interaction that are normally obscured by the broad spread in initial states employed and final states produced in a typical experiment. The strategy is to prepare the system in a well defined state and to take measurements that are sensitive to a particular final state. The results from these experiments more clearly expose the roles played by the different degrees of freedom in the process being studied [1].

In figure 2.1 we present a simplified conceptual diagram of our measurement to illustrate the state-to-state nature of our experiment. It is clear from the diagram and accompanying caption that our experiment consists of four main components:

- the beam of hydrogen molecules,

- the silicon surface from which the molecules scatter,

- a pumping laser exciting the incident molecules,

- a probe laser (and detection electronics) to measure the scattered molecules.

In the following sections we describe each of these components.

2.1 The H_2 Supersonic Molecular Beam

The molecules studied in our scattering experiment originate from a supersonic molecular beam (SMB)[1]. An SMB is generated by a high pressure gas expanding into a low pressure volume. During the initial phase of the expansion, molecules collide in such a way as to produce a narrow velocity distribution peaked about the direction of expansion. Beyond a certain radius (known as the quitting surface), intermolecular collisions cease to occur, so that SMBs can propagate over long distances with essentially zero scattering losses. The average translational energies of the molecules

---

[1] In chapter 3 we survey a number of experiments using some combination of state preparation and/or state detection.
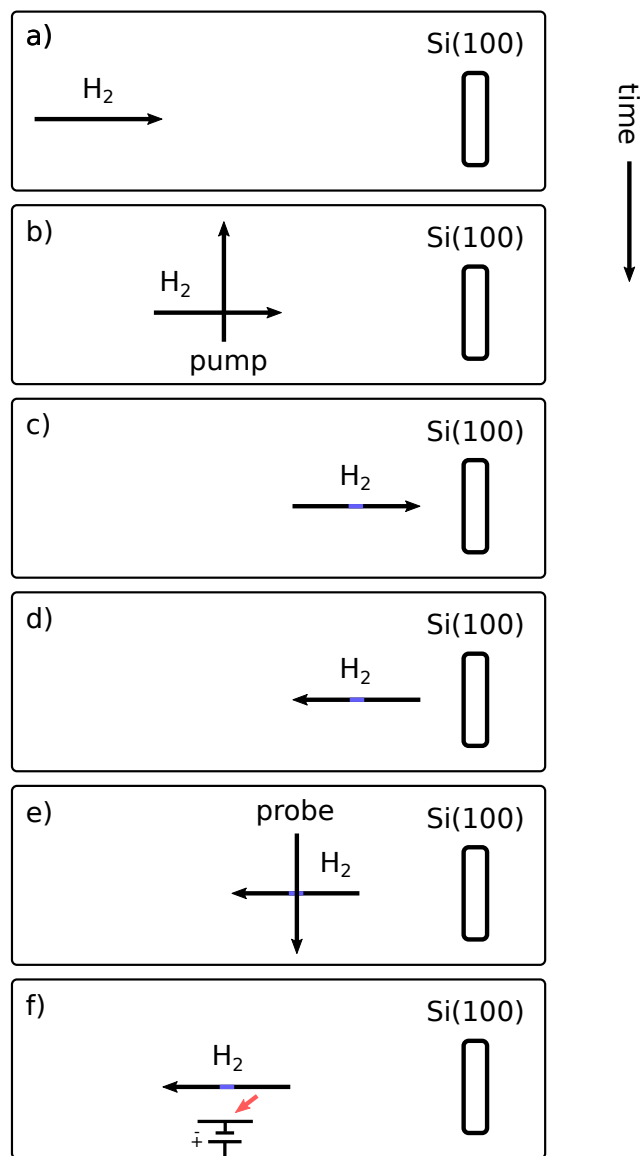
Figure 2.1: Simplified description of our experiment. The experiment begins in **a)** with a beam of hydrogen (H_2) molecules impinging on a silicon surface oriented in the (100) direction. The firing of a short (5 ns) "pump" laser (**b)**) is timed so to intercept the molecular beam, exciting the molecules to a higher rotational state ($j = 1 \rightarrow 3$). The excited molecules are represented by the blue segment in panel **c)**. The beam then scatters from the surface in **d)**, at which point another short "probe" laser is fired (**e)**) which is timed to overlap with the portion of the beam excited by the pump laser. This laser selectively ionizes molecules in the higher rotational state. Finally in **f)** the ionized molecules (shown in red) are collected using an electric field.
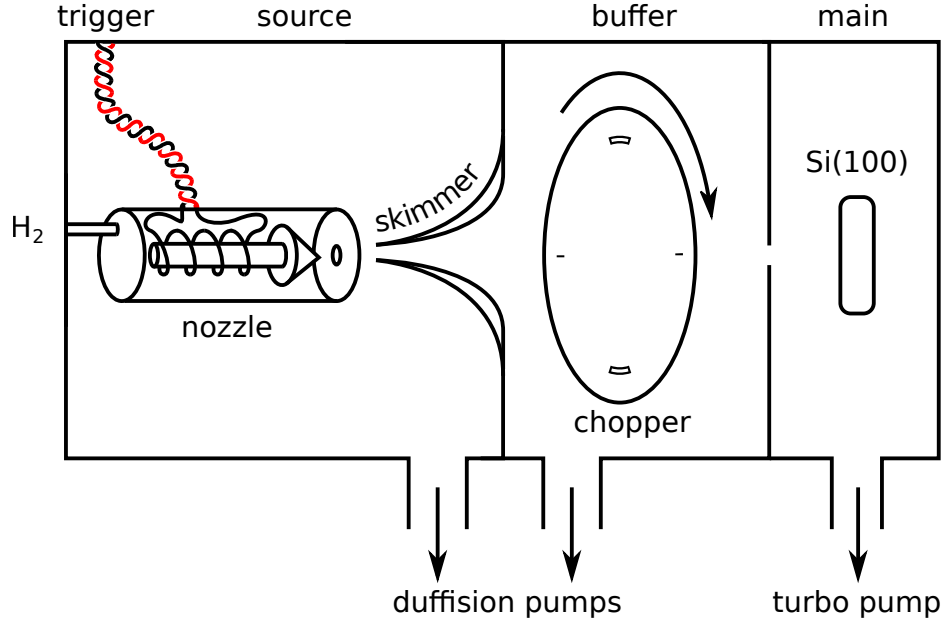
Figure 2.2: A schematic diagram of our molecular beam source. The nozzle holds a high pressure (4-5 bar) reservoir of H_2. A spring (not shown) supplies the force necessary to maintain a good seal between the plunger and the nozzle aperture. A pulse of gas escapes into the vacuum from the reservoir when the magnetically permeable plunger is briefly ($\approx 1ms$) retracted by pulsing current to a surrounding coil. A skimmer is placed close (≈ 1cm) to the nozzle to separate out the molecules traveling in the direction of the surface. A rapidly (200 Hz) rotating chopper wheel selects out the desired segment (μs) of the beam pulse. The chopped molecular beam then propagates into the main chamber.

are also increased above their $\frac{3}{2}kT$ equilbrium value. For instance, using pump-probe time of flight we measure a velocity of ≈ 2900m/s, which in turn implies a kinetic energy of 80meV, well in excess of the ≈ 40meV of kinetic energy expected for molecules at room temperature.

A schematic of our SMB apparatus appears in figure 2.2. The nozzle[2] is pulsed for the purposes of reducing the gas load on the vacuum pumps. Most of the gas released into the source chamber while the plunger is open does not end up in the collimated molecular beam entering the main chamber, and acts as a large undesirable

---

[2]Miniature High Speed Vacuum Dispense Valve – Parker Fluidics

background. The skimmer acts to shield the portion of the beam heading towards the surface from collisions with this background, and also acts as a constriction, preventing background from diffusing into the main chamber[3].

The chopper wheel for the purposes of our experiment serves essentially as an extra constriction to reduce the amount of contamination (primarily water) coming from the nozzle from reaching the sample, allowing us to increase the time between cleanings of the sample (section 2.2).

The firing of the nozzle is timed so that the desired portion of the SMB passes through a chopper slit. The phase of the chopper wheel is monitored using a photogate sandwiched around the edge of the wheel that activates when a slit rotates past. Rough synchronization can be achieved by monitoring the signal at the 2 AMU peak on a quadrupole mass spectrometer located in the main chamber on the beam axis as the delay between the nozzle and the photogate signal is scanned.

Note however that it is not always the brightest portion of the beam which is most desirable. In figure 2.3 we've sketched out a plot derived from measurements of the density in the $j = 1$ and $j = 3$ rotational states (section 2.4) as the nozzle delay is increased. Due to complex dynamics occurring in the expansion of the pulsed beam, both profiles exhibit pronounced structure, and, moreover, the structure is j-dependent. To determine the optimal nozzle delay, we first note that in our experiment we produce aligned $j = 3$ molecules by optical excitation of molecules from highly populated $j = 1$ level. Any initial population of the $j = 3$ rotational level before the pumping stage then acts as unaligned background, degrading the signal. It is therefore advantageous to time the chopper to select regions of SMB with *lower* $j = 1$ density if it is accompanied by an even larger decrease in $j = 3$.

One can also further improve the $j = 1 : j = 3$ signal to background by increasing the nozzle pressure[2]. While most molecules efficiently transfer their rotational energy into translation during the expansion, hydrogen molecules, owing to their large rotational energy level spacing, do not. To improve the rotational cooling rate it is necessary to increase the rate of intermolecular collisions, which is accomplished by increasing the initial density (i.e. pressure) in the reservoir.

---

[3] This strategy of separating the source chamber from the main (or "science") chamber by an intermediate volume that is actively pumped is known as differential pumping. The effectiveness goes roughly as the ratio of the pumping speed (~ 100l/s) to the conductance of the constriction, which for the skimmer is on the order of .01 l/s. This allows us to maintain a base pressure in the main chamber lower than 10^{-10}torr during operation of the pulsed nozzle.
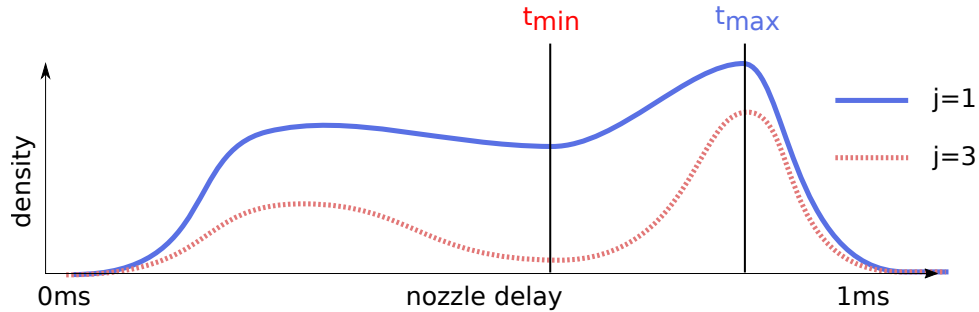
Figure 2.3: Sketch of the measured density of the SMB at the $j = 1$ and $j = 3$ rotational states vs. nozzle delay. The density was measured using REMPI spectroscopy, discussed in section 2.4. The times $t_{\max}$ and $t_{\min}$ indicate the delays of maximum $j = 1$ density and minimum $j = 3$ density respectively.

2.2 The Si(100) Surface

2.2.1 The Si(100) reconstruction

The silicon unit cell is shown in figure 2.4a. Silicon forms a diamond lattice, named after the phase of carbon, the element appearing directly above silicon in the periodic table. If the silicon solid is cleaved along the plane containing the (010) and (001) directions, the Si(100) surface is formed.

By inspection of figure 2.4a, we find that in forming the surface two of the original four bonds of each surface atom are broken. Such a scenario would be expected to be highly reactive. To increase its stability, the surface undergoes a *reconstruction* whereby the atoms assume an arrangement different from how they find themselves in the bulk.

Specifically, atoms tilt towards one of the two equivalent nearest neighbors not sharing the same backbone (c.f. caption of figure 2.4a, forming surface atom pairs known as "dimers". Atoms on the same backbone tilt in the same direction, so that the dimers form rows (see figure 2.5a). This is known as the Si(100)–(2x1) reconstruction, since the periodicity along a dimer row is one surface atom while the periodicity normal to the rows is two surface atoms.

If the surface was formed instead by the plane of atoms lying just beneath the surface (i.e. the lower backbone atoms), inspection of the bonding structure suggests
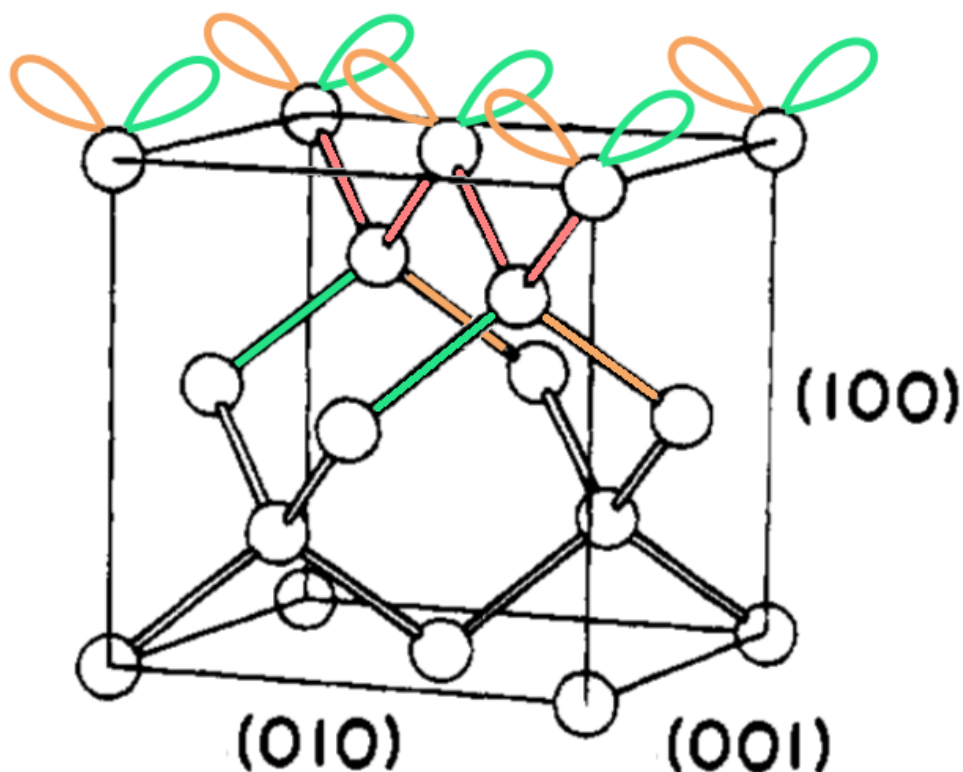
(a) The silicon unit cell. The green and orange lines respresent the bonds broken to form the Si(100) surface, while the green and orange petals indicate the associated dangling bonds. The red lines indicate a single "backbone" linking together a line of surface atoms. Adapted with permission from [3]. Copyright (1995) American Chemical Society.

that the dimer rows should run in the perpendicular direction. This prediction is confirmed by scanneling tunneling microscopy (figure 2.5b), which reveals the dimer row direction rotating 90° at monoatomic (one atom high) step edges. The distribution of step edges is stochastic[4] so that when observed over macroscopic areas the dimers run with equal likelihood in either direction. This gives rise to a *statistical* four-fold rotational symmetry, as evidenced in the pattern produced from low-energy electron diffraction (LEED) from the Si(100) surface (figure 2.6). We exploit this symme-

---

[4] Though for silicon samples intentionally miscut at large ($> 2°$) angles to the (100) direction double-atomic steps prevail, resulting in "single domain" surfaces with all the dimer rows running in the same direction. See [4] for a study the dependence of hydrogen reactivity on the *azimuthal* angle of incidence on Si(100), i.e. whether the molecule impinges traveling parallel or perpendicular to the dimer rows.

try in the analysis of the results (chapter 6) of our scattering experiment. Detailed discussion can be found in 5.1.

As shown in figure 2.5a, the 2x1 reconstruction still leaves each silicon atom with an unpaired electron. It is believed that this remaining instability is alleviated by a further reconstruction whereby the dimers *buckle* in an alternating fashion, resulting in a 4x2 surface periodicity[5]. The buckling is expected to modify the dangling orbitals so that the upwards (downwards) buckling orbital is lowered (raised) in energy, resulting in preferential occupation of the upper orbital over the lower. The chemical rationale is that the buckling distortion brings the upper (lower) dimer atom into a $sp^3(sp^2)$ bonding geometry with its neighboring atoms, so that the dangling orbital in the upper orbital contains more lower-energy s-like character than the lower dangling orbital, which should be bear closer resemblance to a higher-energy p-orbital[6] See figure 2.7 for an illustration.

The buckling distortion does not modify the conclusions drawn regarding the statistical four-fold rotational symmetry (see section 5.1). It should also be noted that, at room temperature, the enlargement of the unit cell periodicity from (2x1) to (4x2) is not expected to give rise to additional diffraction spots in LEED due to the thermally driven flipping of the buckling orientation, which occurs many times over the time scale of a LEED observation. This flipping motion, it should be noted, exhibits long range spatial correlations [7] so that over the course a single molecular scattering event the impinging molecule can expect to encounter an environment closely resembling the ideal (4x2) reconstruction.

2.2.2 Preparation

High temperature annealing of the Si(100) surface has become the established method of obtaining the ideal Si(100) reconstructed surface. In our work we follow the prescriptions laid out in the popular reference by Hata et al. [8] and elaborations described in the dissertation of Guo [9].

---

[5] Experimental evidence for the buckling and the chemical implications are discussed in detail in a review by Yoshinobu [6].

[6] Incidentally, this respective filling/emptying of the upper/lower dangling orbitals suggests a classification of the upper and lower atoms in a dimer as Lewis base and acid, respectively. See Yoshinobu [6] for a thorough development of this interpretation of the Si(100) surface.
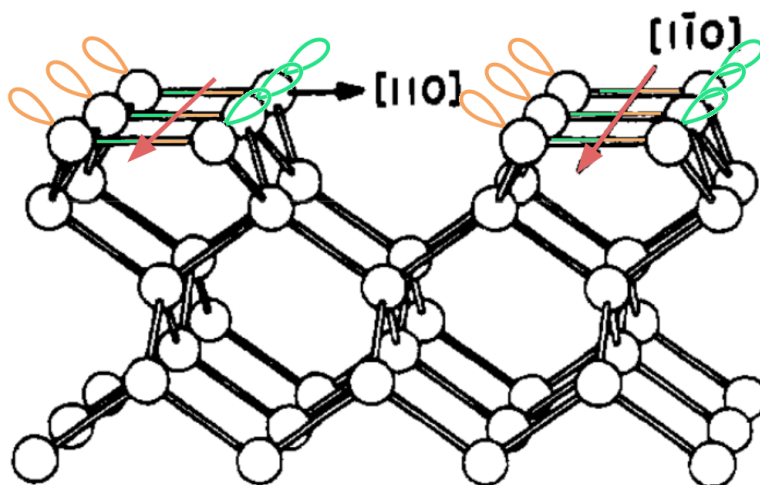
(a) Diagram
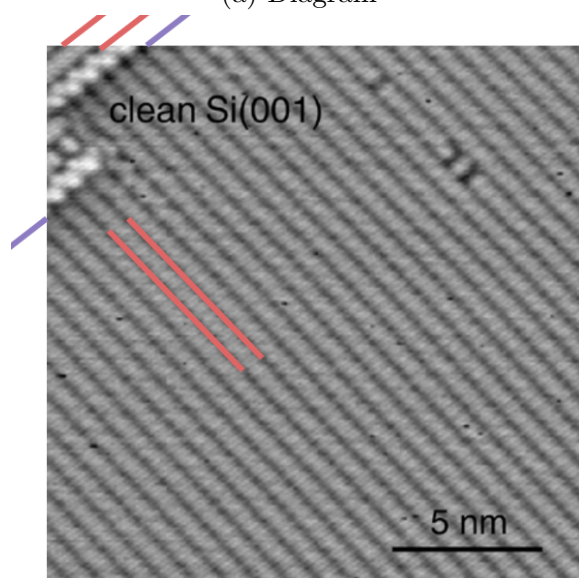
(b) STM image

Figure 2.5: The Si(100)–(2x1) reconstruction. **(a)** shows a version of figure 2.4a modified to reflect the dimer-row reconstruction. The green and orange lines now denote the dimer bonds formed by the overlap two dangling bonds from figure 2.4a, while the petals denote the remaining dangling bond per surface atom. The dimers organize into rows, indicated by the red lines. **(b)** shows a scanning-tunneling microscopy image of the clean Si(100) surface. The dimer row structure is clearly visible, appearing as lines of alternating darkness/brightness (red lines as guide). The purple lines mark a monoatomic step edge, above which the dimer rows now run in a direction perpendicular (lower left → upper right) to those on the lower terrace (upper left → lower right). Figures (a) and (b) are adapted from [3] and [5] with permission from the American Chemical Society and Taylor & Francis, respectively.
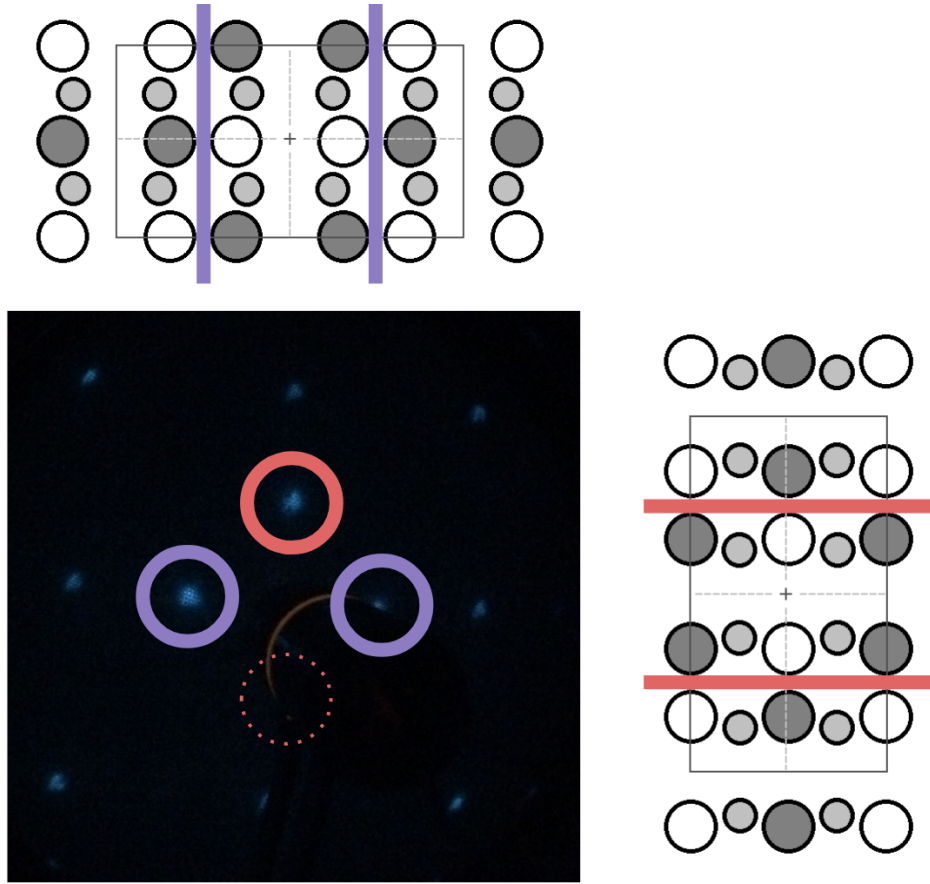
Figure 2.6: Low energy electron diffraction of physical Si(100) surface. The outer diffraction spots indicate 1x1 periodicity while the inner spots indicate 2x1 periodicity arising from the dimer-row reconstruction. The spots circled in red and purple originate from dimer rows running in the horizontal and vertical directions respectively. Note that the rightmost spot is partially obscured by the electron gun, while the lower spot is completely obscured, though by symmetry considerations we expect their brightness to be equal to their mirror image partner. See figure 5.1 for an explanation of the Si(100)–(4x2) unit cell diagram, shown here above and to the right of the diffraction image for the two possible orientations. The rough equality of brightness of 2x1 spots in the vertical and horizontal directions indicates the equal statistical distribution of dimer row orientations along the two directions.
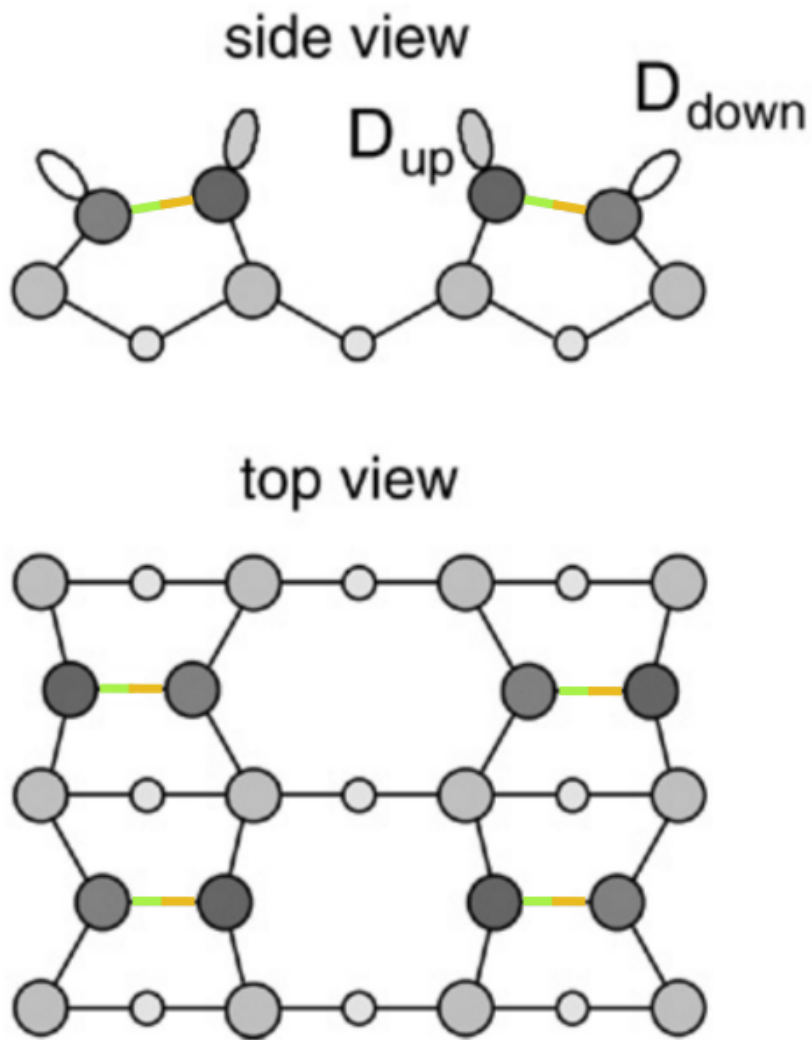
Figure 2.7: The Si(100)–(4x2) buckled dimer reconstruction. Dimer bonds are indicated with green-orange lines as in figure 2.5a. The buckling distortion is suspected to drive partial transfer of charge from the lower buckling dimer atom to the upper. As indicated in the figure, the buckling is suspected to alternate both along and perpendicular to the dimer rows. Adapted from [7] with permission from Elsevier.

The typical contaminants on the Si(100) surface are oxygen and carbon. The oxygen desorbs as SiO around 1100K, though desorption at these temperatures is suspected to leave the surface reconstruction in a disrupted state. The carbon, however, does not appear to desorb any temperatures, and the understanding is that around 1400K is begins to dissolve into the bulk of the silicon crystal. To reverse the deleterious effects of both contaminants it is thus found necessary to raise the surface temperature above 1500K for short periods of time ($\approx$ 30s) before rapidly ($\approx$ 5s) quenching the temperature below 1200K (taking care to remain well below the melting temperature of 1678K). The high temperatures not only provides the silicon atoms with the necessary mobility to anneal out the "pitting" incurred by SiO desorption but also allows the carbon atoms to desolve into the bulk. The quenching step should be rapid so that the carbon can not resegregate to the surface.

The most convenient method of obtaining the elevated surface temperatures is via direct resistive heating. For our sample geometry (25mm x 10mm x .65mm, current running parallel to the long dimension) and resistivity ($\approx$ .015Ωcm) we found it necessary to apply roughly 25A of current to reach the desired annealing temperature ($1500K$ as determined by Land Cyclops L infrared pyrometer, .83 emissivity setting).

To prevent fracture during the heating and cooling cycles we found through experience that only force should be applied to restrain the silicon sample in its holder. We found that a coiled foil "scroll" of .004" thick tungsten suitable for this purpose. See figure 2.8 for a diagram of our scroll-sample assembly holder. The different components are as follows:

- A: Flange mounted to three axis translation stage (not shown)

- B: Stainless steel clamp

- C: Stainless steel slider

- D: Conflat power feedthrough flange

- E: Stainless steel brackets (2x)

- F: Silicon sample

- G: .004" thick tungsten scroll

- H: Silicon buffer slivers (top and bottom). These are included to prevent metallic contamination of the silicon sample by metal. Slivers can be added as necessary to tune the clamping force.

- I: Lower OFHC copper scaffolding.

- J: OFHC copper power feedthroughs (Insulator Seal Incorporated). These are bent and inserted into the copper scaffolding and fastened to scaffolding with a set screw.

- K: Upper OFHC copper scaffolding

- L: Ceramic shoulder washers. These are used to electrically isolate the copper scaffolds from the chamber.

2.2.3 Characterization

To characterize the effectiveness of our cleaning procedure we rely on LEED imaging, mentioned earlier in section 2.2.1 (see, e.g. figure 2.6). We found that Auger electron spectroscopy is a poor measure of surface order in that it can indicate contamination levels below our detection threshold ($< 10^{-2}$) at surface conditions for which LEED indicates poor surface order.

Shown in figure 2.9 are LEED images which we take to indicate a well ordered reconstructed Si(100) surface.

2.3 Stimulated Raman Pumping

2.3.1 Stimulated Raman Pumping

The state preparation stage of our experiment is accomplished using the technique of stimulated Raman pumping (SRP)[10]. Two lasers whose frequency difference is matched to the transition frequency of two energy levels in a molecule can efficiently drive that transition, transferring molecules from the level of higher initial population to the lower. Classically we may think of the molecule as facilitating "mixing" between two laser fields, producing radiation oscillating at the beat frequency. This beating
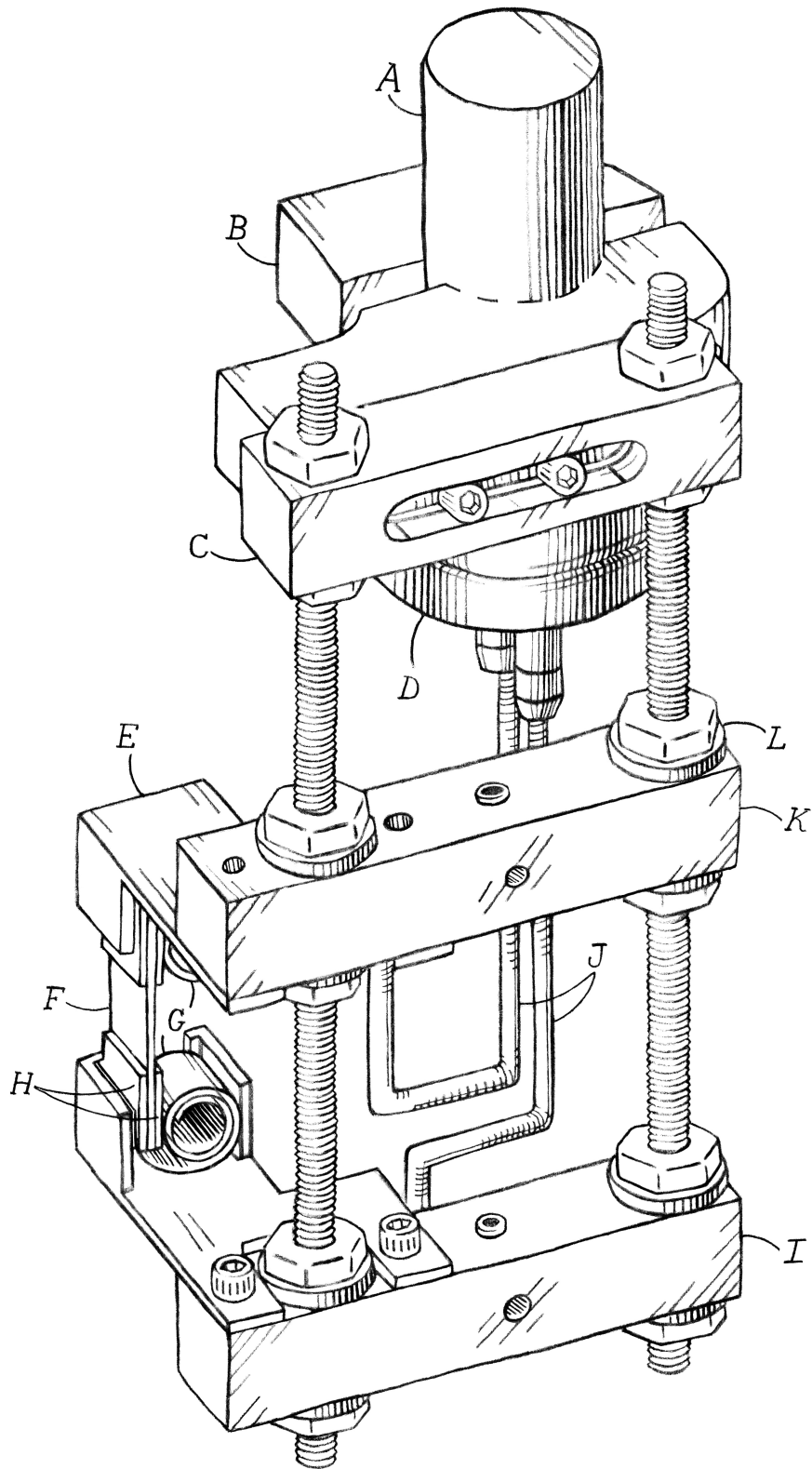
Figure 2.8: The silicon sample holder. See the main text for an explanation of the labels (i.e. $A, B, \ldots, L$). Credit to Andrea Quitugua for the illustration.

(a) dimer parallel   (b) dimer diagonal
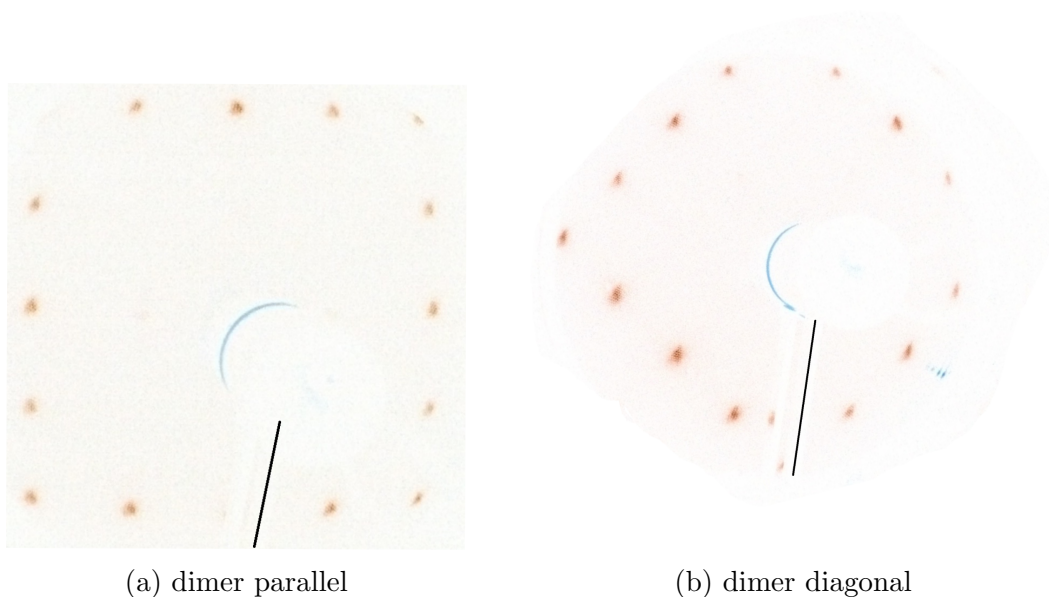
Figure 2.9: LEED images of the well ordered Si(100) surface taken at an incident electron energy of 47eV. The surfaces imaged in figures **(a)** and **(b)** are related to each other by a 45° rotation about the surface normal, i.e. in **(a)** the crystal cleavage direction (i.e. the dimer-row or (011) direction) runs vertically and in **(b)** it runs at 45° to the vertical. As expected, the surface rotation is reflected in the associated LEED image (The arm of the electron gun is indicated by a black line for reference.)

can in turn drive vibrations or rotations in the molecule if the frequency matches a resonance.

2.3.2 Stimulated Raman Emission

SRP can be accomplished by separately generating two lasers pulses with the appropriate frequency difference, and then sychronizing and aligning them so that they illuminate the same focal region at the same time (see, e.g., [11]). In some instances, however, one can use a trick to take a monochromatic laser beam and generate an additional synchronized and copropagating beam detuned by the desired transition frequency using a simple gas cell. A cell used for this purpose is known as a Raman shifter. The trick is based on a general phenomenon known as stimulated Raman emission (SRE), first observed in liquids but detected for the first time in gases by

Minck et al. [12] in 1963[7].

The explanation of the effect is as follows. When an intense monochromatic laser is brought to a focus inside of a gas cell, *spontaneous* Raman scattering is generated over a broad range of solid angles. Some fraction of this scattered light is emitted in the direction of laser propagation, and can then beat together with the unscattered radiation – á la SRP – to resonantly drive further inelastic scattering. Crucially this stimulated process is *coherent* in that the emitted radiation copropagates with the original laser.

As energy builds up in the copropagating mode it can come to dominate over all other scattering processes in winner-take-all fashion [8]. As a result in an SRE spectrum one typically finds all peaks separated by the same frequency shift corresponding to the transition with the largest overall cross section. This is contrasted with the spontaneous case where one usually observes multiple shifts reflecting the variety of resonances possessed by the molecule.

SRE generated by rotational transitions in H_2 were again first observed by Minck [15] in 1966. To beat out competition with the strong vibrational transition it is necessary to circularly polarize the incident laser radiation. At room temperature the population of molecules in the $j = 1$ rotational state exceeds that of any other state by at least a factor three, so that the S1 ($j = 1 \rightarrow 3$) transition dominates[9]. See figure 2.10 for a SRE spectra taken in our laboratory. Note that the first Stokes line at 549nm and the Rayleigh peak at 532nm are of comparable strength, implying signficant conversion of the incident pulse energy. We also observe a smaller longer wavelength peak at 567nm. This peak we attribute to SRE generated by the 550nm radiation, which is itself SRE generated by the 532nm input radiation.

---

[7] See [13] for an entertaining early review of the subject.

[8] The author in [13] likens the situation to the board game Monopoly where the player who can acquire a small amount money early is able to dominate control the flow of money later in the game.

[9] By cooling the gas to liquid nitrogen temperatures (77K) the S0 transition can be selected. Note however that in a typical glass or steel vessel the nuclear spin flip required to convert odd j H_2 (*ortho*hydrogen) to even (*para*hydrogen) occurs with very low frequency so that ortho-para equilibriation may take a full day or even longer. It is found though that by flowing the low temperature gas over a zeolite catalyst the equilibriation time may be reduced to a few minutes or less depending on the state of the catalyst. In our observations of SRE from zeolite processed hydrogen we find many instances of emission of comparable strength on the S0 and S1 Stokes lines (as well as the anti-Stokes lines), though typically after sufficient processing the S0 process will come to dominate.
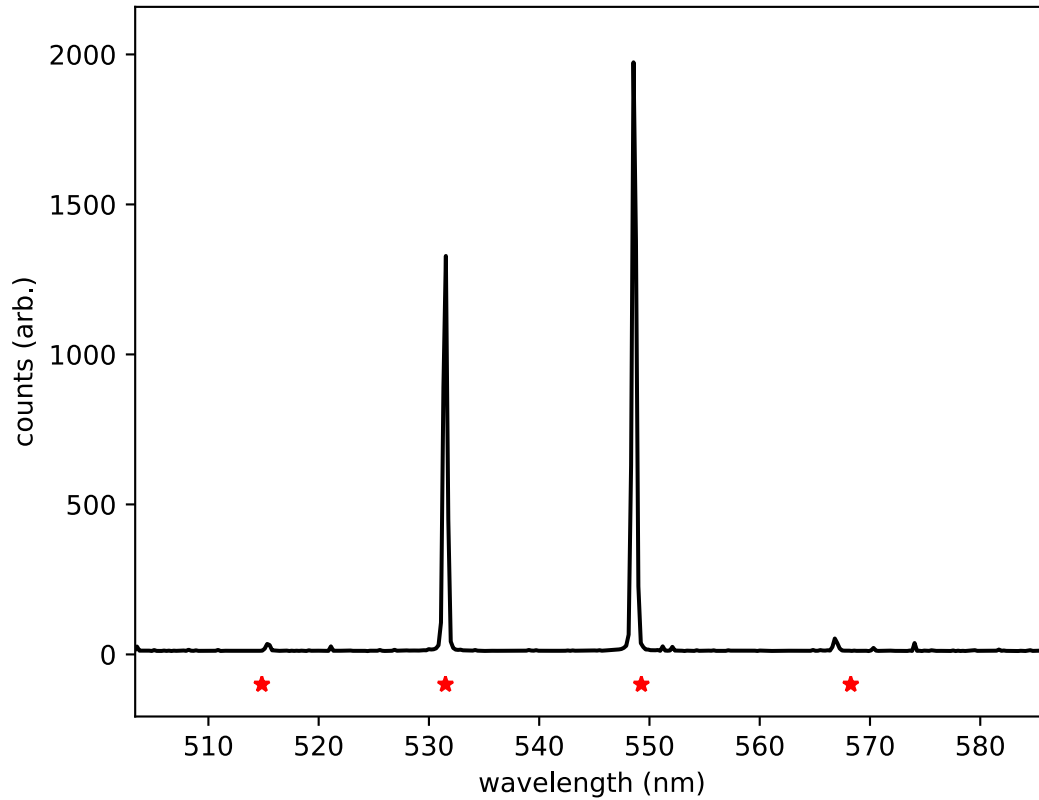
Figure 2.10: SRE spectrum of H_2 at 300K and 1 atm cell pressure. The excitation source was a 50mJ pulse of 532nm laser radiation, approximately 5ns in duration, obtained by frequency doubling the output of a Q-switched Nd:YAG laser. The 532nm pulse was brought from a diameter of ≈ 5mm to a shallow ($f = 1m$) focus in the gas cell. The red stars indicate the location of the Rayleigh peak (532 nm) and the expected location of the first two Stokes and first anti-Stokes lines assuming a $j = 1 \rightarrow 3$ transition frequency of $10B$ where $B = 60.853$cm^{-1} is the ground state rotational constant as tabulated by NIST [14].

2.3.3 Pump Laser System

A diagram of the pump laser system is shown in figure 2.11. See Siegman [16] for a discussion of the pulsed Nd:YAG laser, and Boyd [17] for a discussion of nonlinear frequency doubling in KDP. The polarizer (Thorlabs polarizing beam splitter) is positioned directly behind the last focusing lens to avoid/eliminate any ellipticity incurred as a result of internal reflections from back faces of the many (10) steering prisms used to direct the beam into the main chamber. From the roughly 5mm beam size and 10cm focal length focusing lens, we can antipicate a focused waist of some tens of microns and a Rayleigh length on the order of 1cm. This estimate is consistent with results from both time of flight measurements (section 6.1.1) and vertical scan REMPI measurements of the profile of pumped molecule (section 2.4).

2.4 REMPI Probe

2.4.1 REMPI

In our experiment we measure *ionization yields*. The ionization is generated by focusing a "probe" laser onto a region occupied by scattering molecules. The firing of the probe laser is synchronized with the pump laser (section 2.3) so that the probe illuminates the pumped molecules after they have scattered from the surface (i.e. figure 2.1). Using charged "steering plates", the ionization is directed onto the face of charge multiplier where the current is amplified before being recorded. See figure 2.12 for an illustration of the measurement scheme.

Measuring ionization, as opposed to, say, fluorescence, has the advantage that ions can be collected with near perfect efficiency. We utilize an ionization scheme known as REMPI – **R**esonantly **E**nhanced **M**ulti-**P**hoton **I**onization[10]. See figure 2.13 for a conceptual diagram and the associated caption for an explanation. The technique is *state-specific* in that molecules can in general be ionized out of at most one ground electronic molecular state. With a tunable source of laser radiation it is then possible to measure the ionization yield and thus indirectly the relative population of the different molecular states. In a scientific sense, this feature of the resonant aspect of REMPI is not useful for our experiment, which focuses on a single rovibrational

---

[10] See [18] for a review of the technique
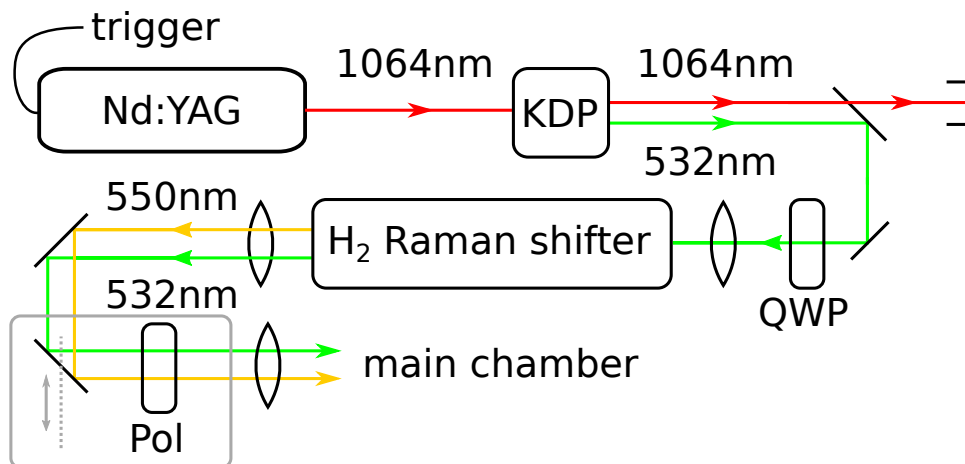
Figure 2.11: Diagram of the SRP laser system. The 5ns long, 532nm pulse driving the Raman shifter is generated by frequency doubling (via a KDP crystal) of 1064nm radiation from a flash-pumped and Q-switched Nd:YAG laser (Continuum Surelite). The firing of the Q-switch is timed relative to the nozzle trigger so that the pump laser intercepts the molecular beam. A quarter wave plate converts the linearly polarized output of the KDP crystal to circular, enhancing the strength of rotational scattering in the Raman shifter. Before focusing into the main chamber, the output of the Raman shifter is linearly polarized to establish a plane of alignment for the pumped molecules. The plane of alignment may be rotated by rotation of the polarizer. The polarizer and final focusing lens are mouted on a translation stage (shown in grey) so that the location of the focus may be adjusted along the direction of molecular beam propagation.

level. As a practical matter, however, the ability to address other rovibrational levels is indispensable for preparations, optimizations, and diagnostics.

As explained in figure 2.13, our particular flavor of REMPI is (2+1), meaning that the ionization process is a sequence of two-photon absorption to an intermediate excited electronic state followed by one-photon ionization from the intermediate state. The ionization cross section is relatively strong, so that, at our laser fluences, any molecule excited to the intermediate state is assumed to ionize[11]. The two-photon

---

[11] Though at low pulse energies it is certainly possible to incompletely ionize molecules in the intermediate state. From a simple calculation we find the fraction f of molecules remaining in intermediate state is given by

$$f = \frac{1 - e^{-\beta}}{\beta}$$
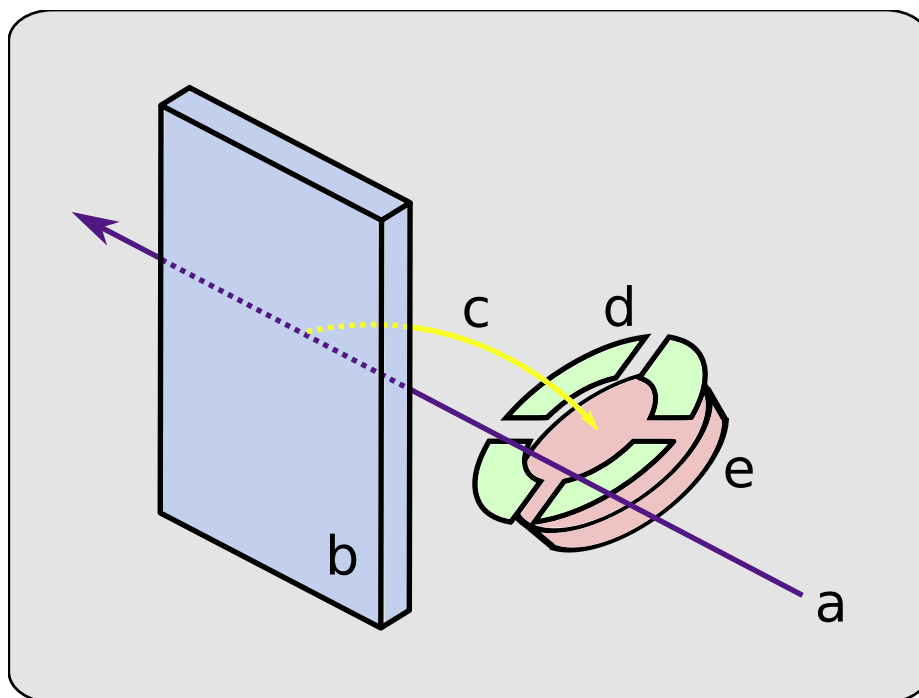
Figure 2.12: Illustration of measurement scheme. The probe laser (**a**/purple) is focused onto the molecules scattering from the surface (**b**/blue), producing photo-electrons and ions. The postively charged ions (**c**/yellow) are attracted to the front face of the negatively charged microchannel plate (MCP) (**e**/red). Four steering electrodes (**d**/green) with independently variable potentials are used to guide the ions onto the MCP. The impact of an ion on the front of the MCP initiates an electron cascade which propagates towards the back face, producing a measurable current pulse exiting the MCP. This current is collected by an anode (not shown), positioned directly behind the MCP and held at a positive (50V) potential with respect to the back face of the MCP. The anode current is further amplified and then integrated to produce a measure of the ionization yield. Where the probe laser and ion trajectories are obscured by the surface we have indicated by dotting the lines.
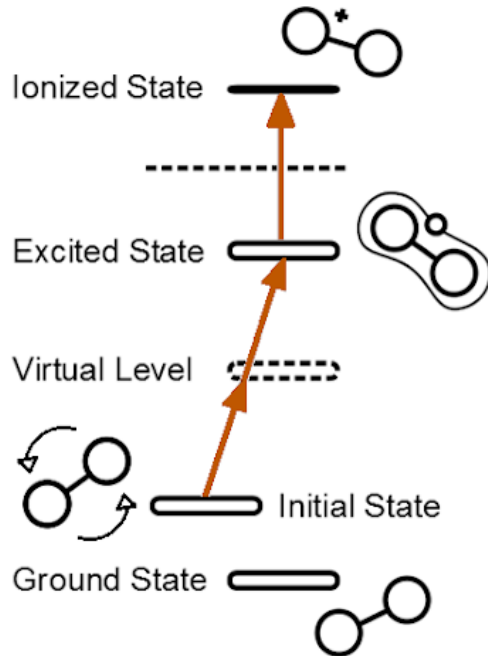
Figure 2.13: (2+1) REMPI ionization scheme. Of all the molecules in the ground electronic state, only one rovibrational level (labeled *Initial State*) is two-photon resonant with some intermediate electronic state (*Excited State*). Molecules occupying other rovibrational states (e.g. *Ground State*) are essentially transparent to the probe laser. Molecules excited to the intermediate state are subsequently ionized by absorption of one additional photon from the same laser pulse.

---

where β characterizes the pulse energy. The population p of molecules remaning in the intermediate state on the other hand has the form

$$p \propto \beta \left(1 - e^{-\beta}\right)$$

so that yield unsurprisingly decreases with decreasing pulse energy.

p can be measured by measuring the ionization produced by a second strong laser pulse timed and positioned to overlap with molecules excited by the REMPI pulse (imagine placing step **e** before **b** in figure 2.1). This second laser pulse should have a wavelength and fluence sufficient to ionize any molecule remaining in the intermediate state. In addition, the time interval between the initial REMPI pulse and the second ionizing pulse should be made shorter than the radiative lifetime of the intermediate state.

f can similarly be measured by comparing the ionization yields from the initial REMPI pulse to the second ionizing laser pulse. For our REMPI system we find by sufficient reduction of the REMPI pulse energy we can obtain for some transitions survival fractions f in excess of 50% at yields p easily detectable by our ion collection electrons.

For the pump-probe scheme employed in our experiment a low pulse energy (i.e. low β) is purely detrimental in that the ioniziation yields are low and the analysis is complicated by incompletness

21

transition is then the rate limiting step, so that the expected ionization yield is governed by the strong two-photon selection rules operative between two discrete rovibrational states. These selection rules predict strong modulation in the ionization yield with laser polarization for molecules with non-trivial *alignment*. This aspect of REMPI spectroscopy is described in detail in section 4.7.

In the following sections we outline the relevant details regarding the structure of the H_2 energy levels (section 2.4.2) and describe our REMPI laser system (section 2.4.3).

2.4.2 The H_2 molecule

The Born-Oppenheimer approximation [19] states that the molecular Hamiltonian H (electrons + nuclei) can be partially diagonalized in a basis of states $|\mathbf{R}\rangle|n;\mathbf{R}\rangle$, where $\mathbf{R}$ is a nuclear configuration and $|n;\mathbf{R}\rangle$ is the nth lowest energy solution[12] to the electronic Hamiltonian with the nuclei fixed at $\mathbf{R}$. In this basis we find that

$$\left(\langle\mathbf{R}'|\langle n';\mathbf{R}'|\right) H \left(|\mathbf{R}\rangle|n;\mathbf{R}\rangle\right) \propto \delta_{n'n}$$

so that a molecule beginning in the nth electronic state remains there as time progresses. In other words the nuclear motion separates into independent motions for each electronic index n, each with its own associated potential $V_n(\mathbf{R})$.

In figure 2.14 the potential energy is plotted for the $X^1\Sigma_g^+$ electronic state[13], the lowest (ground) level ($n = 0$) of diatomic hydrogen[14]. The potential is plotted as a function of the $H-H$ bond length r, the only coordinate on which the potential

---

of the ionization step. The ability to produce a population of electronically excited molecules is however useful in other scenarios.

For instance, it allows for the possibility of studying scattering of electronically excited molecules from surfaces. Preliminary measurements from our group suggest that few if any ($< 0.1\%$) of these "metastable" molecules survive the scattering process.

Secondly, the ease of aligning the pump (section 2.3) and probe beams, a traditionally difficult task, is vastly improved if the SRP pump beam is used to detect "secondary ionization" from the residual molecules left in the intermediate state by the REMPI probe. The secondary ionization is usually detected after only modest alignment effort, after which optimizations are more or less trivial.

[12] Complications arising from degeneracy of the electronic states do not concern us here.

[13] See [20] (Chapter 3) for a discussion of the electronic state symmetry labels for diatomic molecules.

[14] Data for this curve and others shown in the section were taken from [21]. Information about the energy levels is taken from [14].

depends. The potential is highly repulsive at short bond lengths ($r < 0.5$Å) due to Coulomb repulsion of the positively charged nuclei, while at longer bond lengths ($r > 2.0$Å) the potential becomes constant, as expected of two neutral atoms separated by a long distance. In between these limits the molecule oscillates about its stable equilibrium position at $\bar{r}_o \approx 0.74$Å. For displacements close to equilibrium the potential is roughly harmonic with a energy quantum $\hbar\omega_o = 546$meV, so that the vibrational energy of the molecule is limited to discrete values $\varepsilon_\nu = E_o + \hbar\omega_o \left(\nu + \frac{1}{2}\right)$ where $\nu = 0, 1, \ldots$ and E_o is the potential energy at the equilibrium position $\bar{r}_o$. Conventionally E_o is set to $-\frac{1}{2}\hbar\omega_o$ so that the ground electronic state vibrational energy ε_ν is zero when $\nu = 0$.

In addition to vibrational quanta, the molecule can possess rotational quanta. A molecule with j rotational quanta, where $j = 0, 1, \ldots$ has an associated rotational energy $\varepsilon_j = B_o j(j+1)$, where $B_o = 7.54$meV is proportional to the inverse square of the equilibrium bond length. In total, then, the internal energy of a ground electronic state molecule is given by $\varepsilon_{\nu,j} = \varepsilon_\nu + \varepsilon_j$ (see figure 2.15). Note that this expression is only approximate and that in general we must consider, in addition to anharmonicity in vibrational potential, coupling between the vibrational and rotational motion so that $\hbar\omega_o$ and B_o may each exhibit a weak dependence on both ν and j.

The discussion so far has been restricted to the ground electronic state, though it applies just as well to higher electronic states. E,F$^1\Sigma_g^+$ is the lowest energy two-photon accesible state for H$_2$.[15] See figure 2.16 for the potential energy curve of this state. The interesting double well structure, discovered by comparison of calculations with spectroscopic observations [22], is explained as an avoided crossing between a covalent and ionic structure with a short and long equilibrium bond length, respectively, giving rise to a curve with an inner (E) and outer (F) well.

For our purposes it is only important to note a couple things regarding this state. First off, the potential minima (E_E, E_F) of either well is offset by $\sim$ 12eV from the ground state (X$^1\Sigma_g^+$) minimum. A two photon transition thus requires a photon energy of roughly 6eV, with corresponding wavelength (200nm) in the near VUV region of the electromagnetic spectrum.

---

[15] Though there are lower lying states that are accessible by a one or three photon transition. For a one photon transition, however, there are difficulties in generating the required short-wavelength ($\sim$100nm) light, and for the three photon transition there are issues with Stark shifting/broadening at the high intensities. The two photon transition is therefore a good tradeoff.
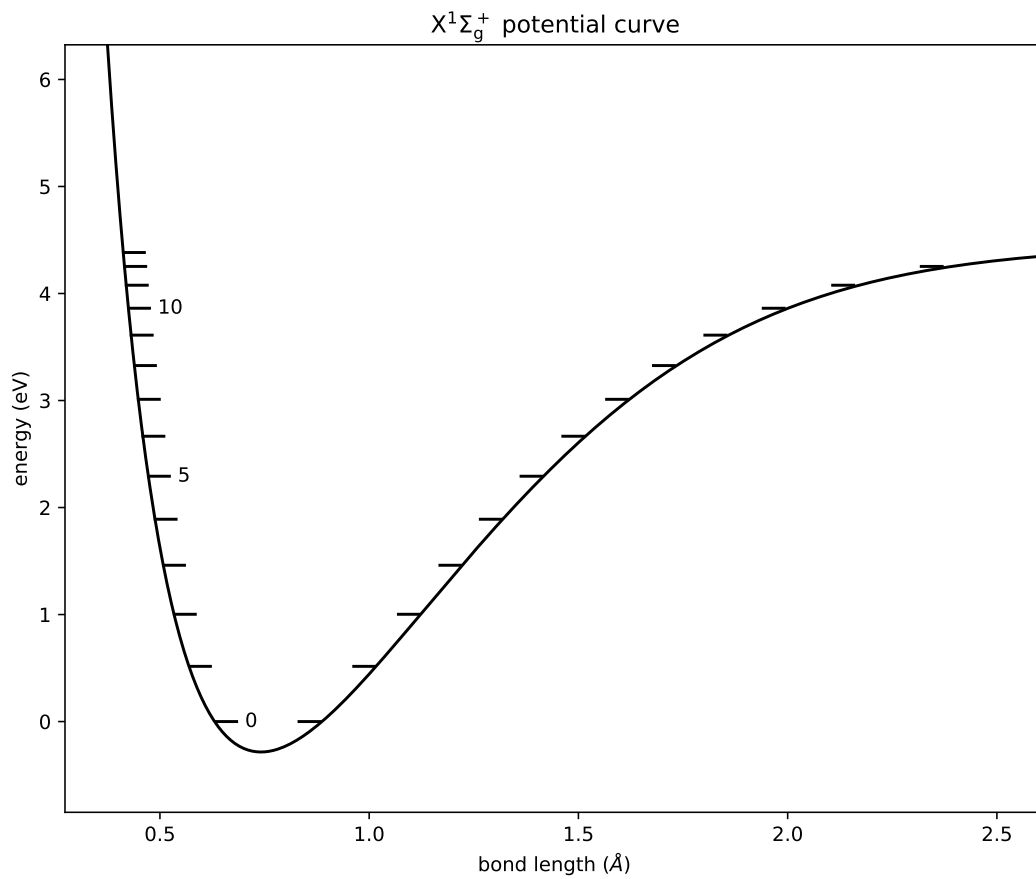
Figure 2.14: Potential energy for the ground state $X^1\Sigma_g^+$ of H_2 as a function of the H$-$H bond length. Indicated by the notches ($-$) are the different vibrational energy levels for the states with $j = 0$.
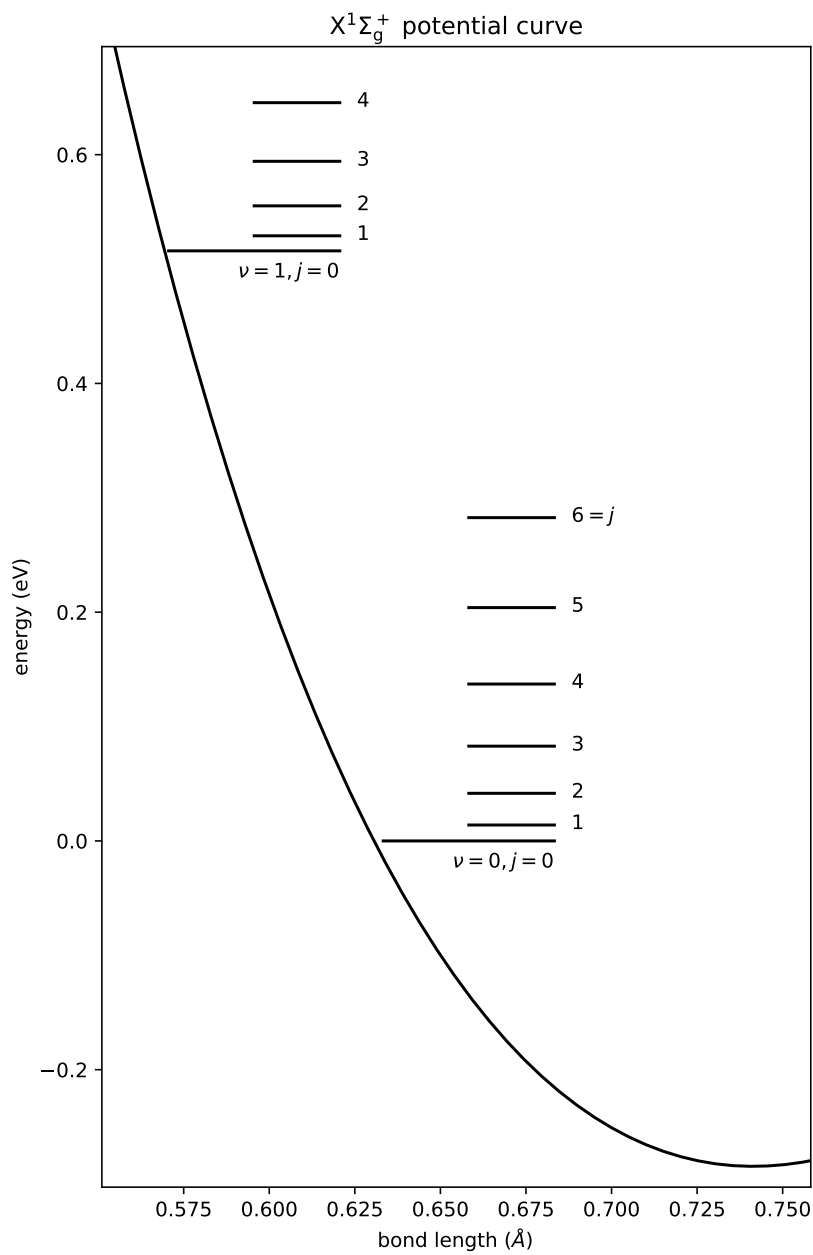
Figure 2.15: Zoomed in version of figure 2.14. On this scale the rotational energy level structure, characterized by quantum number j, can be resolved, in addition to the higher energy scale vibrational structure, characterized by the quantum number ν.
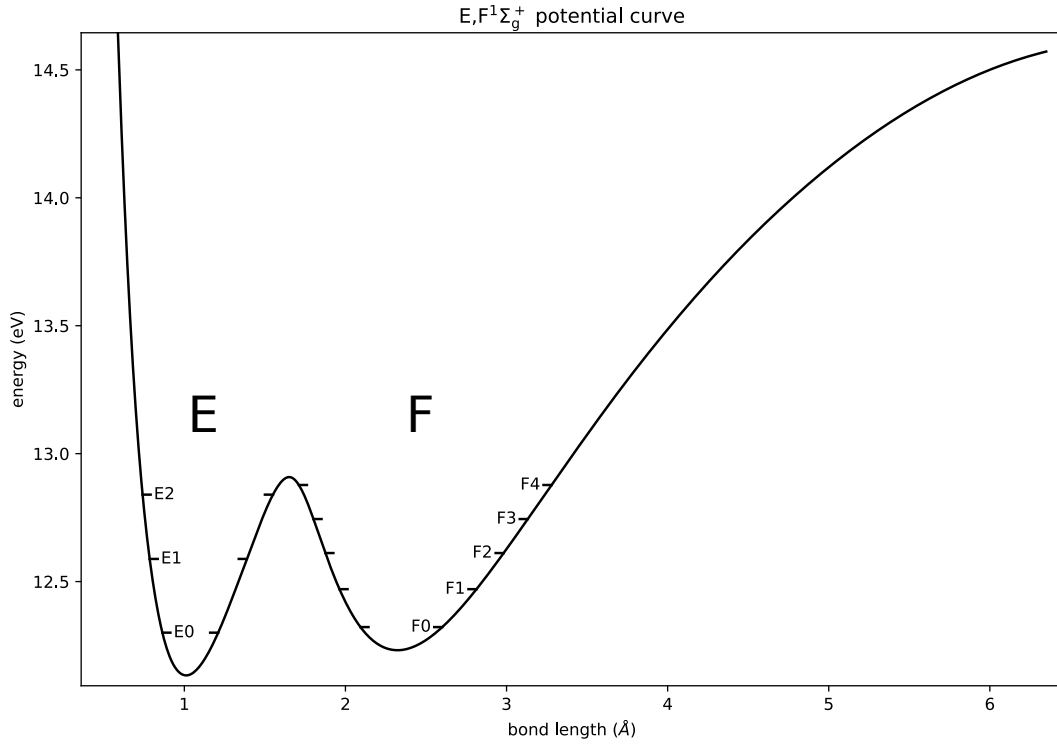
Figure 2.16: The E,F$^1\Sigma_g^+$ electronic state potential curve. The vibrational energy levels are given an E or F designation based on which well the associated wave function primarily lies in. For energy levels higher than those indicated on the figure the distinction becomes increasingly ambiguous.

Next we note that the low energy solutions to the vibrational wave equation are largely confined to one well or the other, and the spacings between energy levels in a given well are roughly evenly spaced, so that we may assign vibrational constants $\hbar\omega_E, \hbar\omega_F$ and rotational constants B_E, B_F for each well. These constants for both wells differ from their ground state counterparts. This is clear from figure 2.17, where we find that the E and F wells not only exhibit less curvature in at their bottoms than the ground state, but also possess longer equilibrium bond lengths. The F state is also seen to overlap poorly with the ground state well, so that transition moments between the two wells should be negligibly small. We expect then no coincidences in the frequencies $f_{\nu,\nu';j,j'}$ of any strong E,F $\leftarrow$ X transitions, since

$$h f_{\nu,\nu';j,j'} = \Delta E + \hbar\omega_E\nu' - \hbar\omega_o\nu + B_e\left(j'\left(j'+1\right)\right) - B_o\left(j\left(j+1\right)\right)$$

26

(where $\Delta E \equiv E_E - E_o + \frac{1}{2}\hbar\omega_E - \frac{1}{2}\hbar\omega_o$) will in general be unique, i.e.[16]

$$(\nu_1, \nu_1', j_1, j_1') \neq (\nu_2, \nu_2', j_2, j_2') \implies f_{\nu_1,\nu_1';j_1,j_1'} \neq f_{\nu_2,\nu_2';j_2,j_2'}$$

Therefore, the ionization yield for any particular resonance can be attributed to molecules from a single ground state rovibrational level.

2.4.3 REMPI laser system

See figure 2.18 for a diagram of our REMPI laser system. The dye laser [23] is used for its wide ($\Delta\lambda \sim 20$nm) tunability, a necessity if multiple vibrational levels are to be addressed with the same laser system ($\frac{\hbar\omega_E - \hbar\omega_o}{\Delta E} \sim 2\% \sim \frac{10\text{nm}}{600\text{nm}}$)[17]. The stressed UV fused silica (UVFS) plate exploits a near perfect coincidence of full- and half-wave retardation at 600 and 300 nm, respectively, at a particular pressure thickness product (see figure 2.19), where the slow axis is parallel to the direction of applied pressure. This produces optimal phase matching conditions for subsequent BBO sum frequency stage.

We close this section with a word of warning. At 600nm, UVFS must be placed under considerable stress in order to exhibit significant birefrigence. This is evidenced in figure 2.19, where the first full wave retardation occurs only after light propagates through a centimeter of UVFS under 200 bar of applied pressure. At 200nm, however, significant retardation occurs under only mild stress. In our observations we found that minor ($< 10°$) rotations of a nylon tipped set screw securing a UVFS steering prism to a mount were enough to produce large ($> 30\%$) changes in the transmission of the prism's output through our homemade UV polarizer (figure 2.20). This is attributed to both the shorter wavelength and the close proximity of 200nm to the absorption edge of UVFS. We experienced a great deal of difficulty eliminating anomalous polarization signals, and only succeeded after eliminating all clamping forces on any optics transmitting 200nm. To secure optics to mounts we opted instead for beeswax as a glue.

---

[16] More precisely the diatomic constants differ enough that any two transitions differ by a margin larger than the 22GHz (.09meV) noise-broadened bandwidth of the REMPI laser.

[17] The seasoned experimenter can tell whether or not their labmate is probing ground or vibrationally excited hydrogen molecules by the hue of the dye laser output.
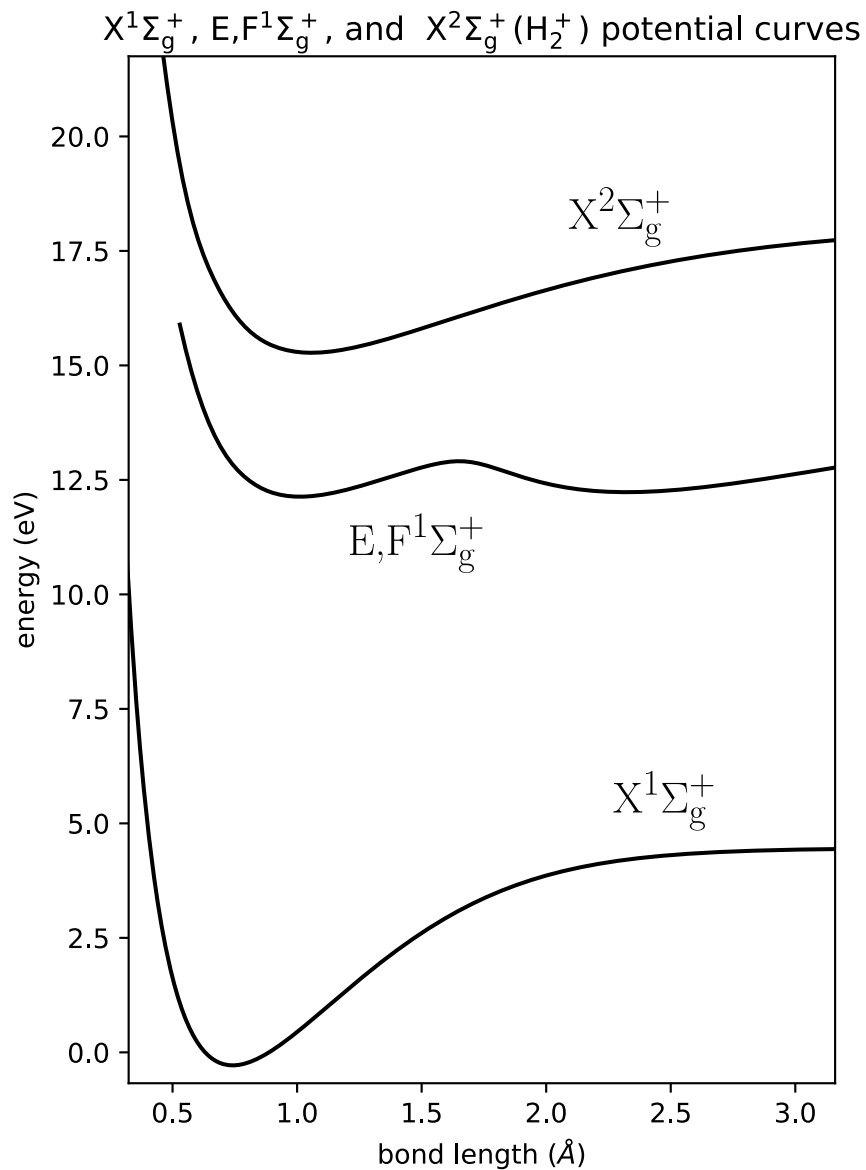
Figure 2.17: The three electronic states participating in our (2+1) REMPI scheme. A molecule from the ground $X^1\Sigma_g^+$ state is excited into the ground or first vibrational state of the E well of the $E,F^1\Sigma_g^+$ state, where an additional photon then ionizes the molecule, leaving it in the $X^2\Sigma_g^+$ state.
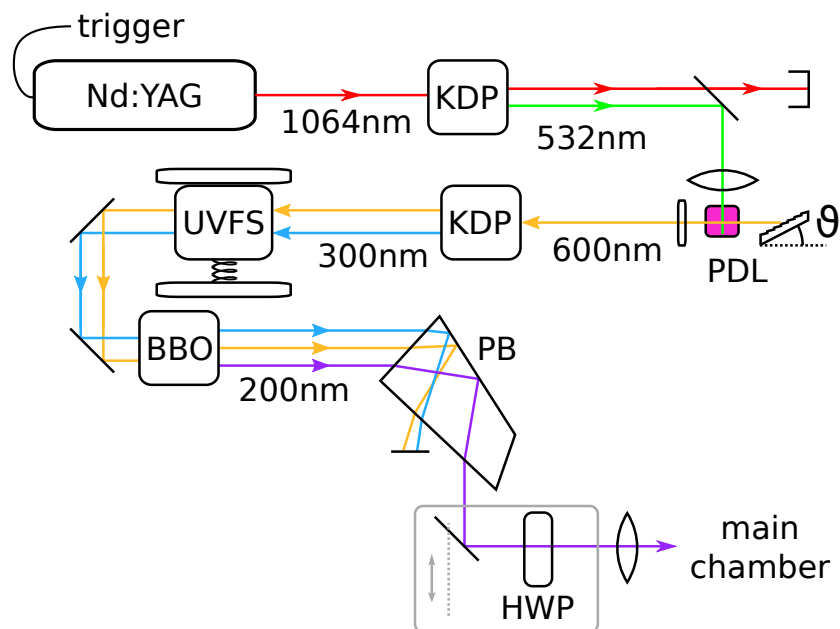
Figure 2.18: Diagram of our REMPI laser system. The 300mJ/5ns frequency doubled output of a pulsed Nd:YAG laser (Quanta Ray GCR4) pumps a dye laser (Quanta Ray PDL3) with grating tunable output wavelength, nominally 600nm. The dye laser operates with Rhodamine 640 (Exciton) dye in methanol solution. The 50mJ/5ns output of the dye laser is frequency doubled in a KDP crystal (Newlight Photonics), generating 1.5mJ of 300nm second harmonic. The fundamental and second harmonic are sent through a plate of stressed UV fused silica which acts as a half (full) wave plate at 300nm (600nm) before mixing in a BBO crystal (Newlight Photonics) to form $400\mu J$ of 200nm light via sum frequency generation. The third harmonic is separated out using a UVFS Pellin-Broca dispersing prism (Thorlabs) before being sent through a MgF_2 half wave plate (Karl Lambrecht) before being focused and sent into the main chamber. The half wave plate and focusing lens are attached to a three axis translation stage (indicated by the gray lines).
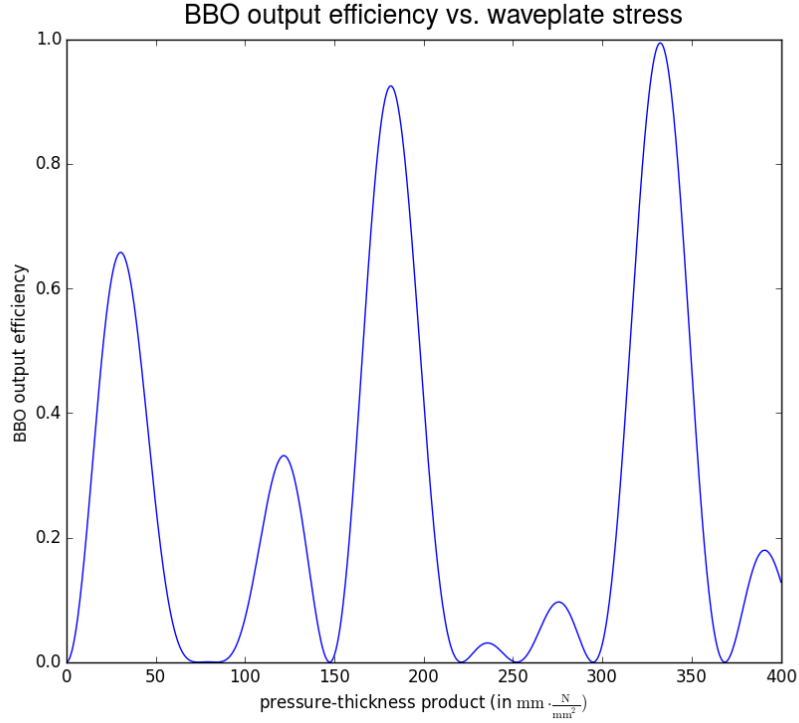
Figure 2.19: Waveplate action of stressed UVFS. The 600nm fundamental and 300nm second harmonic (see figure 2.18) exit the KDP crystal with vertical and horizontal polarizations, respectively. The output of the BBO sum frequency stage is proportional to the product of the projections of the two polarizations on the vertical axis, which we define as the "output efficiency". At a pressure-thickness product of $\approx 340\text{mm} \cdot \frac{\text{N}}{\text{mm}}$, both harmonics exit the stressed waveplate at nearly vertical polarization, as indicated by the $\approx 100\%$ output efficiency. In our own observations we found BBO output energy to follow roughly the same profile shown in this figure as the stress was gradually increased. Curve produced using stress-induced birefrigence coefficients measured by Sinha in [24].
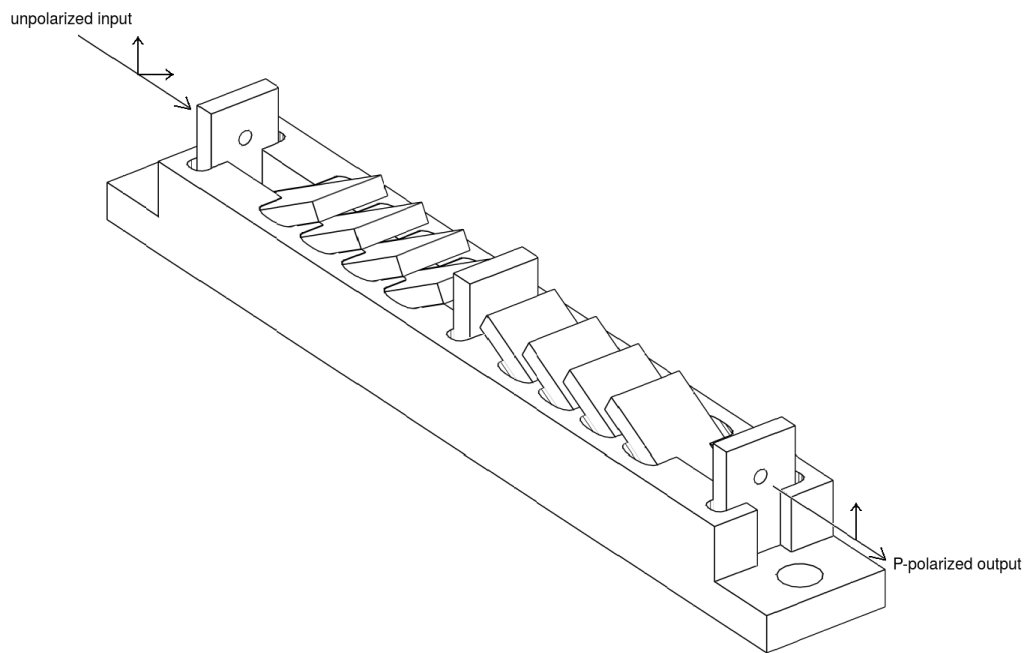
Figure 2.20: Homemade stacked plate polarizer. Light is polarized by preferential reflection of S-polarized light of the front and back faces of the eight UVFS slabs oriented at Brewster's angle. The slabs are restrained in their carriage slots by silicon rubber tabs. The vertical plates are aluminum apertures which transmit the primary beam while blocking secondary reflections. Tests confirm the expected 20:1 extinction ratio, though losses were found to be non-negligible ($\approx 40\%$).

Chapter Three: Background

Our work falls under the category of gas-surface dynamics, which in turn is contained under the larger category of reaction dynamics. The subject of reaction dynamics is best understood by its relation to two other large branches in the field of chemistry: energetics and kinetics.

Energetics is concerned with the thermodynamic *stability* of different chemical species, i.e. for a given set of circumstances (temperature, pressure, etc.) how will matter distribute itself if left on its own (i.e. in equilibrium)? Microscopically we may think of equilibrium as the condition where in-fluxes are matching out-fluxes. If we consider for instance a system containing atoms of type A and B that combine to form molecules A_2, B_2, and AB then the we say the system is in equilbrium when the reaction $B_2 + A_2 \rightleftharpoons 2\,A\,B$ becomes balanced. Should the formation of two molecules of AB require significant additional energy beyond what is already possessed by the molecules A_2 and B_2, we find then by energy conservation that at low temperatures the probability of its formation will be rare since it is unlikely that any single collision between A_2 and B_2 will possess the requisite kinetic energy. This constraint does not exist for the reverse reaction, i.e. $2\,AB \longrightarrow A_2 + B_2$, so that, taking into account only the product and reactant energies, we allow that any two colliding AB molecules may react. We find then that in order to balance the rates of AB formation and decomposition we must then have many more $A_2 + B_2$ collisions than $AB + AB$, or in other words we require a much higher *concentration* of the former versus the latter.

Nonetheless it is found for some systems that at low temperatures a thermodynamically unstable species can resist decomposition into its more stable configuration. A famous example is the formation of ammonia (NH_3) from nitrogen (N_2) and hydrogen (H_2), i.e. $N_2 + 3\,H_2 \longrightarrow 2\,NH_3$. Beginning with volume of gas in a standard glass vessel composed of 1 part N_2 and 3 parts H_2 held fixed at standard temperature (25°C) and pressure (1 atm), thermodynamics predicts a near complete (94%)[25] conversion to NH_3 at equilibrium. In practice however no reaction is observed to occur. To explain this apparent conflict with the laws of thermodynamics it is necessary to expand our attention from solely products and reactants to intermediate configurations along the path to reaction. In particular we note that in order to form

NH$_3$ it is first necessary break the existing bonds holding the H$_2$ and N$_2$ molecules together. These bond energies exceed by many times (400x for the case of nitrogen!) the typical excess energy kT possessed by a molecule at room temperatue. The vast majority of intermolecular collisions are therefore unable to dissociate the molecules. We say in these cases that there exists an energetic barrier to reaction. The study of these barriers, their microscopic origin, and their influence on reaction rates falls under the topic of chemical kinetics.

Demonstrating the existence of barriers, however, tells us little about how these barriers might be overcome. The total energy possessed by a set of reactants can be partitioned among their various degrees of freedom in an enormous number of ways, and only a small subset of these partitionings may be effective in promoting the reaction in question. To tackle this issue then we further expand our consideration to the full microscopic trajectory from reactants to products. Which degrees of freedom should be excited to most effectively promote reaction? Does motion excited in one degree of freedom couple strongly into the others as the system progresses along the path to reaction? These study of these and similar questions comprise the field of reaction dynamics.

In the following chapter we look at some existing studies in reaction dynamics, focusing primarily on gas-surface studies. Shared in common between all the experiments presented is use of state preparation or state detection to gain information regarding some particular degree of freedom. In section 3.1 we briefly introduce the potential energy surface (PES), the central theoretical tool for the interpretation of experimental results. Following this a pair of experiments are discussed which utilize state preparation to illuminate the role of molecular vibration in the dissociation of methane CH$_4$ at a metal surface (section 3.2.2). From there we move on to section 3.3 where we begin by discussing hypotheses concerning the influence of rotational energy on the adsorption process. A number of experimental studies are then presented which aim to test these hypotheses. Finally in section 3.4 we complete our survey of gas-surface dynamics with the description of experiments which, like our experiment, probe the effect of rotational *alignment* on molecule-surface interaction.

3.1 The Potential Energy Surface / Polanyi Rules

Since reaction dynamics aims to study the various paths taken en route to reaction, i.e. the time evolution of the system degrees of freedom, the starting point for theoretical understanding is unsurpsingly the equations of motion. In the temperature ranges of interest the motion is presumed to be non relativistic so these equations are Newton's equations in a classical framework and the Schrödinger equation in a quantum framework. H_2 is the lightest of all molecules and so is the most "quantum", i.e. at a given energy it possesses the longest de Broglie wavelength $\lambda = \frac{h}{\sqrt{2mE}}$. At room temperature this wavelength is approximately 1Å, which is the same length scale as the spacing between atoms on a surface. The interaction between hydrogen molecules and a surface would then be expected to exhibit distinctly quantum effects, and indeed in 1930 Estermann working with Otto Stern succeeded in observing diffraction of H_2 from a freshly cleaved NaCl surface[27]. Despite the undeniably quantum mechanical nature of the H_2-surface interaction, many theoretical treatments avoid quantum methods in favor of a classical approach [28]. The debate over the superiority of the two frameworks as applied to H_2-surface dynamics, safe to say, is far from settled.

No matter whether a classical or quantum framework is adopted, a potential energy must be specified before any dynamics can be solved. The full dynamical information of the system is encoded in the potential energy, though of course the relation between the potential and the trajectories/wave functions the potential gives rise to is nontrivial. Interpreting this function geometrically as specifying for each possible set of coordinates a height above a point on high-dimensional hyperplane corresponding to those coordinates, we obtain what is known as a potential energy surface (PES). For a potential taking for instance only two-coordinates as input, we can imagine point particles rolling or sliding around on the resulting PES, i.e. we can use our physical intuition to simulate the dynamics.

The potential energy function receives as input a set coordinates describing the geometric configuration of the particles constituting the system. In general it is necessary to include the coordinates of not only the nuclei but the electrons as well. Inclusion of the electronic motion results in a large increase in the analytic, numerical, and intuitive complexity of the dynamics problem. This increase renders quantum calculations intractable and – considering there is no acceptable classical

theory of atomic let alone molecular electronic structure – makes classical calcuations meaningless. Fortunately, owing to the large mass mismatch between electrons and nuclei, the electronic motion can be "integrated out", so that their effect is reduced to an effective potential on the nuclei coordinates[1,2]. Chemical bonding is in essence the competition between this effective potential and repulsive Coulomb interaction between the nuclei.

For molecule-surface interactions the situation still however appears rather dire, since we still have to handle the degrees of freedom associated with the near-infinite numbers of surface atoms, as well as the subsurface atoms to which they are bonded, and so on and so forth. For lighter incident molecules like H_2 there is reason to claim that the motion of the heavier surface atoms can be neglected and assumed frozen in place. The reasoning is that the light molecules will in general have difficulty transferring energy to the heavy surface atoms, at least in direct (i.e. single bounce) collisions, in the same way a golf ball's energy is largely conserved after ricocheting off a paved cart path. Theoretical treatments neglecting electronic and surface atom motion are said to be employing BOSS, the **B**orn-**O**ppenheimer **s**tatic **s**urface approximation[28]. [3]

For a diatomic molecule, the remaining degrees of freedom are the three center of mass coordinates (x, y, z), the vibrational coordinate (r), and the two rotational coordinates (θ, ϕ). Adsorption and dissociation at a surface are essentially statements about the molecular-surface distance (z) and bond length (r), respectively, and so unsurprisingly these degrees of freedom have historically received preferential attention. Taking slices of the PES through the $r - z$ plane in the vicinity of the surface we obtain what are known suggestively as elbow plots. For the purposes of illustration I've constructed a set of three such plots, shown in figure 3.1. For all three we find a trend of increasing equilbrium bond length with decreasing surface-molecule distance, indicating the gradual weakening of the molecular bond and establishing of atom-surface bonds.

From the elbow plots we can draw a number of conclusions. For the unactivated (no barrier) process 3.1a we would expect dissociative adsorption with high probabil-

---

[1] This technique is known as the Born-Oppenheimer approximation[19].

[2] Though a rapidly growing focus in gas-surface dynamics is on "non-adiabatic" effects, i.e. those which can not be explained within the Born-Oppenheimer approximation. See [29].

[3] In section 5.5 we use BOSS to compute the evolution of the rotational alignment of H_2 molecules scattering from Si(100).

ity over a wide range incident translational and vibrational energies since we find no repulsive region along the reaction path. For the activated processes 3.1b and 3.1c we are led to consider the location of the barrier. In figure 3.1b, the barrier occurs *early* along the reaction path. In this region of the PES the translational and vibrational motions are still largely decoupled, i.e. they evolve independent of one another. Vibrational energy in this case is expected to accomplish very little, as illustrated by the red trajectory that scatters off the barrier and back into the gas phase. Translational energy on the other hand gives the molecule momentum in the direction parallel to the reaction path, resulting in efficient surmounting of the barrier, as shown with the blue trajectory.

The barrier in 3.1c, on the other hand, occurs *late* along the reaction path. This region of the PES differs from the earlier region in two main aspects. Firstly, the reaction path now runs primarily along the bond length coordinate r. Now it is vibrational energy which is expected to promote adsorption, as illustrated by the red trajectory. Secondly, the reaction path exhibits *curvature*, so that the two degrees of freedom no long evolve independently. As a result, energy can now be coupled between the two coordinates, as illustrated by the blue trajectory that accumulates vibrational energy upon scattering from barrier with curved potential contours.

These predicted correlations between translational (vibrational) efficacy and early (late) barriers are dubbed the "Polanyi" rules after chemist John Polanyi who encunciated them first in [30]. The other effect mentioned, i.e. the transfer of energy between the translational and vibrational coordinates induced by PES curvature, is known simply as VT coupling. For polyatomic molecules we may also similarly consider internal vibrational redistribution (IVR), i.e. a surface-mediation interact exchange of energy between the different modes of molecular vibration[4]. In the following section we look at a couple of experiments that probe these theoretical concepts using state prepared molecules.

3.2   Vibrational Efficacy / Bond Selectivity

As mentioned in the prevous section, of the numerous molecular degrees of freedom, the coordinate normal to the surface z and the bond length coordinate r are intuitively

---

[4] Coupling between translation and rotation (R–T transfer) is discussed in section 3.3.
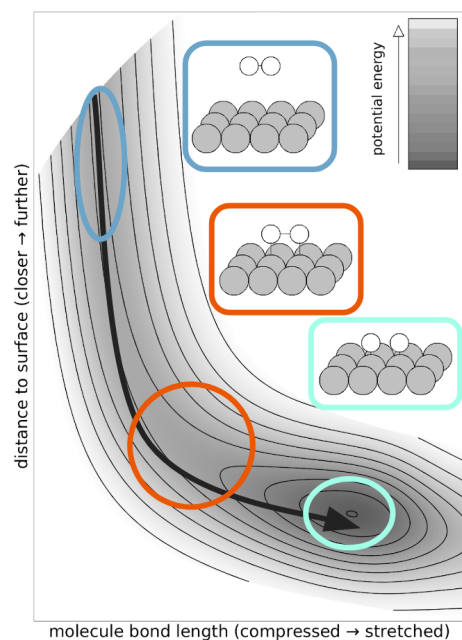
(a) No barrier
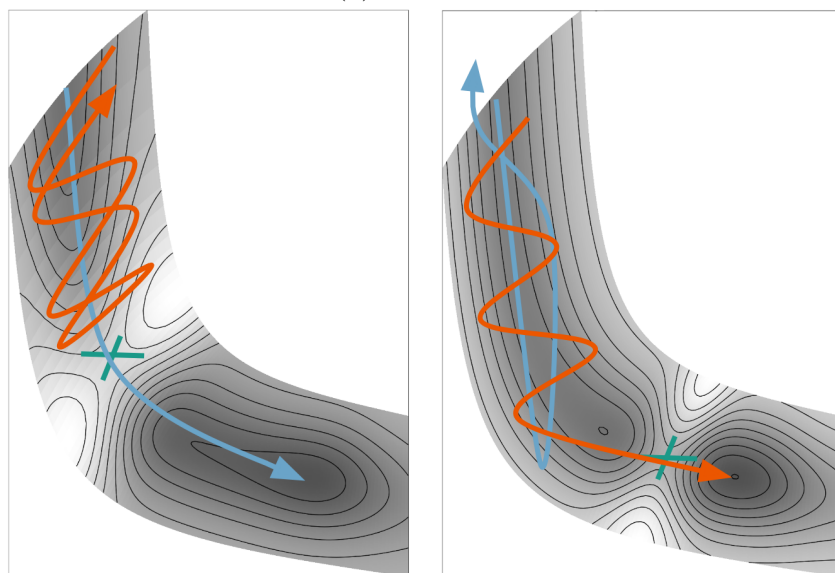
(b) Early barrier

(c) Late barrier

Figure 3.1: Elbow plots for three different barrier configurations. The vertical and horizontal axes correponds to the z and r coordinates respectively. Constant potential contours are drawn in thin black lines, and the value of the potential is indicated in grayscale shading. **(a)** No barrier. The blue and light green ovals denote gas-phase and adsorbed configurations respectively, while the red circle denotes the intermediate region. The black arrow represents a typical trajectory. Early **(b)** and late **(c)** barrier. The green "X" denotes the barrier, while the blue and red trajectories possess high incident translational and vibrational energy respectively.

37

expected to play the largest role in surface reactions. The experiments discussed in this section use laser to prepare beams of vibrationally excited methane isotopologues to explore the interplay between these two degrees of freedom.

3.2.1 CH_4 on Ni(111)

Using optical excitation Smith et al. [31] convert a significant fraction (10-20%) of an incident molecular beam of CH_4 into the first excited state $\nu_3 = 1$ of the antisymmetric stretching mode. By exposing a Ni(111) surface to the molecular beam and later measuring the carbon coverage with Auger spectroscopy[32], the sticking probabilities of the ground $\nu_3 = 0$ and excited $\nu_3 = 1$ states are determined for a wide range of incident translational energies (see figure 3.2). The authors find that the increase in translational energy of vibrationally unexcited molecules necessary to obtain sticking comparable to $\nu_3 = 1$ is 25% in excess of the ν_3 vibrational quantum. In other words, the vibrational efficacy of the ν_3 mode is 125%. From this observation the authors conclude that the vibrational energy permits molecules to access regions of the PES with lower reaction barriers than ground vibrational state molecules.

3.2.2 CHD_3 on Ni(111)

In a similar study from the same group, Killelea et al. [33] direct a beam of triply deuterated methane (CD_3H) at a Ni(111) surface. CHD_3 reacts on Ni(111) by the breaking of a C-H (or C-D) bond to form a chemisorbed CD_3 (or CD_2H) group as well as a chemisorbed H (or D) atom. The ratio of C-H to C-D cleavages is then determined via the ratio of the CD_3H (mass 20) to CD_4 (mass 19) desorption flux as measured on a quadrupole mass spectrometer as the surface temperature is raised above the threshold for associative desorption[34]. The result is shown in 3.3 **a**.

The authors then optically excite the C-H stretch vibrations of the incident molecules and repeat the measurement. Subtracting out the background from the unpumped molecules the authors arrive at 3.3 **b**. Within their detection limit they observe 100% C-H:C-D bond cleave ratio for the pumped molecules. Evidentally there is very little surface-mediated coupling between the different vibratonal modes in CD_3H at Ni(111). Any theory hoping to treat the vibrational energy during a re-
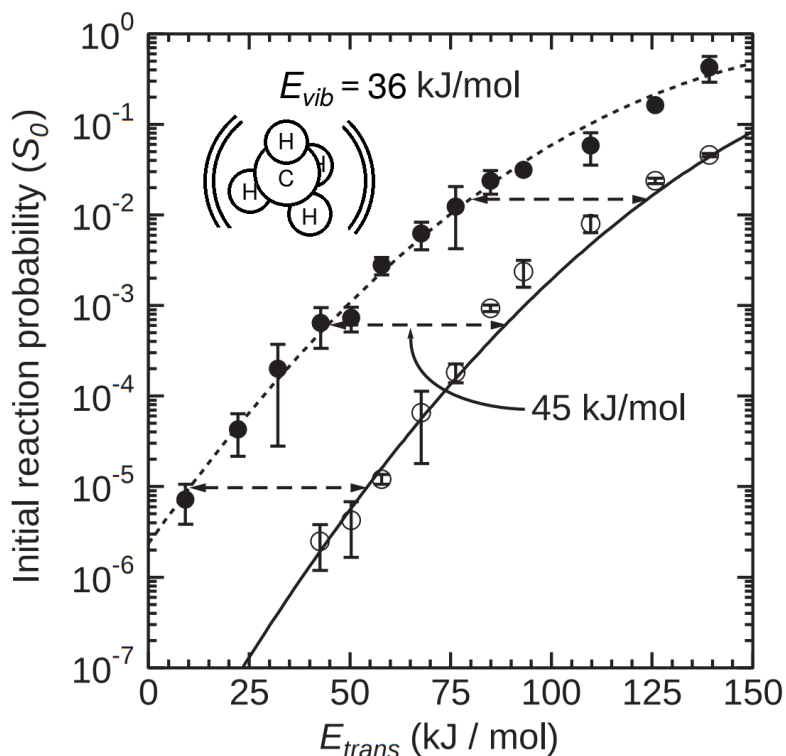
Figure 3.2: Sticking (S_0) of ground-state and vibrationalbly excited CH_4 on Ni(111) vs. incident energy E_{trans}. The solid and open circles denote the $\nu_3 = 1$ and ground state sticking probabilities. The dashed and solid curves are smooth fits to the observations, and the horizontal distance between curves (45 kJ/mol) is to be compared to the ν_3 transition frequency (36 kJ/mol). From [31]. Reprinted with permission from AAAS.

action as equilibriated at all instants among the different modes [35] could not hope to be applicable to systems like the one studied here where IVR is so weak.

3.3   Dynamical Steering / Rotation-Translation Transfer

Compared to the translational and vibrational molecular degrees of the freedom, the role of a molecule's angular momentum in the course of a chemical reaction is less clear. Indeed, rotational motion is by its nature periodic (every 360° you end up where you started!) and so its influence on the progression of a reaction is necessarily
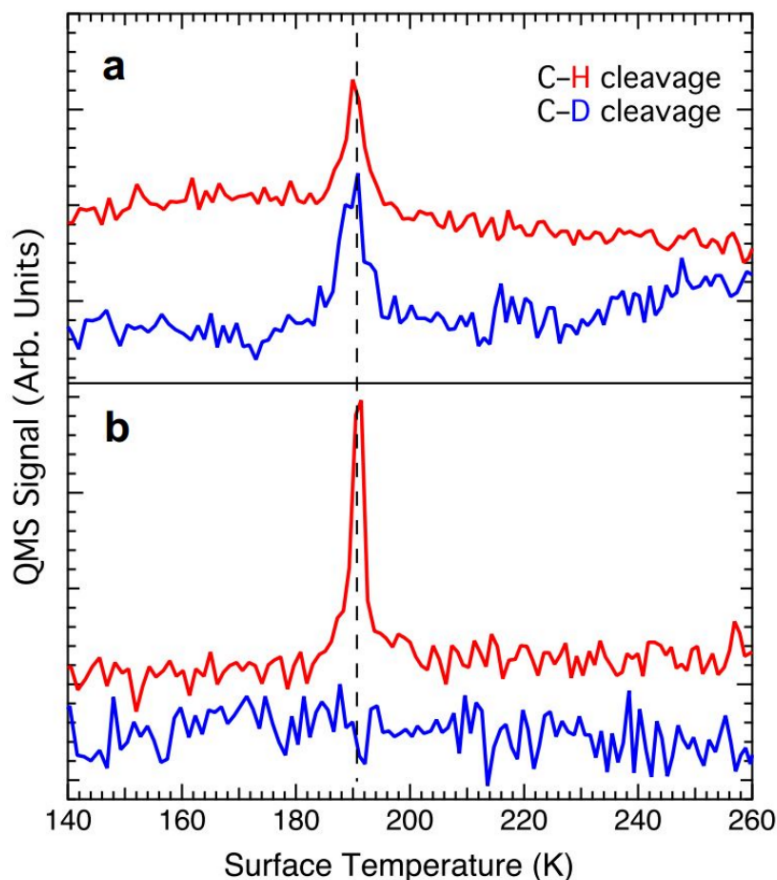
Figure 3.3: Measurement of bond cleavage ratios for **a** unpumped molecules and **b** molecules laser pumped to $\nu = 1$ C-H stretch level. Red (blue) trace monitors desorption of CD_3H (CD_4), indicating C-H (C-D) bond cleavage, as the surface is brought above the temperature threshold for associate desorption. Reprinted from [33] with permission from AAAS.

indirect. All the same, rotational angular momentum has been shown influence a molecule's reactivity at surfaces. The manner in which this occurs falls into two broad categories:

- rotation-translation (R–T) energy transfer, which acts to increase reactivity at *higher* angular momenta, and

- dynamical steering, which acts to reactivity at *lower* angular momenta.

In sections 3.3.1 and 3.3.2 these two effects are explained, and in section 3.3.3 they are explored through a survey of experimental results.

40

3.3.1 R–T Transfer

R–T transfer is the conversion of angular momentum to (linear) momentum along the reaction path. Qualitatively we might then expect this effect to exert a greater influence at higher angular momenta where this is more energy to contribute to surmounting the barrier.

How R–T transfer might come about is best explained using a simple example. Suppose we have a classical molecule impinging on a flat surface and rotating in the pure helicopter orientation, i.e. $\vec{J} \propto \vec{n}$, the surface normal. The molecule's angular momentum (all three components)[5] is thus conserved, and influences the dynamics of the molecule via an effective force

$$\vec{F}_c(r; j) = \frac{j^2}{\mu r^3} \hat{r}$$

where

- j^2 is the squared angular momentum,

- r is the bond length,

- μ is the reduced mass.

The "centrifugal" force F_c is always positive and acts to *stretch* the molecular bond. As the molecules progresses along the path to dissociative adsorption, its bonds weakens and must elongate to compensate F_c. The greater the angular momentum, the greater the bond elongation and thus the greater progress towards dissocation. Viewed from a different but equivalent perspective, the angular momentum contributes to the molecular potential a term V_c obtained by integrating the centrifugal force, i.e.

$$V_c(r; j) = \frac{j^2}{2\mu r^2}$$

Now suppose the molecule's trajectory is confined to the minimum energy path (i.e. the evolution is "adiabatic"). The molecule's state is then describable by a single *reaction coordinate s* which measures the progress along the minimum energy path (see

---

[5] Of course, quantum mechanically the only way to completely confine angular momentum about a single direction is to have *zero* total angular momentum. We ignore this complication, taking the scenario described here as a classical idealization, useful for illustration.
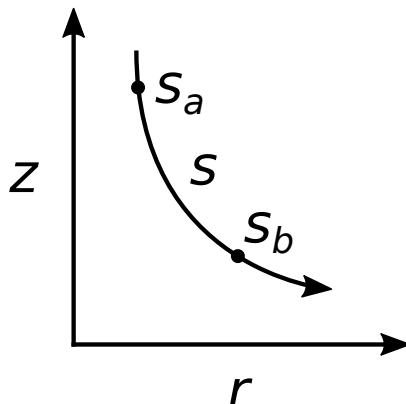
Figure 3.4: Diagram illustrating the reaction coordinate s. The molecular surface coordinate z and the bond length coordinate r are graphed for some interval along a hypothetical reaction path. In the example discussed in the text we consider an energetic barrier located early (s_a) and late (s_b) along the path to dissociation.

figure 3.4)[26, p.1610]. The evolution is then governed by a 1-dimensional potential $V(s; j)$ of the form

$$V(s; j) = V_o(s) + V_c(r(s); j)$$

where $V_o(s)$ is the potential at zero angular momentum. Refer now to figure 3.5. Suppose that $V_o(s)$ contains an energetic barrier at a point s_a *early* in the reaction path, so that the bond length is held more or less fixed at its gas phase value. It is seen then that angular momentum does little to facilitate dissociation, since at s_a there is no gradient in V_c about s. The picture changes however when the barrier is located at a point s_b *late* in the reaction path, where there is rapid variation in r with s. In this case we find that the energy barrier is effectively reduced for molecules with higher angular momentum j. This reduction is a manifestation of R–T coupling.

Note the assumptions that were necessary to make in order to conclude that angular momentum can enhance the likelihood of dissociation. In reality of course no surface is microscopically flat, so that there will in general be variation in the molecule-surface potential with the bond's azimuthal coordinate ϕ. Further, many molecules will impinge on the surface in a cartwheeling motion with their bonds rotating in and out of the surface plane[6]. When these factors are taken into account

---

[6] Finally, vibrational motion does not in general evolve adiabatically so that transfer of energy out of the rotational motion may in some cases *shorten* the bond length! This complication however
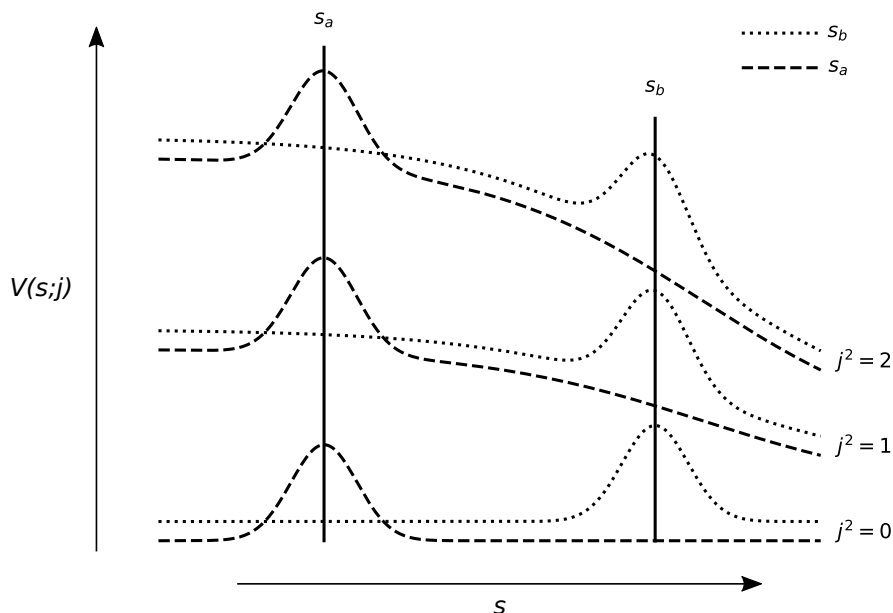
Figure 3.5: Schematic plot of the reaction path potential $V(s; j)$ for various angular momenta j. The dashed and dotted lines correspond to an early and late barrier, respectively (see figure 3.4), with the dotted raised slightly above the dashed for visibility. The height of the late barrier decreases with increasing j, indicating R–T coupling.

matters complicate considerably so that the conclusion is far from clear. In particular, these complications suggest that the *alignment* of the incoming molecules could significantly impact the extent of R–T transfer. A comparison of dissociation rates for cartwheeling and helicoptering molecules might then be revealing.

3.3.2 Dynamical Steering

For a classical system subject to a conservative force $\vec{F}(\vec{x}) = -\nabla V(\vec{x})$ Newton's equations take the form

$$m\ddot{\vec{x}} = m\dot{\vec{v}} = -\nabla V(\vec{x})$$

or for rotational motion we have, analagously

$$I\dot{\vec{\omega}} = -\nabla V(\theta, \phi)$$

---

is perhaps of lesser concern. Adiabaticity would be expected to apply on account of the very different time scales for rotational and vibrational motion.

where ω is the angular velocity. In either case we find that at each instant the system is adjusting each velocity component to point more in the direction of decreasing potential energy than it did the instant before. In this sense we can say that a molecule approaching a surface is being "steered" into the configuration most favorable for dissociation. Consider two impinging molecules A and B with equal velocity v_z but unequal angular velocities $\omega_A < \omega_B$[7]. The approximate time interval $\Delta t \sim \frac{\Delta z}{v_z}$ over which the molecule and surface interact is the same for both molecules and so then is the resulting change $\Delta\omega \sim \frac{|\nabla V|\Delta t}{I}$ in the angular velocity. We expect then the steering effect to have a greater influence on the molecule A than molecule B, since $\frac{\Delta\omega}{\omega_A} > \frac{\Delta\omega}{\omega_B}$. See figure 3.6 for an illustration.

Underlying dynamical steering – the concept that a potential naturally acts to reduce a particle's potential energy – is the tacit assumption that trajectories tend to get funnelled onto the least energy path. Were this so, we would expect decreasing influence of alignment on dissociation probability at decreasing incident velocities, the rough reasoning being that, given enough time, the surface can steer any molecule into the lowest energy orientation. This is opposite to what was concluded for R–T transfer, where enhancement of dissociation could be expected to correlate strongly with alignment. However, the above assumption regarding the funneling of trajectories is defective. In general a molecule finding itself at some moment on the least energy path will by inertia be carried off it, i.e. one can expect overshoot. Ultimately to determine to what extent dynamical steering is operative it is necessary to take into account the full details of the PES.

3.3.3 Experimental Evidence of R–T Transfer and Dynamical Steering

The two proposed rotational effects discussed above make two opposing predictions for the dependence of sticking on the rotational angular momentum on the impinging molecules. R–T transfer predicts an increase in dissociative adsorption with increasing angular momentum, while dynamical steering predicts a decrease.

In the following we describe measurements made for the adsorption probabilities for H_2 at $Pd(111)$, D_2 at $Cu(111)$, and our particular system of interest, i.e. H_2 at

---

[7] We ignore the linear velocity components parallel to the surface and the vectorial nature of the angular momentum for the purposes of illustration.
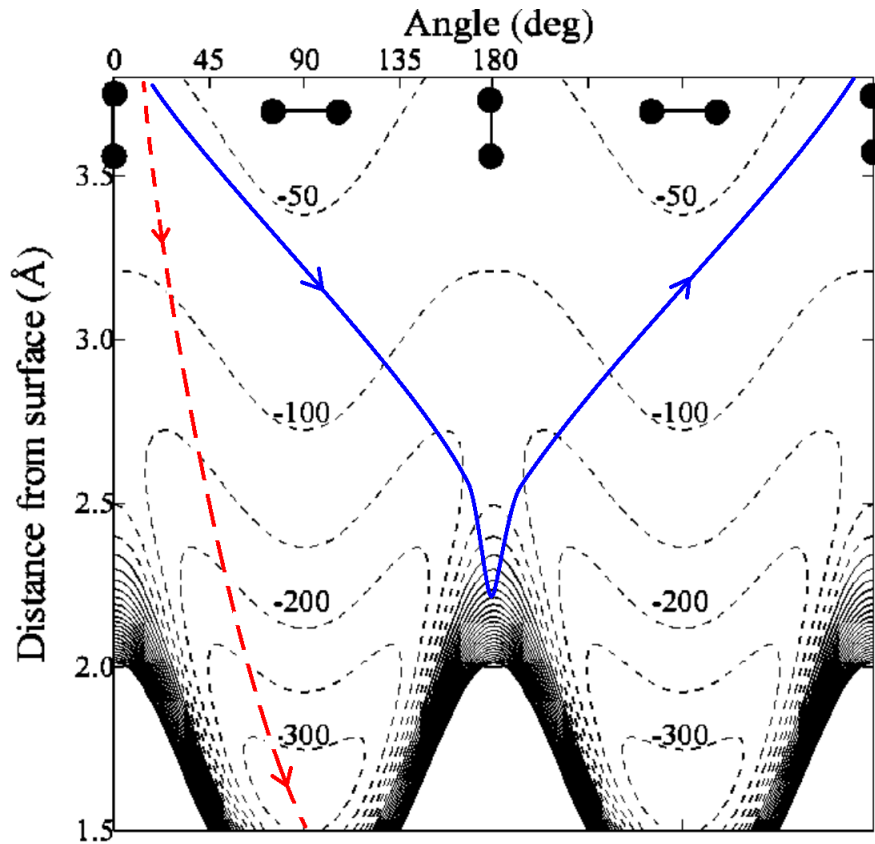
Figure 3.6: Illustration of dynamical steering. The vertical and horizontal axes correspond to the molecular-surface coordinate z and bond polar coordinate θ respectively. The thin dashed (solid) lines represent contours of constant negative (positive) potential energy (in meV) taken from a potential energy surface constructed by Crespos [36] for the H_2/Pd(111) system. On top of these contours we have superimposed two hypothetical trajectories. The red (dashed) trace represents a trajectory with low incident angular momentum that is steering into an orientation favorable for dissociation. The blue (solid) trace represents a trajectory with high incident angular momentum that resists steering and encounters a barrier which sends the molecule back into the gas phase. Adapted from [36] with the permission of AIP publishing.

Si(100). For the first two systems sticking at fixed incident translational energy is found to decrease at low angular momenta, reach a minimum, and then increase at higher angular momenta. This dependence is explained by the activation of dynamical steering and R–T transfer at low and high angular momenta, respectively. After discussing these two systems we describe the H_2/Si(100) results, which share many qualitative similarities with the results of the first two systems.

3.3.3.1 H_2/Pd(111)

By mixing different ratios of H_2 and an inert "antiseeding" gas of N_2 and using a variable temperature nozzle, Gostein and Sitz [37] were able to generate a beam of H_2 with fixed translational energy but variable rotational distributions. Using REMPI spectroscopy they were able to measure a j-dependent scattered flux and from a model of rotationally inelastic scattering arrive at an estimate for the sticking probability as a function of j. Their results are shown in figure 3.7. For all three incident energies there is an intermediate j_{min} for which sticking is minimized. Further, j_{min} increases with decreasing j. This is consistent with the expected behavior of dynamical steering, where a longer interaction time allows for steering of higher angular momentum.

3.3.3.2 D_2/Cu(111)

A similar result was discovered earlier by Michelson et al. for the D_2/Cu(111) system. The Cu(111) system differs qualitatively from the Pd(111) system in that dissociation is activated, i.e. exhibits an energetic barrier. Again using REMPI spectroscopy they measure the desorbing D_2 flux vs. j (figure 3.8a) for the different vibrational levels ν. From the principle of detailed balance [39] the sticking probability can be inferred. In particular the deviation from a pure Boltzmann distribution at the surface temperature indicates a j-depedence to the sticking coefficient. Fitting the results to a standard S-curve they arrive at figure 3.8b. Similar to Gostein and Sitz' results on Pd(111) we find with increasing j an initial decrease in sticking ($j = 0 \to 5$), followed by an increase ($j = 5 \to 10 \to 14$).

3.3.3.3 H_2/Si(100)

We conclude the section with some results on H_2/Si(100), our particular system of interest. In figure 3.9 we show a reproduction of desorption measurements by Shane
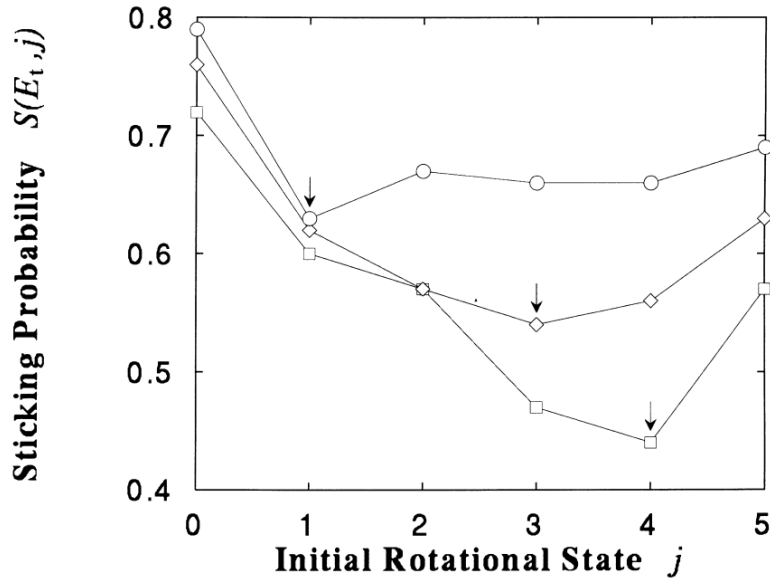
Figure 3.7: j-dependent sticking measurements by Gostein and Sitz [37] for H_2 incident on Pd(111). Squares, diamonds, and circles correspond to the mean incident translational energies of 55, 73, 94 meV respectively. Reprinted from [38] with permission from Elsevier.

(a)   (b)
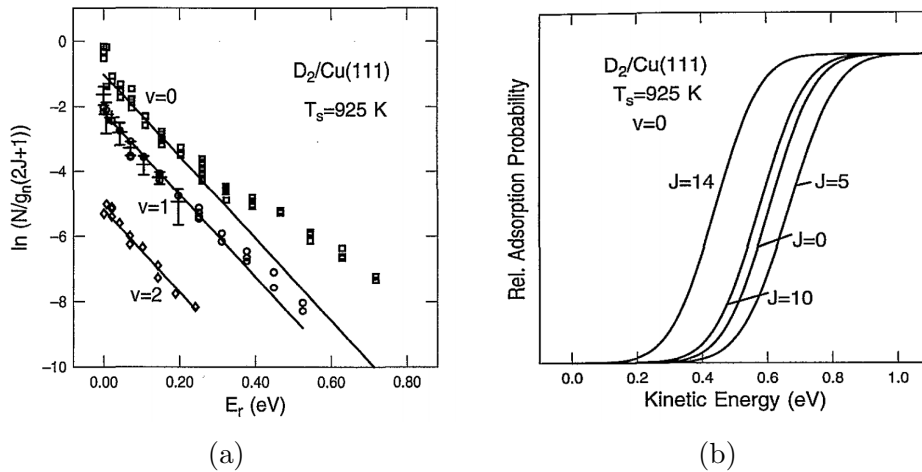
Figure 3.8: **(a)** j dependent measurements of the desorption flux of D_2 from Cu(111). The straight lines correspond to Boltzmann distributions at the surface temperature. **(b)** Sticking probabilities obtained from desorption data via detailed balance. Both figures reproduced from [40] with the permission of AIP Publishing.

et al. [41]. Focusing on the $\nu = 0$ results, we again find a similar positive curvature to the j-dependent desorption flux (measured again with REMPI), with slope at low j (0-3)running steeper than the corresponding Boltzmann distribution and gradually flattening at higher j (3-5) so that the slopes become approximately equal. The same interpretation of low $j \leftrightarrow$ dynamical steering / high $j \leftrightarrow$ R–T coupling is thus applicable, though for the sake of an alternative perspective we can connect the findings to the rotational structure of the transition state. Assuming that the rotational motion evolves adiabatically as molecules move beyond the transition state and into the gas phase, the steep slope at low j then implies that the spacing of rotational levels at the transition state for those j are signficantly larger than their gas phase spacings, or in other words that the rotational motion is hindered. For the range of j at which the slope matches the Boltzmann prediction the molecules can conversely be thought to be rotating more or less freely at the transition state. By noting the rotational energy $E_j = Bj(j+1)$ at which this slope matching occurs we gain a rough estimate of the corrugation in the PES with the angular coordinates θ, ϕ at the transition state.

3.4   Gas-Surface Studies with Aligned Molecules

The previous section outlined the role played by the *total* angular momentum, represented quantum mechanically by the quantum number j in the dissociative adsorption of diatomic molecules at surfaces. Some effects were introduced to explain how j may influence reactivity, though for each of these effects it was also pointed out that the molecule's *alignment*, represented quantum mechanically by the quantum number m, might also play a signficant role. A thorough explanation of quantum mechanical alignment is given in chapter 4.

In this section we survey some existing results concerning the role of alignment in molecule-molecule and molecule-surface interactions. The first two discussed use laser spectroscopy to detect alignment in D_2 molecules desorbing from Pd(100) [42] and Cu(111) [43]. The measurements are then connected to the concepts of R–T coupling dynamical steering and dynamical steering described in the previous section. From here we review a series of experiments involving the production of aligned molecules, beginning with an experiment measuring the survival of alignment in col-
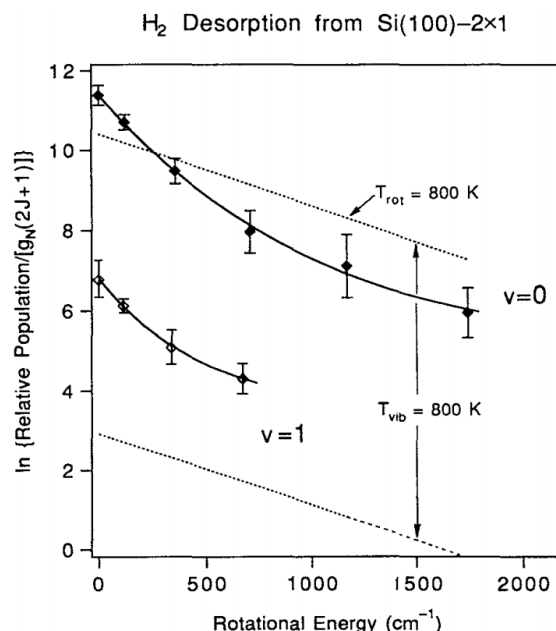
Figure 3.9: Measurements by Shane et al. [41] of the j-dependent flux at different vibrational levels ν for D_2 desorbing from Si(100). The straight dotted lines correspond to a Boltzmann distribution at the surface temperature. Reproduced from [41] with the permission of AIP Publishing.

lisions between N_2 molecules before moving on to molecule-surface studies utilizing aligned molecular beams. The first two of these measure the dependence of sticking on alignment, while the third measures the effect of alignment on the scattering distribution. Through these studies the reader is hopefully convinced of the relevance of alignment in surface chemistry.

3.4.1   Alignment in desorption from D_2/Pd(100) and D_2/Cu(111)

The investigators in these experiments [42], [43] measure the alignment of desorbing molecules in a manner more or less identical to our technique (see section 4.7). In essence alignment is detected by measuring modulation in the molecular response to probing laser radiation with varying laser polarization. The results are shown in figure 3.10.

Results are stated in terms of the measured quadrupole alignment (section 4.4), where positive and negative quadrupole alignments indicate helicoptering and cartwheel-
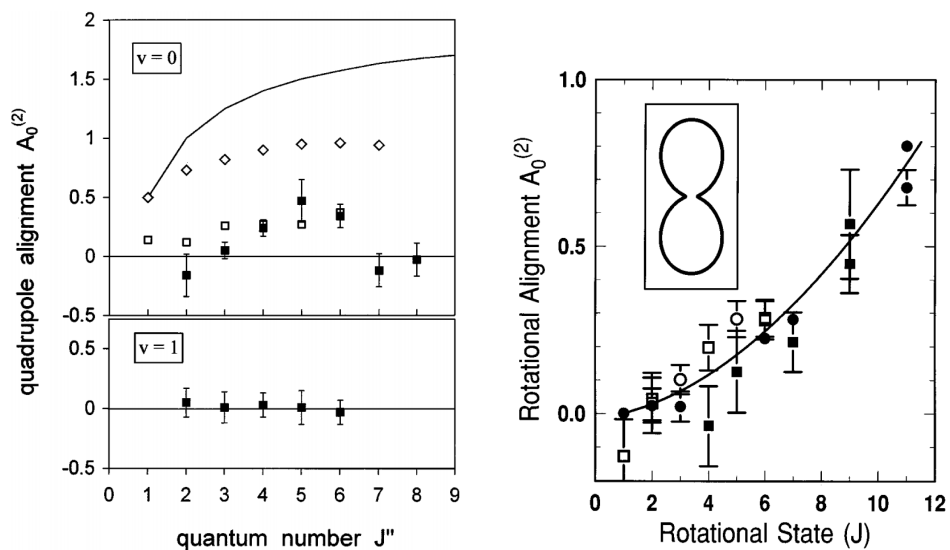
(a) $H_2/Pd(100)$. Solid squares denote experimental values, while open squares and diamonds denote theoretical predictions for the Pd(100) and Cu(111) surfaces respectively. The $\nu = 0$ and $\nu = 1$ data were acquired at surface temperatures $T_s = 690K$ and $T_s = 900K$ respectively.

(b) $H_2/Cu(111)$. The circle and square markers denote P and R branch transitions respectively, while solid and open markers denote $\nu = 0$ and $\nu = 1$ respectively.

Figure 3.10: Measurement of the quadrupole alignment of desorbing D_2 molecules from **(a)** Pd(100) and **(b)** Cu(111). Reproduced from [42] and [43] with permission from APS and AIP respectively.

ing motion respectively. The results (when combined with detailed balance) in both cases are found to generally reinforce the interpretation put forth for the j-resolved results from the previous section. Namely, at low j, cartwheeling (i.e. end-on) molecules are steered into the helicoptering (i.e. broadside) orientation favorable for dissociation, while, at higher j, R–T transfer preferentially enhances dissociation for incident helicopters.

3.4.2 Survival of Alignment in $N_2 - N_2$ Collisions

Using a preparation and detection technique equivalent to our own (see sections 4.6 and 4.7), Sitz and Farrow in [44] monitored the evolution of alignment in vibrationally excited ($\nu = 1$) N_2 molecule as they collide with each other and their unpumped
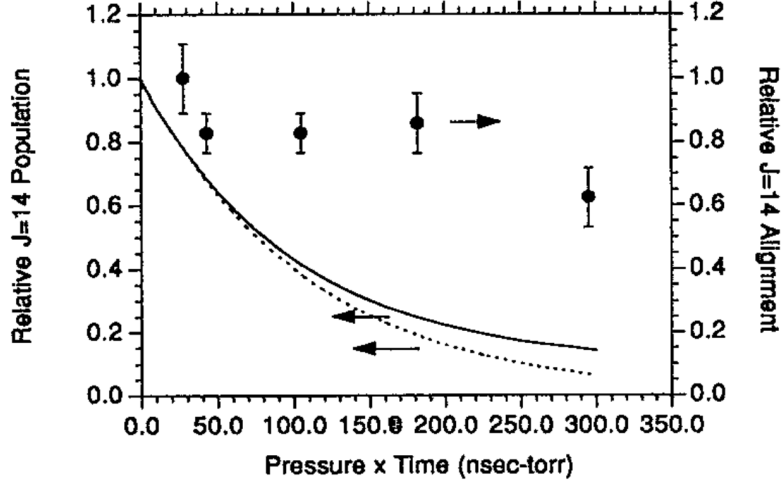
Figure 3.11: Rotational alignment in the $j = 14$ rotational level vs. pressure-time product. Markers indicate fraction of initial quadrupole alignment. The solid line represents overall population while the dotted line represents population excess originating from the pumping process. At late times the $j = 14$ population is composed largely of molecules scattering in from unpumped $\nu = 1$ rotational levels. Reproduced from [44] with permission from AIP.

($\nu = 0$) neighbors. Figure 3.11 illustrates the main findings. Vibrationally excited molecules are prepared initially in the $j = 14$ rotational state and as time progresses these molecules redistribute themselves among the $\nu = 1$ rotational states as they seek equilibrium. The time scale[8] over which this occurs, which we will denote T_{eq}, was determined by the authors in a previous study[11]. What was found in [44] was that the alignment of the vibrationally excited molecules persisted well beyond T_{eq}, leading the authors to conclude that rotational alignment was robust enough to survive transfer not only away from but also back to the initially pumped state.

3.4.3 Dissociation of O_2 on Si(100)

Exploiting the non-zero electronic spin of O_2 in its ground electronic state, Kurahashi and Yamauchi [45] were able to use magnetic fields to filter out the $|j = 2, m = 2\rangle$ spin-rotation state from a molecular beam, where the associated quantization axis is controlled by varying the direction of the field at the filter exit. Note that j and m here refer to the angular momentum vector $\vec{J}$ given by the sum $\vec{K} + \vec{S}$ of the rotational and

---

[8] or, more precisely, pressure-time product

spin angular momentum of the molecule, respectively. Because O_2 possesses nearly pure Hund's case (b) angular momentum coupling, the rotational state of a $|2, 2\rangle$ molecule turns out to high accuracy to be a pure Y_1^1 spherical harmonic.

Using these filtered beams, the authors studied the dependence of silicon oxidation rate on the direction of the quantization axis [46]. A sample measurement is given in figure 3.12. Toggling the magnetic field at the filter exit between the (100) (surface normal) and (011) (dimer parallel) directions induces large changes in sticking. From taking measures at different incident energies and surface temperatures the authors are able to associate the "direct", i.e. single bounce adsorption processes with the observed alignment sensitivity. The expected role of rotation in O_2 adsorption, it should be mentioned, differs from that for H_2 due to their large disparity in mass (16:1) and thus moment of inertia. At low $\langle |\vec{K}|^2 \rangle$ the O_2 bond angle is essentially fixed over the course of a direct interaction. Rotational angular momentum is thus expected to be relevant only so far as it determines the distribution of bond angles. With this in mind, the authors model adsorption as a step function in the bond polar angle θ, i.e. for some θ_o and $\Delta\theta$ we have for the adsorption probability $P(\theta)$

$$
P(\theta) = \begin{cases} 1 & \theta_o - \Delta\theta < \theta < \theta_o + \Delta\theta \\ 0 & \text{else} \end{cases}
$$

and find their measurements consistent with a narrow $\Delta\theta = 30°$ cone of acceptance about $\theta_o = 90°$ (i.e. bond in-plane).

3.4.4   Methane (CH_4) Dissociation on Nickel

For a diatomic molecule the direction of its single mode of vibration is constrained to lie perpendicular to its angular momentum. For polyatomic molecules the situation is different so that we can speak separately of rotational and vibrational alignment. Using laser pumping, Yoder et al. [48] excite CH_4 molecules to ν_3 anti-symmetric stretching mode. By varying the laser wavelength, the molecules are excited from different ground $\nu = 0$ vibrational state rotational levels. The different operative selection rules for the different transitions result in differing combinations of rotational and vibrational alignment in the excited vibrational state.

For each transition the authors measure the sensitivity of the adsorption probability to the pump laser polarization. The senstivity is quantified by the parameter
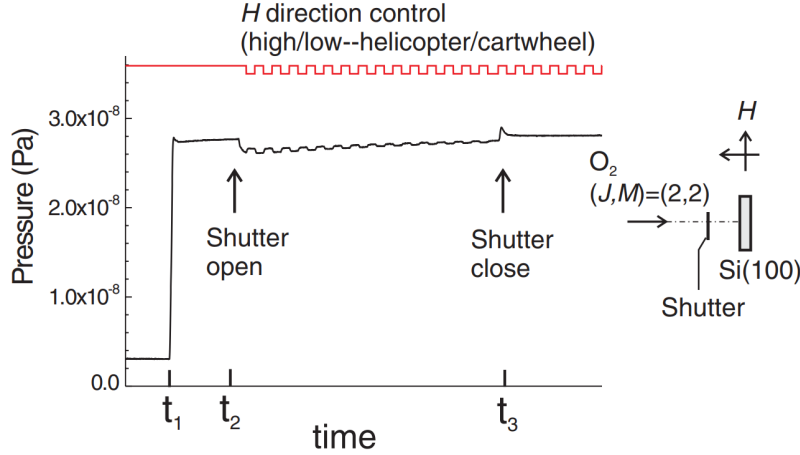
Figure 3.12: Variation in oxidation of Si(100) with direction of incident O_2 $\vec{J}$. Adsorption probabilities are determined using a King and Wells [47] method so that decreases in pressure correspond to increased sticking. Clear variation in pressure with magnetic field (quantization axis) direction indicate strong dependence of sticking on alignment. Reproduced from [46] with permission from APS.

$\Delta_p \equiv \frac{S_\parallel - S_\perp}{S_\parallel + S_\perp}$ where $S_\parallel$ and $S_\perp$ is the sticking probability with the pump laser polarization parallel and perpendicular to the surface normal respectively. In figure 3.13 Δ_p for each transition is compared to the corresponding rotational and vibrational alignments, denoted respectively by A_0^2 and β_{axis}, produced by the transition. It is clear from the figure that the Δ_p correlates far better with vibrational alignment than rotational, suggesting that bringing the excited bond into a favorable geometry plays a larger role in dissociative adsorption than does coupling of angular momentum to the surface.

3.4.5 H_2 Scattering from Cu(111) and Cu(115)

We conclude the chapter with an experiment that, like our own experiment, probes the *scattering* behavior (as opposed to reactivity) of H_2 molecules for different incident rotational alignments, though the state preparation and detection techniques differ greatly from ours. Similar to Kurahashi et al. [46], Godsi et al. [49] using a hexapole magnet were able to filter out all but the $|I = 1, m_I = 1\rangle|J = 1, m_J = 1\rangle$ spin-rotation level from a H_2 molecular beam, where $\vec{I}$ and $\vec{J}$ are the angular mometa of the nuclear spin and rotation, respectively. The filtered beam is then subjected to an electromagnet which coherently evolves the spin-rotation state. Owing to the
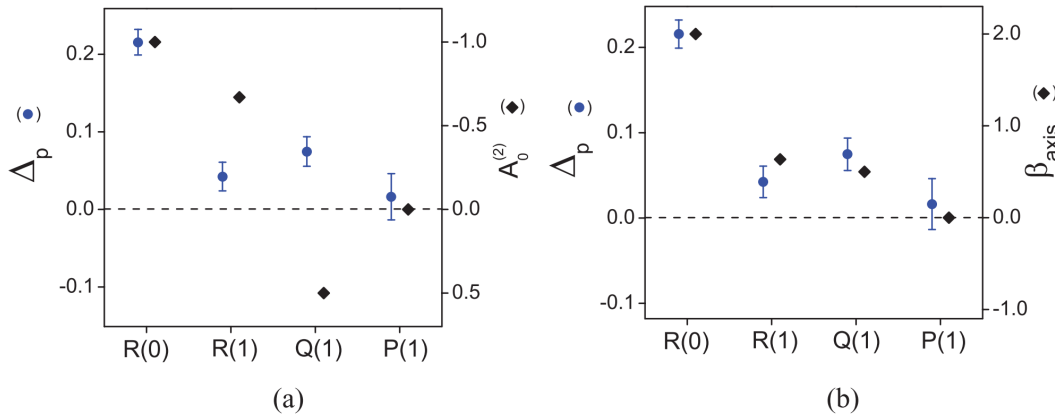
Figure 3.13: Polarization sensitivity for the various transitions. For comparison, the rotational alignment A_0^2 and vibrational alignment β_{axis} are plotted alongside in **(a)** and **(b)**, respectively. The P(1) transition produces $j = 0$ (i.e. unaligned) molecules and serves as a control. Reproduced from [48] with permission from AIP.

complexity of the mutual interaction between the different nuclear angular momenta and the magnetic field, the precise nature of the evolution is complicated but qualitatively the electromagnet acts to coherently rotate the molecule's rotational angular momentum.

After passing through the electromagnet, the molecules are scattered off of a flat (Cu(111)) or stepped (Cu(511)) copper surface, and the scattered flux is monitored at the specular angle as the strength of the electromagnet and thus the incident molecule rotational state is varied. The results are shown in figure 3.14. The detailed shape of the curve can only be rationalized by taking into account the complete spin-rotation Hamiltonian, and the authors choose to give context to their results by comparing to the curve predicted from full quantum simulation of the state-preparation and scattering stages.

However, from simple comparison of the modulation *depth* for the different copper surface orientations we can conclude that scattering from the stepped surface exhibits significantly larger sensivity to rotational alignment than the flat surface. This in turn implies an increase in corrugation in the rotational potential at step edges, a conclusion consistent with accompanying *ab initio* calculations that found H_2 molecules can penetrate closer to the Cu(111) surface at step edges than at terraces.
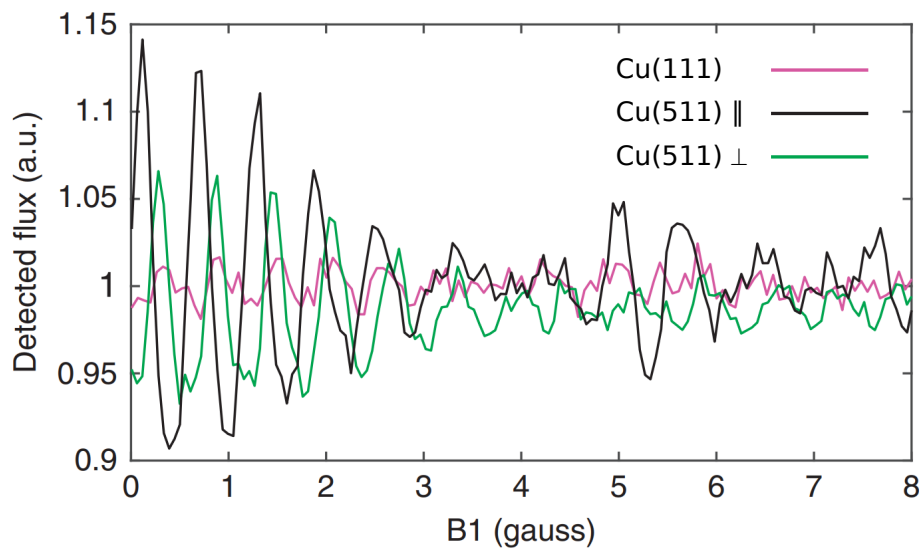
Figure 3.14: Dependence of specular scattered flux on the strength of the magnetic field $B1$ that rotates the incoming states. The parallel ($\parallel$) and perpendicular ($\perp$) designations indicate the direction of the atomic steps with respect to the scattering plane. Reproduced from [49].

Chapter Four: Alignment

In our experiment we measure the influence of molecule-surface interaction on the *alignment* of the molecule's *angular momentum.* This chapter, dedicated to the quantum mechanical study of angular momentum and alignment, is included in order to develop the context necessary to discuss our measurements and their interpretation. A notoriously heiroglyphic air tends to surround the subject of quantum mechanical angular momentum, and the aim of the chapter is to lift some of this fog by introducing some simple fundamental objects and operations and showing how larger, more complex objects can be constructed. We introduce only the concepts necessary to discuss our experimental results, so no attempt will be made at full completeness or rigor. The sections of this chapter are organized as follows:

- *Angular momentum eigenstates*, the fundamental units of quantum mechanical angular momentum, are introduced, and then

- we show how to *combine* angular momentum eigenstates into states and operators that themselves behave as angular momentum eigenstates.

- The *density operator*, which provides a convenient link between experiment and theory, is motivated and then introduced, after which

- we show how the density operator permits a simple and powerful description of alignment in terms of its *multipole expansion.*

- From there we define the *two-photon operator*, which acts to transfer molecules between different multiplets, and describe how the action of the operator modifies the alignment of molecules.

- Finally we relate the concepts introduced in this chapter to the pumping and probing stages of our experiment. The two stages are seen to be essentially opposite of one another. We describe the alignment produced in the pumping stage and derive formulas relating our probe measurements to the multipole moments of the probed molecules.

4.1 Angular Momentum Eigenstates

4.1.1 Angular Momentum Eigenstates

Rotational angular momentum is a *vector* quantity, possessing both a magnitude and direction. Quantum mechanically an object's angular momentum is characterized by a pair j, m of quantum numbers, where

- j is the *total angular momentum* quantum number and encodes the magnitude of the object's angular momentum. More precisely, a state $|j, m\rangle$ with quantum number j (the m quantum number is explained below) has a definite total squared angular momentum so that

$$J^2|j, m\rangle = \hbar^2 j(j+1)|j, m\rangle, \tag{4.1}$$

  where $\vec{J}$ is any triplet of operators (J_1, J_2, J_3) satisfying the commutation relations $[J_a, J_b] = i\hbar \sum_{i=c}^{3} \varepsilon_{abc} J_c$, where $a, b \in \{1, 2, 3\}$. The vector notation $\vec{J}$ is justified by the fact that from some triplet $\vec{J}$ we can obtain another triplet $\vec{J}'$ satisfying the commutation relations by applying a rotation matrix O, i.e. $J_i \to J_i' = \sum_{j=1}^{3} O_{ij} J_j$ where $O^{-1} = O^T$ and $\det(O) = 1$.

  Rotational angular momentum quantum numbers, associated with the operator $\vec{J} = \vec{r} \times \vec{p}$, are constrained to non-negative integer values ($j = 0, 1, 2, \ldots$), while *spin* angular momenta can take on positive half integer ($j = 1/2, 3/2, \ldots$) values as well.

- m is the *magnetic* quantum number [1] and encodes the direction of the angular momentum vector. States of quantum number m have definite projection of angular momentum about some direction $\hat{n}$ referred to as the *quantization axis* so that for a state $|j, m\rangle$ we have

$$\vec{J} \cdot \hat{n}|j, m\rangle = \hbar m|j, m\rangle, \tag{4.2}$$

  Once the quantization axis is selected, it is common to reorient $\vec{J}$ via an appropriate orthogonal transformation so that $\hat{n}$ is parallel to J_3, along with an establishment of coordinate axes so that $J_1 \to J_x,\ J_2 \to J_y,\ J_3 \to J_z$.

---

[1] This terminology originates from atomic spectroscopy. Two atomic states with all but their m quantum numbers the same will split apart in energy under application of a magnetic field.

For a given j quantum number, the possible m quantum numbers are $m = -j, -j+1, \ldots, j-1, j$. The fact that an object can not occupy a state with all its angular momentum pointing in a single direction, i.e. that for all $j \neq 0$ we have

$$\langle \left(\vec{J} \cdot \hat{n} \right)^2 \rangle = \hbar^2 m^2 \leq \hbar^2 j^2 < \hbar^2 j(j+1) = \langle \vec{J}^2 \rangle$$

can be viewed as a consequence of Heisenberg's uncertainty principle.

We use the term angular momentum eigenstate to refer to states $|j, m\rangle$ of definite j and m quantum numbers. We further require (along with an additional final requirement discussed below) that the angular momentum eigenstates be normalized so that

$$\langle j, m | j, m \rangle = 1 \tag{4.3}$$

4.1.2   Angular Momentum Multiplets

It should be clarified that an arbitrary state may not possess definite angular momentum but in general lies in some superposition angular momentum states, i.e. can be expanded in a basis of angular momentum *multiplets*

$$\begin{aligned}
\{ \quad &|j_1, -j_1\rangle, \quad |j_1, -j_1 + 1\rangle, \quad \ldots \quad |j_1, j_1 - 1\rangle \quad |j_1, j_1\rangle, \\
&|j_2, -j_2\rangle, \quad |j_2, -j_2 + 1\rangle, \quad \ldots \quad |j_2, j_2 - 1\rangle \quad |j_2, j_2\rangle, \\
&\vdots \\
&|j_n, -j_n\rangle, \quad |j_n, -j_n + 1\rangle, \quad \ldots \quad |j_n, j_n - 1\rangle \quad |j_n, j_n\rangle, \\
&\vdots \qquad\qquad\qquad\qquad\qquad\qquad\qquad\qquad\qquad\qquad \}
\end{aligned}$$

where the n index identifies the multiplet. Two states belong in the same multiplet if one can be reached from the other by successive application of *raising* (J_+) or *lowering* (J_-) operators, where

$$J_\pm \equiv J_x \pm i J_y$$

The ladder operators also serve to fix a phase ambiguity in our definition of the $|j, m\rangle$ states. Given a quantization axis $\hat{n}$ and a state $|j, m\rangle$ with the properties (4.1), (4.2), and (4.3), we can generate another state with the same properties by multiplying by some phase factor $e^{i\delta}$ so that $|j, m\rangle \rightarrow e^{i\delta} |j, m\rangle$.

We can fix the relative phases among the different $|j, m\rangle$ states in a multiplet by requiring

$$J_{\pm}|j, m\rangle = \sqrt{(j \mp m)(j \pm m + 1)}|j, m \pm 1\rangle \tag{4.4}$$

This convention, known as the Condon-Shortley phase convention[50], has the benefit of making all the Clebsch-Gordan coefficients (to be discussed in section 4.2) real. Equation (4.4) together with equation (4.2) actually imply (4.1) so that we can take equations (4.4) and (4.2) along with the normalization condition (4.3) as the definition of the angular momentum eigenstates/multiplets $|j, m\rangle$.

Equivalently, angular momentum states can be grouped into multiplets by examining their behavior under rotations. In quantum mechanics rotations are represented as operators $\mathcal{D}(\omega)$, where $\omega \equiv (\hat{n}, \phi)$ is a rotation by angle ϕ about the axis $\hat{n}$. Rotation operators can be written in terms of the angular momentum operator via

$$\mathcal{D}(\omega) = e^{\frac{\vec{J} \cdot \hat{n} \phi}{i\hbar}}$$

The action of a rotation operator $\hat{D}(\omega)$ on a state $|jm\rangle$ takes the following simplified form:

$$\mathcal{D}(\omega)|jm\rangle = \sum_{m'=-j}^{+j} D_{m'm}^{j}(\omega)|jm'\rangle \tag{4.5}$$

where the coefficients $D_{mm'}^{j}(\omega)$ form a $(2j + 1) \times (2j + 1)$ matrix known as the (j^{th}) *Wigner D-matrix*. From equation (4.5) it can be seen that states in a multiplet have the property of transforming into each other under rotations. We can in fact make the stronger statement that any state in the some multiplet (i.e. in the span of some $|j, m\rangle$, $m = -j, \ldots, +j$) can be transformed into any other state in the multiplet by some appropriately weighted sum of rotation operators. In this sense states in a multiplet are said to have *definite symmetry under rotations*[2].

4.2 Addition of Angular Momentum

Suppose a composite system consists of two interacting subsystems, one with angular momentum j_1 with respect to its angular momentum operator $\vec{J}_1$ and the other with angular momentum j_2 and $\vec{J}_2$ with respect to its angular momentum operator $\vec{J}_2$.

---

[2]in mathematical terms we could say that multiplets form *irreducible representations* of the rotation group

For instance, the first angular momentum $\vec{J}_1$ may represent the rotational angular momentum of a molecule, taking only integer values, while $\vec{J}_2$ may represent the spin of one the molecule's nuclei, which, depending on the nucleus, may take integer or half integer values. We are interested in grouping states in the composite system into multiplets with respect to the *total* angular momentum operator $\vec{J}_1 + \vec{J}_2$.[3]

A basis for this system can be constructed from the tensor products $|j_1, m_1\rangle \otimes |j_2, m_2\rangle$, where $m_1 = -j_1, -j_1+1, \ldots, j_1-1, j_1$ and $m_2 = -j_2, -j_2+1, \ldots, j_2-1, j_2$.[51] These basis vectors, however, are not in general angular momentum eigenstates with respect to the $\vec{J}_1 + \vec{J}_2$ operator. The $\vec{J}_1 + \vec{J}_2$ angular momentum eigenstates, denoted $|j, m\rangle_\otimes$ are obtained via the linear transformation

$$|j_1, m_1\rangle \otimes |j_2, m_2\rangle \rightarrow |j, m\rangle_\otimes \equiv \sum_{m_1=-j_1}^{+j_1} \sum_{m_2=-j_2}^{+j_2} c(j_1, m_1; j_2, m_2|j, m)|j_1, m_1\rangle \otimes |j_2, m_2\rangle$$

$$(4.6)$$

where the $c(j_1, m_1; j_2, m_2|j, m)$ are known as the *Clebsch-Gordan coefficients*[52].

The following are some properties of the Clebsch-Gordan coefficients that we will use:

CG.1 $c(j_1, m_1; j_2, m_2|j, m) = 0$ unless $j \in \{|j_1 - j_2|, |j_1 - j_2| + 1, \ldots, j_1 + j_2 - 1, j_1 + j_2\}$

CG.2 $c(j_1, m_1; j_2, m_2|j, m) = 0$ unless $m = m_1 + m_2$

CG.3 In the Condon-Shortley phase convention the $c(j_1, m_1; j_2, m_2|j, m)$ are purely real.

CG.4 The $c(j_1, m_1; j_2, m_2|j, m)$ at fixed j_1 and j_2 comprise a unitary matrix so that, combined with the properties CG.1 and CG.3, we get

$$|j_1, m_1\rangle \otimes |j_2, m_2\rangle = \sum_{j=|j_1-j_2|}^{j_1+j_2} \sum_{m=-j}^{+j} c(j_1, m_1; j_2, m_2|j, m)|j, m\rangle \qquad (4.7)$$

---

[3]or, equivalently, we are interested in decomposing the system into multiplets of definite symmetry with respect to *simultaneous* rotation of the two subsystems.

4.2.1 Applications of Addition of Angular Momentum

4.2.1.1 Outer Products $|j_1, m_1\rangle\langle j_2, m_2|$ and Spherical Tensors

Angular momentum addition finds application in the decomposition of operators into *spherical tensors*, a concept we will use extensively in the remainder of the dissertation. Consider an operator taking the form of a single outer product $|j_1, m_1\rangle\langle j_2, m_2|$, where $|j_1, m_1\rangle$ and $|j_2, m_2\rangle$ are states of definite angular momentum with respect to the same angular momentum operator $\vec{J}$.[4] The outer product can also be considered a tensor product, i.e. we have the linear correspondence

$$|j_1, m_1\rangle\langle j_2, m_2| \cong |j_1, m_1\rangle \otimes \langle j_2, m_2| \tag{4.8}$$

However, the components of $\vec{J}$ do not satisfy the commutation relations as operators on the bras $\langle j, m|$, though its negation $-\vec{J}$ does. As a consequence it is the states $(-1)^{-(j_2+m_2)}\langle j_2, -m_2|$ that possess the quantum numbers j_2 and m_2. After some rearrangement we can write the tensor product in equation (4.8) so that it takes the form that lends itself to application of equation (4.7). Explicitly

$$
\begin{aligned}
|j_1, m_1\rangle\langle j_2, m_2| &\cong |j_1, m_1\rangle\langle j_2, m_2| \\
&= (-1)^{j_2-m_2}|j_1, m_1\rangle \otimes \left((-1)^{-(j_2-m_2)}\langle j_2, -(-m_2)|\right) \\
&\cong (-1)^{j_2-m_2}\sum_{k=|j_1-j_2|}^{j_1+j_2}\sum_{q=-k}^{+k} c(j_1, m_1; j_2, -m_2|k, q)t_q^k
\end{aligned}
\tag{4.9}
$$

where the operators t_q^k are operators with definite angular momentum in that the following relations hold:

$$[\vec{J}\cdot\hat{n}, t_q^k] = \hbar q t_q^k \tag{4.10}$$

$$[\vec{J}_\pm, t_q^k] = \hbar\sqrt{(k \mp q)(k \pm q + 1)}t_{q\pm 1}^k \tag{4.11}$$

$$\mathrm{Tr}\left(\left(t_{q'}^{k'}\right)^\dagger t_q^k\right) = \delta_{k'k}\delta_{q'q} \tag{4.12}$$

Where Tr denotes the trace operation. Note the similarity of the above with equations (4.2), (4.4), (4.3) defining the angular momentum eigenstates. The similarity is actually a full equivalence when we recognize that

---

[4]The results (with slight modification) also apply should the $|j_1, m_1\rangle$ and $|j_2, m_2\rangle$ associate with different angular momentum operators $\vec{J}_1$ and $\vec{J}_2$.

- operators are themselves vectors (possessing the operations of addition and scalar multiplication) with

- an inner product between two operators A and B given by

$$\mathrm{Tr}\left(B^\dagger A\right) \tag{4.13}$$

  and

- an angular momentum "super-operator" (operator on operators) defined by the prescription $A \to [\vec{J}, A]$.

.

The t_q^k can be written in terms of the outer products $|j_1, m_1\rangle\langle j_2, m_2|$:

$$t_q^k = \sum_{m_1=-j_1}^{+j_1} \sum_{m_2=-j_2}^{+j_2} (-1)^{j_2-m_2} c(j_1, m_1; j_2, -m_2|k, q)|j_1, m_1\rangle\langle j_2, m_2|$$

and in fact form a basis for the $|j_1, m_1\rangle\langle j_2, m_2|$.

In general, for fixed k, any collection of operators t_q^k where $q = -k, -k+1, \ldots, k-1, k$ satisfying equations (4.10) and (4.11) is known as a spherical tensor of type k. Note that property (4.12) is omitted so that a spherical tensor in general need not be normalized.

Equivalently we could define spherical tensors as operators t_q^k that have the following behavior under an arbitrary rotation ω:

$$\mathcal{D}(\omega)t_q^k\mathcal{D}^\dagger(\omega) = \sum_{q'=-k}^{+k} D(\omega)_{q'q}^k t_{q'}^k \tag{4.14}$$

From an angular momentum operator $\vec{J}$ we can obtain a spherical tensor $\mathcal{J}_q^1$ of type $k = 1$ from the following associations:

- $\mathcal{J}_0 \equiv J_z$

- $\mathcal{J}_{\pm 1} \equiv J_\pm$

If we multiply $\vec{J}$ by a matrix encoding a rotation ω, this produces a new angular momentum operator $\vec{J}'$ with a corresponding spherical tensor $\mathcal{J}_q'^1$ that can be expanded

in terms of the $\mathcal{J}_q^1$ via

$$\mathcal{J'}_q^1 = \sum_{q'=-1}^{+1} D_{q'q}^1(\omega)\mathcal{J}_{q'}^1 = \mathcal{D}(\omega)\mathcal{J}_q^1 \mathcal{D}^\dagger(\omega)$$

From the above it follows that for every multiplet $|j, m\rangle$ with associated angular momentum operator $\vec{J}$ we obtain a multiplet $|j, m\rangle'$ with associated angular momentum operator $\vec{J'}$ by the rule

$$|j, m\rangle' = D_{m'm}^j(\omega)|j, m'\rangle = \mathcal{D}(\omega)|j, m\rangle \tag{4.15}$$

To see that the $|j, m\rangle'$ are indeed angular momentum multiplets with associated angular momentum operator $\vec{J'}$ we note that for any m,m', and q we have

$$'\langle j, m'|\mathcal{J'}_q^1|j, m\rangle'$$
$$=\langle j, m'|\mathcal{D}^\dagger(\omega)\mathcal{D}(\omega)\mathcal{J}_q^1\mathcal{D}^\dagger(\omega)\mathcal{D}(\omega)|j, m\rangle$$
$$=\langle j, m'|\mathcal{J}_q^1|j, m\rangle$$

where $'\langle j, m'| \equiv [|j, m'\rangle']^\dagger$, and the last step exploits the unitarity of the rotation operators $\mathcal{D}(\omega)$. Recalling then the definition of the $\mathcal{J}_q^1$, we find the $|j, m\rangle'$ as defined obey the three relations (4.2), (4.4), and (4.3) required of angular momentum multiplets with associated angular momentum operator $\vec{J'}$.

4.2.1.2 Products of Spherical Tensors $t_q^k \tilde{t}_{q'}^{k'}$

The product of two spherical tensors t_q^k and $\tilde{t}_{q'}^{k'}$ also admits a spherical tensor decomposition. That is, from the set of products $t_q^k \tilde{t}_{q'}^{k'}$, $q = -k, \ldots, +k$, $q' = -k', \ldots, +k'$ we can form special combinations

$$\left[t^k \tilde{t}^{k'}\right]_{q''}^{k''} \equiv \sum_{q=-k}^{+k} \sum_{q'=-k'}^{+k'} c(k, q; k', q'|k'', q'')t_q^k \tilde{t}_{q'}^{k'} \tag{4.16}$$

that obey the defining relation (4.14) for spherical tensors.

Conversely the product of two spherical components $t_q^k \tilde{t}_{q'}^{k'}$ can be expanded in terms of the $\left[t^k \tilde{t}^{k'}\right]_{q''}^{k''}$ in a fashion analogous to (4.7):

$$t_q^k \tilde{t}_{q'}^{k'} = \sum_{k''=|k'-k|}^{k'+k} \sum_{q''=-k''}^{+k''} c(k, q; k', q'|k'', q'') \left[t^k \tilde{t}^{k'}\right]_{q''}^{k''} \tag{4.17}$$

However, since the product of two operators is not strictly a tensor product, the $\left[t^k \tilde{t}^{k'}\right]_{q''}^{k''}$ are *not* in general linearly independent, and indeed some multiplets may be zero.

Consider as an example the case of products of Pauli spin matrices $\sigma_1, \sigma_2, \sigma_3$. The spin matrices together constitute a basis of a $k = 1$ spherical tensor, so that from CG.1 we may expect to generate spherical tensors of type $k=0$, 1, and 2. However, from the commutation and anticommutation relations

$$[\sigma_i, \sigma_j] = 2i \sum_{k=1}^{3} \varepsilon_{ijk} \sigma_k$$

$$\{\sigma_i, \sigma_j\} = 2\delta_{ij}I$$

we find that products of the spin matrices lie in the span of $\{I, \sigma_1, \sigma_2, \sigma_3\}$. Since I is a spherical tensor of type $k = 0$, we find that the spherical tensor decomposition of a product $\sigma_i \sigma_j$ does not happen to contain any terms of $k = 2$ symmetry.

4.2.1.3   Products of Spherical Tensors and Angular Momentum Eigenstates $t_q^k |j, m\rangle$

For reasons analogous to those discussed in 4.2.1.2 the states obtained by the action $t_q^k |j, m\rangle$ of a spherical tensor t_q^k on an angular momentum multiplet $|j, m\rangle$ admit a decomposition into "pseudo"-angular momentum eigenstates in the sense that the states $|j', m'\rangle$ defined by

$$|j', m'\rangle \equiv \sum_{q=-k}^{+k} \sum_{m=-j}^{+j} c(j, m; k, q|j', m') t_q^k |j, m\rangle \tag{4.18}$$

obey relations (4.2) and (4.4) but are not necessarily normalized and for some $j' = |j - k|, \ldots, j + k$ may even vanish.

4.2.1.4   Inner Products of Angular Momentum Eigenstates $\langle j, m | j', m' \rangle$

An even stronger result can be obtained for inner products of angular momentum eigenstates $\langle j, m | j', m' \rangle$, again by applying the arguments of 4.2.1.2. In this case we get schematically a decomposition similar to 4.2.1.1, i.e.[5]

$$\langle j, m | j', m' \rangle = \sum_{j''=|j-j'|}^{j+j'} \sum_{m''=-j''}^{+j''} (-1)^{j-m} c(j', m'; j, -m) \left[\langle j | j' \rangle\right]_{m''}^{j''}$$

[5]roughly we flip the bras and kets in the outer product to obtain an inner product

where the $[\langle j|j'\rangle]_{m''}^{j''}$ obey equations (4.2) and (4.4). However, since the inner product is invariant under rotations (i.e. $\hat{D}^\dagger(\omega) = \hat{D}^{-1}(\omega)$) it should transform as an object of type $k = 0$ so that

$$[\langle j|j'\rangle]_{m''}^{j''} \propto \delta_{j''0}\delta_{m''0}$$

giving us

$$\langle j,m|j',m'\rangle = (-1)^{j-m}c(j',m';j,-m|0,0)\,[\langle j|j'\rangle]_0^0 = \frac{\delta_{j'j}\delta_{m'm}}{\sqrt{2j+1}}\,[\langle j|j'\rangle]_0^0$$

where we make use of the identity

$$c(j',m';j,-m|0,0) = \delta_{j'j}\delta_{m'm}(-1)^{j'-m'}/\sqrt{2j'+1}$$

The result tells us that

- the inner product of two angular momentum eigenstates is zero unless they are of identical symmetry, and that

- the inner product is independent of the magnetic quantum number m.

4.2.1.5 Wigner-Eckhart Theorem

Combining the results from sections 4.2.1.3 and 4.2.1.4 we arrive immediately at the famous Wigner-Eckhart theorem[53] which states that, given two angular momentum multiplets $|j,m\rangle, |j',m'\rangle$ and a spherical tensor t_q^k, the inner product $\langle j',m'|t_q^k|j,m\rangle$ takes on the specialized form

$$\langle j',m'|t_q^k|j,m\rangle = c(j,m;k,q|j',m')\langle j'||t^k||j\rangle \tag{4.19}$$

Where m, q, and m' range over all their possible values, and $\langle j'||t^k||j\rangle$ is a proportionality constant (i.e. independent of m, q, and m') termed the *reduced matrix element*.

4.2.1.6 Wigner 9j- and 6j-Symbols

To complete the discussion of addition of angular momentum we briefly introduce the *Wigner 9j-* and *6j-symbols*, which serve as shorthand for certain sums over products of Clebsch-Gordan coefficients. They appear in construction of matrix elements where

angular momenta are being "coupled" (i.e. added) and then "recoupled" to objects (bras, kets, operators) which may themselves be contain coupled angular momenta.

Take for instance the complicated reduced matrix element

$$\langle c; a, b|| \left[t^{a'} \tilde{t}^{b'} \right]^{c'} ||c''; a'', b'' \rangle \tag{4.20}$$

that would appear in the application of the Wigner-Eckhart theorem (equation (4.19)) to the inner products

$$\langle c, m_c; a, b| \left[t^{a'} \tilde{t}^{b'} \right]^{c'}_{m_{c'}} |c'', m_{c''}; a', b' \rangle \tag{4.21}$$

where the multiplets $|c, m_c; a, b\rangle, |c'', m_{c''}; a'', b''\rangle$ and spherical tensor $\left[t^{a'} \tilde{t}^{b'} \right]^{c'}_{m_{c'}}$ are each formed by coupling the angular momentum vectors $\vec{J}_a$ and $\vec{J}_b$. By decoupling and recoupling the angular momentum eigenstates and spherical tensors we can "separate" the angular momenta $\vec{J}_a$ and $\vec{J}_b$ to find that

$$\langle c; a, b|| \left[t^{a'} \tilde{t}^{b'} \right]^{c'} ||c''; a'', b'' \rangle =$$

$$(-1)^{a''-a'-a+b''-b'-b-(c''-c'-c)} [a, b, c', c'']^{1/2} \begin{Bmatrix} a & a'' & a' \\ b & b'' & b' \\ c & c'' & c' \end{Bmatrix} \langle a||t^{a'}||a''\rangle \langle b||\tilde{t}^{b'}||b''\rangle \tag{4.22}$$

where

$$[x, y, \ldots, z] \equiv (2x+1)(2y+1) \cdots (2z+1)$$

and the $\begin{Bmatrix} a & a'' & a' \\ b & b'' & b' \\ c & c'' & c' \end{Bmatrix}$ are the aforementioned Wigner 9j-symbols. The symbols have the property, one among many[54], that they vanish unless all the rows and columns satisfy property $CG.1$.

The Wigner 6j-symbol $\begin{Bmatrix} a & b & c \\ d & e & f \end{Bmatrix}$ serves as shorthand for the case where one of the entries in a 9j-symbol is zero:

$$\begin{Bmatrix} a & b & c \\ 0 & d & d \\ a & f & e \end{Bmatrix} = \frac{(-1)^{a+b+d+e}}{[a, d]^{1/2}} \begin{Bmatrix} a & b & c \\ d & e & f \end{Bmatrix} \tag{4.23}$$

4.3 Density Operator

In this section we introduce the *density operator*, an object closely associated with the quantum states ψ of a system. As discussed in this section and the following one, the density operator serves two main purposes for us:

- It aids in the statistical analysis of *ensembles* of molecules, whose angular momenta might assume a *distribution* of initial directions.

- The density operator allows an intuitive and mathematically powerful description of an ensemble's distribution of angular momentum in terms of its *multipole expansion*.

In our experiments we perform measurements on an ensemble of molecules that assume a classical distribution of initial quantum states. For simplicity we assume our possible initial states form a discrete set, so that we can describe our ensembles by specificying a pair $(\{|\psi_o\rangle\}, P(|\psi_o\rangle))$ which defines the set of possible initial states $\{|\psi_o\rangle\}$ and the fraction $P(|\psi_o\rangle)$ of molecules in the ensemble initially occupying a given state $|\psi_o\rangle$. At a later time t an initial state $|\psi_o\rangle$ will have evolved to the state $e^{H(t-t_o)/i\hbar}|\psi_o\rangle \equiv U(t,t_o)|\psi_o\rangle \equiv |\psi,t\rangle$, where H is the hamiltonian, we which presume to be identical for each molecule in the ensemble.

If at time t we measure some observable A of each molecule, then we expect on average a result equal to the *classical* expectation value $\langle\langle A\rangle\rangle$ over the distribution $P(|\psi_o\rangle)$ of the *quantum* expectation value $\langle A\rangle(t) = \langle\psi,t|A|\psi,t\rangle$, i.e.

$$\langle\langle A\rangle\rangle(t) = \sum_{\{|\psi_o\rangle\}} P(|\psi_o\rangle)\langle A\rangle(t)$$

From an orthonormal basis $\{|n\rangle\}$ we can construct and insert the identity $\sum_n |n\rangle\langle n|$ to obtain the following alternative expression for $\langle\langle A\rangle\rangle$

$$\begin{aligned}
\langle\langle A\rangle\rangle(t) &= \sum_{\{|\psi_o\rangle\}} P(|\psi_o\rangle)\langle\psi,t| \sum_n |n\rangle\langle n|A|\psi,t\rangle \\
&= \sum_n \langle n|A\left(\sum_{\{|\psi_o\rangle\}} P(|\psi_o\rangle)|\psi,t\rangle\langle\psi,t|\right)|n\rangle \\
&= \mathrm{Tr}\left(A\rho(t)\right)
\end{aligned} \qquad (4.24)$$

Where

$$\rho(t) \equiv \sum_{\{|\psi_o\rangle\}} P(|\psi_o\rangle)|\psi, t\rangle\langle\psi, t|$$

$$= U(t, t_o)\left(\sum_{\{|\psi_o\rangle\}} P(|\psi_o\rangle)|\psi_o\rangle\langle\psi_o|\right)U^\dagger(t, t_o) \qquad (4.25)$$

$$\equiv U(t, t_o)\rho_o U^\dagger(t, t_o)$$

is the *density operator* at a time t of an ensemble with a distribution $P(|\psi_o\rangle)$ at a time t_o.

To calculate any observable A associated with an ensemble (defined at a time t_o) at some later time t it is therefore sufficient to compute the ensemble's initial density operator $\rho(t_o) \equiv \rho_o$ and "propagate" the operator forward in time (i.e. $\rho_o \to \rho' = \rho(t)$) using equation (4.25).

Note that equation (4.25) also implies that two ensembles $(\{|\psi_o\rangle\}, P(|\psi_o\rangle))$ and $(\{|\psi_o\rangle\}', P'(|\psi_o\rangle))$ that have the same associated initial density operators $\rho_o \equiv \rho'_o$ are equivalent in that for all times they produce identical measurable predictions.

One can show that a density operator ρ at any time

- is hermitian

- has non-negative eigenvalues and

- has unit trace.

The converse is also true – for any hermitean operator ρ with non-negative eigenvalues and unit trace we can find an ensemble $(\{|\psi_o\rangle\}, P(|\psi_o\rangle))$ so that $\sum_{\{|\psi_o\rangle\}} P(|\psi_o\rangle)|\psi_o\rangle\langle\psi_o| = \rho$. Therefore the study of ensembles of quantum mechanical states is reduced to the study of operators ρ with the three above-mentioned properties evolving in time according to equation (4.25).

4.4 Multipole Expansion

4.4.1 State Multipoles

For a homonuclear diatomic molecule under no external forces, a given energy level (say the nth) is spanned by $2j_n + 1$ states, all with the same total angular momen-

tum quantum number j_n but different magnetic quantum numbers $m = -j_n, -j_n + 1, \ldots, j_n - 1, j_n$.

A general basis for ρ can be constructed from all possible outer products $|j_n, m\rangle\langle j_{n'}, m'|$, i.e. for any ρ there are coefficients $\rho_{nm,n'm'}$ such that

$$\rho = \sum_{n,n'} \sum_{m=-j_n}^{+j_n} \sum_{m'=-j_{n'}}^{+j_{n'}} \rho_{nm,n'm'} |j_n, m\rangle\langle j_{n'}, m'|$$

At all stages of our experiment, however, we can neglect the possibility of *coherences*, i.e. any nonzero amplitudes $\rho_{nm,n'm'}$ for $n \neq n'$. [6]

Our ensemble before and after each stage can be represented as a sum $\sum_n \rho_n$ of angular momentum *density multiplets*, where[7]

$$\rho_n = \sum_{m,m'=-j_n}^{+j_n} |j_n, m\rangle\langle j_n, m'| \tag{4.26}$$

Instead of expanding ρ in the $|m\rangle\langle m'|$ outer product basis as we've done in equation (4.26), it is often more useful to expand ρ_o in its spherical tensor basis (section 4.2.1.1), i.e. in terms of operators T_q^k defined according to

$$T_q^k \equiv \sum_{m,m'=-j}^{+j} (-1)^{j-m'} c(j, m; j, -m'|k, q)|m\rangle\langle m'| \tag{4.27}$$

(c.f. equation (4.9)). These spherical tensors, forming a basis for some density operator multiplet, are termed *state multipoles* (or just *multipoles* for short).

The coefficients ρ_q^k of ρ expanded in the T_q^k basis are known as the *multipole moments* and are expressed in terms of the $\rho_{mm'}$ by

$$\rho_q^k = \sum_{m,m'=-j}^{+j} (-1)^{j-m'} c(j, m; j, -m'|k, q)\rho_{mm'} \tag{4.28}$$

The coefficients are not all independent. The hermiticity of the density multiplet imposes the following constraint:

$$\rho_{-q}^k = (-1)^q \rho_q^{k*} \tag{4.29}$$

---

[6]The justification for this neglect for each stage are discussed in section A.

[7]For the remainder of the section we will take ρ to be some particular multiplet ρ_n, i.e. for compactness we suppress the (fixed) n and j indices as necessary.

4.4.2 Multipoles Under Coordinate Transformations

Next we consider the transformation of the state multipoles and associated moments under a change of coordinates. Consider a density multiplet ρ associated with an angular momentum multiplet $|j, m\rangle$, itself with an associated angular momentum vector $\vec{J}$. As discussed, we can associate with the multiplet some mulitpoles T_q^k and moments ρ_q^k. If we transform $\vec{J} \to \vec{J}'$ via some rotation ω, then ρ is also a density multiplet for the angular momentum multiplet $|j, m\rangle' \equiv \mathcal{D}(\omega)|j, m\rangle$ (see end of section 4.2.1.1) since the mulitplets span the same space. The associated multipoles T'^k_q and moments ρ'^k_q however will differ from their unrotated counterparts T_q^k and ρ_q^k. As spherical tensors the two sets of multipoles are related via equation (4.15) so that

$$T'^k_q = \sum_{q'=-k}^{+k} D^k_{q'q}(\omega) T_q^k \tag{4.30}$$

and the moments are likewise related via

$$\rho'^k_q = \sum_{q'=-k}^{+k} D^k_{q'q}(\omega)^* \rho^k_{q'} \tag{4.31}$$

4.4.3 Cartesian Multipoles

In discussing the transformation of density multiplets induced by surface scattering it will be helpful to expand our density multiplets in a basis slightly modified from the state multipoles we have been discussing throughout this section.

This modified basis will be composed of operators denoted by $T_q^{k\pm}$ and are termed "cartesian multipoles". They are defined in terms of the state multipoles T_q^k by the following formulas:

$$T_q^{k+} \equiv \left(T_{-q}^k + (-1)^q T_{+q}^k \right) \cdot \begin{cases} \frac{1}{2} & q = 0 \\ \frac{1}{\sqrt{2}} & q \neq 0 \end{cases} \tag{4.32}$$

and

$$T_q^{k-} \equiv i \left(T_{-q}^k - (-1)^q T_{+q}^k \right) \begin{cases} \frac{1}{2} & q = 0 \\ \frac{1}{\sqrt{2}} & q \neq 0 \end{cases} \tag{4.33}$$

where $q = 0, 1, \ldots, k$. Note that $T_0^{k-} = 0$ vanishes for all k and thus does not constitute a basis operator.

The corresponding moments are given by:

$$\rho_q^{k+} = (-1)^q \mathrm{Re}\left(\rho_q^k\right) \begin{cases} 1 & q = 0 \\ \sqrt{2} & q \neq 0 \end{cases} \tag{4.34}$$

and

$$\rho_q^{k-} = -(-1)^q \mathrm{Im}\left(\rho_q^k\right) \begin{cases} 1 & q = 0 \\ \sqrt{2} & q \neq 0 \end{cases} \tag{4.35}$$

The cartesian multipoles are to state multipoles what the real spherical harmonics (e.g. $\frac{x}{r}, \frac{y}{r}, \frac{z}{r}$ for $l = 1$) are to the (complex) spherical harmonics (e.g. $\sin\theta e^{+i\phi}$, $\sin\theta e^{-i\phi}$, $\cos\theta$ for $l = 1$), in that both have the virtue of transforming into themselves under the reflections $x \to -x$ and $y \to -y$.

4.4.4 Bond Angle Probability Distribution

As an example, suppose, as is the case for our system, that the angular momentum eigenstates $|jm\rangle$ are spherical harmonics $Y_j^m(\theta, \phi)$, so that a molecule in a state $|j, m\rangle$ has a probability $|Y_j^m(\theta, \phi)|^2 d\Omega$ of having its bond measured to lie in an infinitessimal patch of solid angle $d\Omega$ about the spherical coordinates θ, ϕ. In this case the ensemble expectation value of the projection $|\theta, \phi\rangle\langle\theta, \phi|$, i.e. $\mathrm{Tr}\left(|\theta, \phi\rangle\langle\theta, \phi|\rho\right) = \langle\theta, \phi|\rho|\theta, \phi\rangle \equiv P(\theta, \phi)$ represents the ensemble's *bond angle probability distribution*, and can be written in terms of the multipole moments as

$$P(\theta, \phi) = \frac{(-1)^j(2j+1)}{\sqrt{4\pi}} \sum_{k=0}^{2j} \frac{c\left(j, 0; j, 0|k, 0\right)}{\sqrt{2k+1}} \sum_{q=-k}^{+k} \rho_q^k Y_k^q(\theta, \phi) \tag{4.36}$$

so that ρ_q^k is a direct measure of the weight of the $(k, q)^{\mathrm{th}}$ term in the multipole expansion of the ensemble's bond angle probability distribution. In terms of the cartesian moments $\rho_q^{k\pm}$ we have

$$\begin{aligned} P(\theta, \phi) =& \frac{(-1)^j(2j+1)}{\sqrt{4\pi}} \sum_{k=0}^{2j} \frac{c\left(j, 0; j, 0|k, 0\right)}{\sqrt{2k+1}} \sum_{q=0}^{+k} (2 - \delta_{q0}) \mathrm{Re}\left(\rho_q^k Y_k^q(\theta, \phi)\right) \\ =& \frac{(-1)^j(2j+1)}{\sqrt{4\pi}} \sum_{k=0}^{2j} \frac{c\left(j, 0; j, 0|k, 0\right)}{\sqrt{2k+1}} \\ & \cdot \sum_{q=0}^{+k} \sqrt{2 - \delta_{q0}}(-1)^q Y_k^q(\theta, 0) \left(\rho_q^{k+}\cos m\phi + \rho_q^{k-}\sin m\phi\right) \end{aligned} \tag{4.37}$$

71

Isotropic
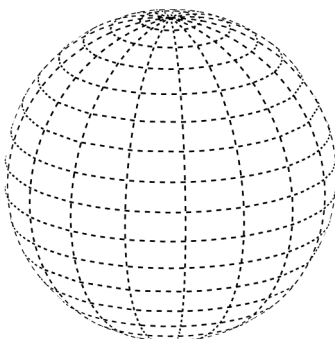
(a) $P(\theta, \phi) \propto 1$

Helicoptering
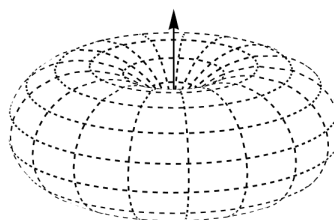
(b) $P(\theta, \phi) \propto \sin^2 \theta$. The arrow lies perpendicular to the surface.

Cartwheeling
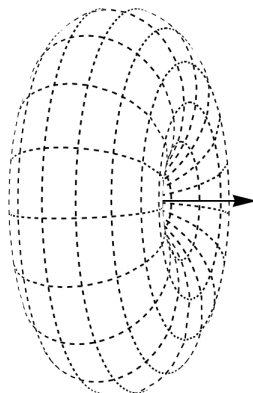
(c) $P(\theta, \phi) \propto 1 - \sin^2 \theta \cos^2 \phi$. The arrow lies parallel to the surface.

Figure 4.1: Bond angle probability distribution plots. The distance of the surface from the origin at some direction θ, ϕ is proportional to the probability $P(\theta, \phi)$ of measuring the molecule's bond to lie in that direction, where θ is angle made between the bond and the surface normal.

Consider for illustration a few example bond angle probability distributions and their associated density operators. Refer to figure 4.1. A totally uniform (i.e. isotropic) distribution of bond angles (figure 4.1a) is proportional to $Y_0^0(\theta, \phi)$, so that the associated density operator will contain only a monopole (i.e. T_0^0) term in its multipole expansion so that $\rho_q^k \propto \delta_{k0}\delta_{q0}$.

Take next the non-trivial bond-axis probability distribution $P(\theta, \phi) \propto \sin^2 \theta$ (figure 4.1b). If we assign z-axis (i.e. $\theta = 0$) to be the surface normal, such an ensemble would then represent helicoptering molecules, with their bonds lying primarily parallel to the surface. This bond-axis distribution can be expanded in spherical harmonics as $P(\theta, \phi) \propto Y_0^0(\theta, \phi) - \frac{1}{\sqrt{5}}Y_0^2(\theta, \phi)$, which according to equation (4.36) means that the density operator contains, in addition to some monopole ρ_0^0 term, a positive *quadrupole alignment parameter* ρ_0^2.

Finally, imagine we gradually rotate this ensemble about some axis lying on the surface, so that as the angle moves from $0° \rightarrow 90°$ we convert our helicoptering molecules into cartwheels (figure 4.1c). Using equation (4.14) we find that the quadrupole moment term $\rho_0'^2$ of the rotated ensembles varies with the rotation angle α as $\frac{1}{2}\left(3\cos^2 \alpha - 1\right)$, so that the full cartwheels also have a non-trivial quadrupole alignment parameter $\rho_0'^2 = -\frac{1}{2}\rho_0^2$ that is opposite in sign from the helicoptering molecules (i.e. negative).

The above examples use multipoles of order $k = 2$ and lower. In general we can further narrow the bond angle distribution by superimposing higher order multipoles, though for any given multiplet of angular momentum j we are limited to multipoles of order $k = 2j$ and lower. This limitation is yet another manifestation of the Heisenberg uncertainty principle, this time imposing a lower limit on the product of the spread in angular momenta Δj and the spread in bond angles $\Delta \theta$.

4.5 Two Photon Operator

In the absence of any external fields, an ensemble of molecules will tend to distribute themselves so that each multiplet ρ_n is rotationally symmetric, i.e. proportional to monopole T_0^0. This is a consequence of the underlying rotational symmetry of the field free Hamiltonian, which gives rise to degeneracy among the different m sublevels in a multiplet, which in turn results in identical Boltzmann factors $e^{-E_{j,m}/kT}$.

In order to obtain our desired alignment of incident molecules it is thus necessary to break the rotational symmetry of the system's Hamiltonian. We accomplish this by exciting the molecules with laser radiation. The symmetry is broken by the *polarization* of the laser, so that different directions in space are distinguished by the angle they make with the polarization vector, which is linear (i.e. no ellipticity) for all cases in our experiment.

Note: *In discussing the effect of laser radiation on the molecular ensemble (i.e. the density operator ρ) we will offer only rough explanations regarding the exchange of energy between molecules and the laser radiation (i.e. the laser-molecule dynamics) and instead focus on how they exchange angular momentum (i.e. their kinematics).*

We begin by selecting our quantization axis to be parallel with the laser polarization. In this case the effect of the absorption or stimulated emission of a laser photon, to first order in the laser's electric field strength, is characterized by a spherical tensor d_0^1 called the *one-photon* operator, so that the laser pulse sends a state $|\psi\rangle \rightarrow |\psi\rangle' = d_0^1|\psi\rangle$.

However, if the energies of the laser photons are out of resonance with every transition out of the initially populated states (i.e. with every *accessible* transitions) then the effect of the one-photon operator on the ensemble will be negligible. We are then led to consider second-order effects which we identify with the simultaneous absorption/stimulated emission of two photons. These effects become considerable when the sums and difference of the laser photon energies resonate with an accessible transition. We associate with such processes the *two-photon operator* d_0^2, which can be written as a special product of two one-photon operators:

$$d_0^2 = d_0^1 a_0^0 d_0^1 \tag{4.38}$$

where a_0^0 is a rotationally symmetric operator representing the intermediate states visited in the two-photon process.

The notation d_0^2 does not appear to be justified since from section 4.2.1.2 we might expect the product in equation (4.38) to decompose into spherical tensors of not only type $k = 2$ but type $k = 0$ as well[8]. Indeed for transitions between multiplets of equal j quantum numbers (i.e. Q-branch transitions) this is in general true. However for all the other branches ($\Delta j = \pm 1, \pm 2$) the $k = 0$ component of the two-photon-operator necessarily vanishes.

---

[8] $k = 1$ is excluded since $c(1, 0; 1, 0; 1, 0) = 0$.

To see this, we note that, since we presume two-photon process to be resonant with only one accessible transition, it should act only to send states from some initially occupied (i.e. *ground-state*) multiplet $|j, m\rangle$ to some other presumably unoccupied (i.e. *excited*) $|\tilde{j}, \tilde{m}\rangle$ and vice versa. In other words the two-photon operator can be expressed in terms of outer products $|j, m\rangle\langle\tilde{j}, \tilde{m}|$ and $|\tilde{j}, \tilde{m}\rangle\langle j, m|$. From section 4.2.1.1 it then follows that only terms with $k = |\tilde{j} - j|, \ldots, \tilde{j} + j$ can appear in the its spherical tensor decomposition. Since by assumption $|\tilde{j} - j| \neq 0$ we find that the two-photon operator d_0^2 cannot contain a $k = 0$ component and so must therefore be a pure $k = 2, q = 0$ spherical tensor.

As d_0^2 describes the action of the laser on the states of our system, the corresponding action on the density operator ρ is given by

$$\rho \to \tilde{\rho} = d_0^2 \rho d_0^2 \qquad (4.39)$$

(c.f. equation (4.25)). We can assume for simplicity that ρ for simplicity contains only terms from the ground state multiplet since any other intially occupied multiplets are annihilated by d_0^2. To determine the multipole moments $\tilde{\rho}_{\tilde{q}}^{\tilde{k}}$ of the excited multiplet following laser excitation we take the inner product of ρ with the $\tilde{k}, \tilde{q}$ state multipole (equation (4.27)) of the excited multiplet (denoted $\tilde{T}_{\tilde{q}}^{\tilde{k}}$), where the inner product is meant in the sense of equation (4.13), i.e.

$$\tilde{\rho}_{\tilde{q}}^{\tilde{k}} = \text{Tr}\left(\tilde{T}_{\tilde{q}}^{\tilde{k}\dagger} \tilde{\rho}\right) \qquad (4.40)$$

Expanding ρ in terms of (ground state) state multipoles (denoted T_q^k), we find then that the excited moments $\tilde{\rho}_{\tilde{q}}^{\tilde{k}}$ can be expressed as a weighted sum of the ground state moments ρ_q^k with weighting factors $s_{\tilde{q},q}^{\tilde{k},k}$, i.e.

$$\tilde{\rho}_{\tilde{q}}^{\tilde{k}} = \sum_{k=0}^{2j} \sum_{q=-k}^{+k} s_{\tilde{q},q}^{\tilde{k},k} \rho_q^k$$

where

$$s_{\tilde{q},q}^{\tilde{k},k} \equiv \text{Tr}\left(\tilde{T}_{\tilde{q}}^{\tilde{k}\dagger} d_0^2 T_q^k d_0^2\right) \qquad (4.41)$$

It turns out, somewhat remarkably, that the $s_{\tilde{q},q}^{\tilde{k},k}$ are, within a constant multiplicative factor, completely independent of the underlying hamiltonian and are expressible in terms of only Clebsch-Gordan coefficients and Wigner 9j-Symbols.

75

To see this we first recall that operators are themselves vectors[9], and that further from any operator a we can define two (commuting) super-operators[9] a_l and a_r, in general distinct, where a_l acts on the ket components of an operator (i.e. left multiplication $b \to ab$), and a_r acts on the bra component (i.e. right multiplication $b \to ba$). We then observe that d_0^2 is (the $q = 0$ component of) a spherical tensor with respect to both the angular momentum vector $\vec{J}$ associated with the kets $|j, m\rangle, |\tilde{j}, \tilde{m}\rangle$ as well as the angular momentum vector $-\vec{J}$ associated with the bras $\langle j, m|, \langle \tilde{j}, \tilde{m}|$. The action of simultaneous left and right multiplication by d_0^2, i.e. $b \to d_0^2 b d_0^2$ then defines a super-operator, which we denote by $d_0^2 \times d_0^2$, produced by the product of two spherical tensors. In section 4.2.1.2 we found that such products admit a spherical tensor decomposition via (4.17) so that

$$
\begin{aligned}
d_0^2 \times d_0^2 &= \sum_{K=0}^{4} \sum_{Q=-K}^{+K} c(2,0;2,0|K,Q) \left[d^2 \times d^2 \right]_Q^K \\
&= \sum_{K=0,2,4} c(2,0;2,0|K,0) \left[d^2 \times d^2 \right]_0^K
\end{aligned}
\tag{4.42}
$$

where the $\left[d^2 \times d^2 \right]_Q^K$ are spherical tensor super-operators. In the second line we eliminate the sum over Q in light of $CG.2$ and restrict the sum over K to even values in light of the identity

$$
c(j_1, m_1; j_2, m_2|j_3, m_3) = (-1)^{j_1+j_2-j_3} c(j_1, -m_1; j_2, -m_2|j_3, -m_3) \tag{4.43}
$$

Inserting equation (4.42) into (4.41) gives

$$
\begin{aligned}
s_{\tilde{q},q}^{\tilde{k},k} &= \sum_{K=0,2,4} c(2,0;2,0|K,0) \mathrm{Tr} \left(\tilde{T}_{\tilde{q}}^{\tilde{k}\dagger} \left[d^2 \times d^2 \right]_0^K T_q^k \right) \\
&\equiv \sum_{K=0,2,4} c(2,0;2,0|K,0) \langle \tilde{T}_{\tilde{q}}^{\tilde{k}} | \left[d^2 \times d^2 \right]_0^K | T_q^k \rangle
\end{aligned}
\tag{4.44}
$$

where in the last step we convert the trace to an inner product in the sense of equation (4.13) in order to bring our expression into form where the Wigner-Eckhart theorem (equation (4.19) readily applies, giving

$$
s_{\tilde{q},q}^{\tilde{k},k} = \sum_{K=0,2,4} c(2,0;2,0|K,0) c(k,q;K,0|\tilde{k},\tilde{q}) \langle \tilde{T}^{\tilde{k}} || \left[d^2 \times d^2 \right]^K ||T^k\rangle \tag{4.45}
$$

[9]c.f. section 4.2.1.1

76

From here we augment the notation $|T^k\rangle \rightarrow |T^k; j, j\rangle$ (and likewise $|\tilde{T}^{\tilde{k}}\rangle \rightarrow |\tilde{T}^{\tilde{k}}; \tilde{j}, \tilde{j}\rangle$) to highlight the coupled nature of the state multipoles. With this modification the reduced matrix element in equation (4.45) becomes

$$\langle \tilde{T}^{\tilde{k}}; \tilde{j}, \tilde{j} || \left[d^2 \times d^2 \right]^K ||T^k; j, j\rangle \tag{4.46}$$

which is identical in form to the LHS of (4.22). Substituting in the corresponding RHS we arrive at the fully reduced form of the $\tilde{\rho}_{\tilde{q}}^{\tilde{k}}$:

$$\tilde{\rho}_{\tilde{q}}^{\tilde{k}} = \sum_{k=0}^{2j} \rho_{\tilde{q}}^k \sum_{K=0,2,4} c(2,0;2,0|K,0) c(k,\tilde{q}; K,0|\tilde{k}, \tilde{q})$$

$$[k, K]^{1/2} (2\tilde{j}+1)(-1)^{K+\tilde{k}-k} \begin{Bmatrix} j & 2 & \tilde{j} \\ j & 2 & \tilde{j} \\ k & K & \tilde{k} \end{Bmatrix} \left| \langle \tilde{j} || d^2 || j \rangle \right|^2 \tag{4.47}$$

where the q sum has been eliminated in light of property CG.2, and the phase factor simplifies from our restriction to $O-$ and $S-$ branch transitions so that $\tilde{j} - j$ is even. We find then that, as claimed, the only system-dependent parameter (the reduced matrix element $\langle j' || d^2 || j \rangle$) enters as an overall scaling factor.

For O- or S-branch ($\Delta j \equiv \tilde{j} - j = \pm 2$) excitation of a rotationally symmetric ground-state density operator ($\rho_q^k \propto \delta_{k0}\delta_{q0}$), the $\tilde{\rho}_{\tilde{q}}^{\tilde{k}}$ have the following simplified form:

$$\tilde{\rho}_{\tilde{q}}^{\tilde{k}} \propto \delta_{\tilde{q}0} c(2,0;2,0|\tilde{k},0) \begin{Bmatrix} \tilde{j} & j & 2 \\ 2 & \tilde{k} & \tilde{j} \end{Bmatrix} \tag{4.48}$$

The main simplification here arises from application of equation (4.23).

For an arbitrary ground-state density operator ρ the O- or S-branch excited monopole moment $\tilde{\rho}_0^0$ takes a similarly simplified form:

$$\tilde{\rho}_0^0 \propto \sum_{k=0}^{2j} \rho_0^k c(2,0;2,0|k,0) \begin{Bmatrix} \tilde{j} & j & 2 \\ k & 2 & j \end{Bmatrix} \tag{4.49}$$

Note here that for equations (4.48) and (4.49) we see again from (4.43) that only even $\tilde{k}$ and k moments, respectively, enter in.

Equations (4.48) and (4.49) are quite similar in appearance. In fact we can state that the relative strength of the excited state moments produced from the $j_1 \rightarrow j_2$ excitation from a symmetric ground state are equal to the relative weights of

contributions of different ground state moments to the population of the excited state excited in the opposite transition $j_2 \to j_1$. This can be understood by interpreting the second transition as the time-reversed version of the first.

<center>❊ ❊ ❊</center>

Incidentally, equation (4.48) applied to S-branch ($\tilde{j} - j = +2$) and equation (4.49) applied to O-branch ($\tilde{j} - j$ = -2) both possess alternative derivations that are similar in character. The derivations are simpler than the above and apply directly to our probing and pumping stages (respectively). We conclude the section with their description.

Consider the excited-state moments $\tilde{\rho}_{\tilde{q}}^{\tilde{k}}$ produced by two-photon S-branch excitation from a rotationally symmetric ground-state $\rho \propto T_0^0$. The only multipoles $\tilde{T}_{\tilde{q}}^{\tilde{k}}$ that can be produced by action of the two-photon *super-operator* $d_0^2 \times d_0^2$ on such a ρ are those with $\tilde{k} = 0, 2, 4$ and $\tilde{q} = 0$ so that

$$\tilde{\rho} = \sum_{\tilde{k}=\{0,2,4\}} \tilde{\rho}_0^{\tilde{k}} \tilde{T}_{\tilde{q}}^{\tilde{k}}$$

and thus the population $p_{\tilde{m}}$ in the $|\tilde{j}, \tilde{m}\rangle$ angular momentum eigenstate is (equation (4.27))

$$
\begin{aligned}
p_{\tilde{m}} &= \langle \tilde{j}, \tilde{m} | \tilde{\rho} | \tilde{j}, \tilde{m} \rangle \\
&= \sum_{\tilde{k}=0,2,4} \tilde{\rho}_0^{\tilde{k}} \langle \tilde{j}, \tilde{m} | \tilde{T}_{\tilde{q}}^{\tilde{k}} | \tilde{j}, \tilde{m} \rangle \\
&= \sum_{\tilde{k}=0,2,4} \tilde{\rho}_0^{\tilde{k}} (-1)^{\tilde{j}-\tilde{m}} c(\tilde{j}, \tilde{m}; \tilde{j}, -\tilde{m} | \tilde{k} 0)
\end{aligned}
$$

We next note that, since the laser polarization is linear and presumed parallel to the quantization axis, the action of the two-photon *operator* on an angular momentum eigenstate $|j, m\rangle$ preserves the m quantum number, i.e. $|j, m\rangle \to |\tilde{j}, m\rangle$ (again CG.2). There is therefore no way to achieve population of the $|\tilde{j}, \tilde{m}\rangle$ angular momentum eigenstates with $|\tilde{m}| > j$. Since we are considering an S-branch transition this means

$$p_{\tilde{m}} = 0, \ \tilde{m} = \pm \left(\tilde{j} - 1\right), \pm\tilde{j} \tag{4.50}$$

<center>78</center>

This defines a system of two linear equations (the $+\tilde{m}$ and $-\tilde{m}$ constraints are equivalent) with three unknowns ($\tilde{\rho}_0^{\tilde{k}}, \ k = 0, 2, 4$), so that the moments $\tilde{\rho}_0^{\tilde{k}}, \ k = 0, 2, 4$ are thus determined up to a multiplicative constant.

Next we consider the $\tilde{\rho}_0^0$ monopole moment produced from an O branch transition, which must by identical reasoning be expressible as a weighted sum over the $k = 0, 2, 4, \ q = 0$ ground-state moments:

$$\tilde{\rho}_0^0 = \sum_{k=0,2,4} a_k \rho_0^k$$

By expanding the ρ_0^k via equation (4.28) in terms of the ground-state probabilities p_m we get

$$\tilde{\rho}_0^0 = \sum_{k=0,2,4} a_k \sum_{m=-j}^{+j} (-1)^{j-m} c(j,m;j,-m|k,0) p_m$$

We next observe that the LHS can not depend on the p_m with $|m| > \tilde{j}$ since we can not excite their associated angular momentum eigenstates. For O-branch transitions we therefore require

$$\frac{d}{dp_m} \tilde{\rho}_0^0 = 0, \ m = \pm(j-1), \pm j$$

yielding

$$\sum_{k=0,2,4} a_k (-1)^{j-m} c(j,m;j,-m|k,0) = 0, \ m = \pm(j-1), \pm j \qquad (4.51)$$

which allows for determination of the a_k within a multiplicative factor.

As expected, the form of equations (4.50) and (4.51) are identical, as one simply the time reversal of the other.

4.6   Alignment Preparation

The H_2 molecules in the SMB are *unaligned*, so that any multiplet is represented by a density operator containing only a monopole term, i.e. $\rho_o \propto T_0^0$. As mentioned earlier, this is not true for every diatomic molecule. O_2, N_2, and I_2, for instance, will all acquire a non-trivial alignment during the supersonic expansion[55], [56]. In any event, we verify the non-alignment of our incident H_2 molecules using our alignment detection technique, described in section 4.7.

Alignment for our experiment is accomplished by transferring molecules via a two-photon Raman process from some initially populated ground state multiplet $|j_o, m_o\rangle$

to another initially unpopulated excited multiplet $|j, m\rangle$. The alignment produced from the excitation process arises from the structure of the ground- and excited-state multiplets as well as the angular momentum of the laser radiation.

In the following we give a quantitative description of the excited state multipole moments produced in the limits of weak and strong laser intensity.

4.6.1   Weak Pumping

If the laser radiation is weak then we only need to consider the lowest order resonant process, which for our scheme is a simultaneous absorption and emission of a high and low energy photon, respectively. Intuitively in the weak limit molecules are so rarely excited that we can certainly neglect the possibility that any excited molecules are subsequently stimulated *back* into the ground state.

In this case the modification of the density matrix due to the pump laser is given by the action of the two-photon operator described in the previous section. Since all multiplets are by assumption initially unaligned, the moments ρ_q^k in the excited state produced by the two-photon process are given by equation (4.48), i.e.

$$\gamma \rho_q^k \propto \delta_{q0} c(2, 0; 2, 0|k, 0) \begin{Bmatrix} j & j_o & 2 \\ 2 & k & j \end{Bmatrix}$$

$$\equiv \delta_{q0} p_k$$

The left-superscript γ here indicates the moments $\gamma \rho_q^k$ are referenced to the coordinate system with the $\hat{z}$ axis (i.e. the quantization axis) parallel to the pump laser. Since the $q \neq 0$ moments vanish this holds for any selection of $\hat{x}$ and $\hat{y}$ axes.

We will be interested in the moments ρ_q^k in a particular coordinate system, which we will term the *lab frame*, where

- the $\hat{z}$ axis is parallel to the surface normal, and

- the $\hat{y}$ axis is perpendicular to both the surface normal and gravity [10]

A diagram illustrating the lab-frame geometry is shown in figure 4.2. Equation (4.31) can be applied to determine the lab frame moments ρ_q^k from the polarization frame

---

[10] This direction will turn out to be parallel to the direction of propagation for both the pump and probe lasers. It will be helpful for later discussion to consider the more general case of non-fixed laser propagation directions.

(a) dimers straight   (b) dimers diagonal
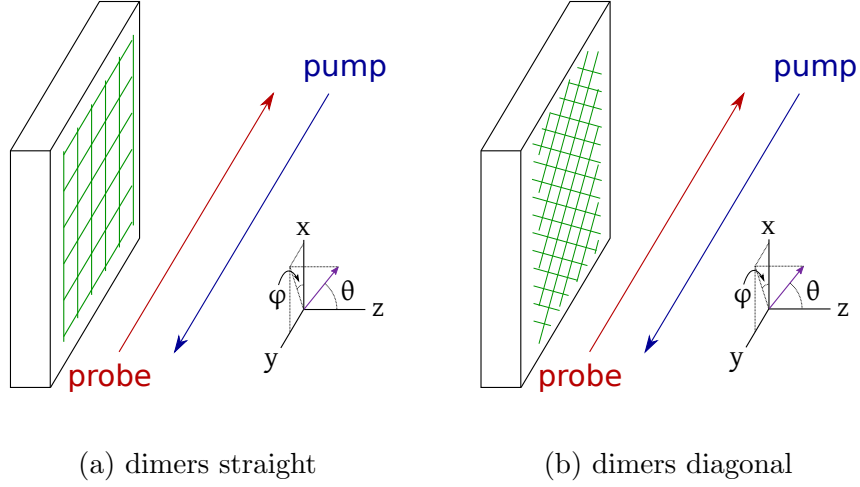
Figure 4.2: Diagrams illustrating lab-frame geometry. $\hat{z}$ axis is parallel to surface normal, while $\hat{y}$ axis is parallel to laser propagation direction which is fixed for all measurements for both the pump and probe lasers. The quantization axis for the polarization frame is shown in purple. Note that lab-frame axes are independent of the orientation of the dimer rows, illustrated schematically in green.

moments $^{\gamma}\rho_q^k$. If we suppose that the pump polarization in the lab frame has polar and azimuthal angles θ and ϕ respectively, the lab frame can be made to coincide with the polarization frame by a compound rotation ω consisting of

- a rotation about the lab frame $\hat{y}$ axis by an angle θ, followed by

- a rotation about the lab frame $\hat{z}$ axis by an angle ϕ.

From (4.31) then we have

$$^{\gamma}\rho_q^k = \sum_{q'=-k}^{+k} D_{q'q}^{k}{}^{*}(\omega)\rho_{q'}^k$$

81

or, by the unitarity of the $D_{q'q}^k$

$$
\begin{aligned}
\rho_q^k(\theta, \phi) &= \sum_{q'=-k}^{+k} D_{qq'}^k(\omega)^\gamma \rho_{q'}^k \\
&= \sum_{q'=-k}^{+k} D_{qq'}^k(\omega) \delta_{q'0} p_k \\
&= D_{q0}^k(\omega) p_k \\
&\propto \frac{Y_k^{q*}(\theta, \phi)}{\sqrt{2k+1}} p_k
\end{aligned}
\tag{4.52}
$$

where in the last step we use the well known identity of the Wigner D-matrices. The moments $\rho_q^{k\pm}$ for the cartesian multipoles (section 4.4.3) are determined from equations (4.34) and (4.35) and yield

$$
\rho_q^{k\pm}(\theta, \phi) = (-1)^q \sqrt{\frac{2 - \delta_{q0}}{2k+1}} p_k \begin{pmatrix} +\mathrm{Re} \\ -\mathrm{Im} \end{pmatrix} \left(Y_q^k(\theta, \phi) \right)
$$

We are interested in two special orientations of the pump polarization

- The *cartwheeling* orientation: $\theta = 0, \phi = 0$

- The *helicoptering* orientation: $\theta = \frac{\pi}{2}, \phi = 0$

The moments $^c\rho_q^k$ for the cartwheels coincide with the polarization frame moments and thus vanish unless $q = 0$ in which case we get:

$$
^c\rho_0^{k+} = {}^c\rho_0^k = {}^\gamma\rho_0^k = p_k
$$

while the moments $^h\rho_q^{k\pm}$ for the helicopters vanish for the negative parity cartesian multipoles T_q^{k-} and for the T_q^{k+} yield

$$
^h\rho_q^{k+} = (-1)^q \sqrt{\frac{2 - \delta_{q0}}{2k+1}} p_k Y_k^q(\frac{\pi}{2}, 0)
$$

4.6.1.1   Strong Pumping

In this section we investigate the limit of strong pumping, where we can assume the photon flux is so intense that any molecule that *can* interact with the laser executes a large number of cycles of

- absorption into the excited state followed by

- stimulated emission back into the ground state.

The exact number of cycles a given molecule executes will be subject to some uncertainty due to intensity variations within the spatial profile of an indiviual pulse as well as variations in overall pulse energy from shot-to-shot. The result is that any molecule that interacts with the laser will have a roughly 50% probability of being excited, for the same reason that a car tire's valve at the end of a long trip is just as likely to be pointing up as pointing down, independent of its starting orientation.

In our case the transitions induced by the laser satisfy a $\Delta m = 0$ selection rule, where the multiplets $|j, m\rangle_\gamma$ are referenced to quantization axis parallel to the pump polarization. If we consider an S-branch $(j_o \to j = j_o + 2)$ pumping transition, then all $2j_o + 1$ of the ground state eigenstates $|j_o, m_o\rangle_\gamma$ have an excited state $|j, m_o\rangle_\gamma$ to transition into. Since all the eigenstates in the ground multiplet are equally populated, we find for the excited state density multiplet ϱ:[11]

$$\varrho \propto \sum_{m=-j_o}^{+j_o} |j, m\rangle_\gamma \langle j, m|_\gamma$$

The above equation can be cast in terms of the moments $^\gamma\varrho_q^k$, yielding

$$\begin{aligned}
^\gamma\varrho_q^k &= \delta_{q0} \sum_{m=-j+2}^{j-2} (-1)^{j-m} c(j, m; j, -m|k, 0) \\
&\equiv \delta_{q0} \mathcal{P}_k
\end{aligned} \tag{4.53}$$

Repeating the analysis in the previous section we find the cartwheeling moments vanish unless $q = 0$ in which case we find

$$^c\varrho_0^{k+} = {}^c\varrho_0^k = \mathcal{P}_k$$

and similarly for the helicopters

$$^h\varrho_0^{k+} = (-1)^q \sqrt{\frac{2 - \delta_{q0}}{2k+1}} \mathcal{P}_k Y_k^q(\frac{\pi}{2}, 0)$$

---

[11] To avoid confusion with the weak pumping case, we denote the strong pumping density multiplet and associated moments with the variable ϱ.

S1 pumped moments

k,q	0,0	2,0	2,2	4,0	4,2	4,4
weak cartwheel ${}^c\rho_q^{k+}$	1	$-\frac{4\sqrt{3}}{7}$		$\frac{\sqrt{22}}{7}$		
weak helicopter ${}^h\rho_q^{k+}$	1	$\frac{2\sqrt{3}}{7}$	$-\frac{6}{7}$	$\frac{3\sqrt{\frac{11}{2}}}{28}$	$-\frac{\sqrt{\frac{55}{2}}}{14}$	$\frac{\sqrt{\frac{55}{14}}}{4}$
strong cartwheel ${}^c\varrho_q^{k+}$	1	$-\frac{5}{3\sqrt{3}}$		$\frac{4\sqrt{\frac{2}{11}}}{3}$		
strong helicopter ${}^h\varrho_q^{k+}$	1	$\frac{5}{6\sqrt{3}}$	$-\frac{5}{6}$	$\frac{1}{\sqrt{22}}$	$-\frac{\sqrt{\frac{10}{11}}}{3}$	$\frac{\sqrt{\frac{35}{22}}}{3}$

k,q	6,0	6,2	6,4	6,6
strong cartwheel ${}^c\varrho_q^{k+}$	$\frac{5}{3\sqrt{33}}$			
strong helicopter ${}^h\varrho_q^{k+}$	$-\frac{25}{48\sqrt{33}}$	$\frac{5\sqrt{\frac{35}{22}}}{48}$	$-\frac{5\sqrt{\frac{7}{33}}}{16}$	$\frac{5\sqrt{\frac{7}{2}}}{48}$

Table 4.1: Non-vanishing moments of the $S1$ pumped molecules for different polarization orientations and pumping strengths.

The non-vanishing excited state moments ρ_q^{k+} produced by an S1 ($j_o = 1 \rightarrow j = 3$) pumping transition for both orientations (cartwheeling and helicoptering) and pumping strengths (weak and strong) are listed in table 4.1 and plotted in figure 4.3. In addition, plots of the S1-excited bond angle probability distributions (section 4.4.4) for both pumping strengths are shown in figure 4.4.

4.7 Alignment Detection

In the probe stage of our experiment pulses of UV laser radiation are focused onto the scattered molecules. The wavelength of the radiation is selected to resonate with a two-photon O branch transition taking molecules from a $j = 3$ ground electronic state multiplet to a $j = 1$ multiplet in an excited electronic state. Any molecules transferred to the excited state are presumed to be ionized by the same laser pulse and collected
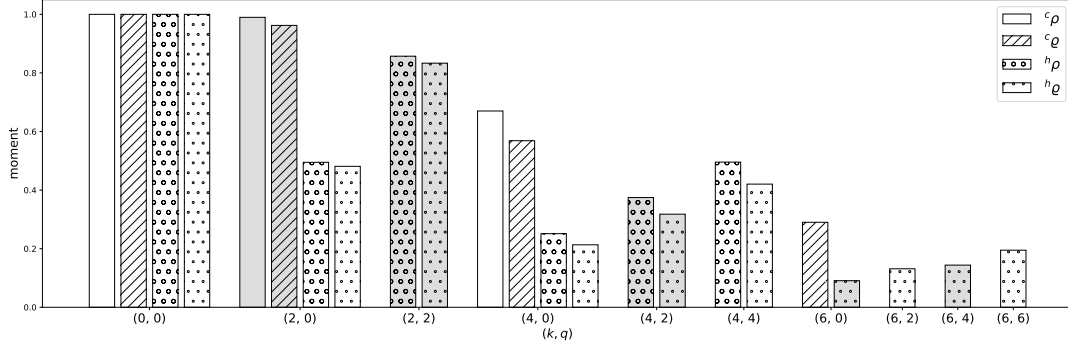
Figure 4.3: Plot of alignment moments produced from $S1$ pumping for different polarization orientations and pumping strengths. Positive and negative moments are filled in with white and gray, respectively.

by the charged particle detector. The measured signal S is thus proportional to the population in the excited state multiplet, which is in turn proportional to the multiplet's monopole moment $\tilde{\rho}_0^0$. Applying equation (4.49) we can find S in terms of the ground state multipole moments $^\gamma\rho_q^k$, i.e.

$$S \propto \tilde{\rho}_0^0 \propto \sum_{k=0}^{2j} {}^\gamma\rho_0^k c(2,0;2,0|k,0) \begin{Bmatrix} \tilde{j} & j & 2 \\ k & 2 & j \end{Bmatrix} \equiv \sum_{k=0}^{2j} s_k {}^\gamma\rho_0^k \qquad (4.54)$$

where, similar to section 4.6, the moments $^\gamma\rho_q^k$ are referenced to a quantization axis parallel to the probe laser polarization (i.e. the polarization frame). Again since we only consider the $q = 0$ moments the above equation holds for any selection of $\hat{x}$ and $\hat{y}$ polarization frame axes.

To obtain an expression for S in terms of the lab frame moments ρ_q^k, we first suppose, like we did for the pumping analysis, that the probe laser polarization has a polar angle θ and azimuthal angle ϕ in the lab frame. Then the polarization frame can be brought to coincide with the lab frame via a sequential rotation ω composed of

- a rotation by an angle θ about the $\hat{y}$ axis, followed by

- a rotation by an angle ϕ about the $\hat{z}$ axis.

For such a rotation we have

$$D_{q0}^{k\,*}(\omega) = \sqrt{\frac{4\pi}{2k+1}} Y_k^q(\theta, \phi)$$

85

(a) weak pumping   (b) strong pumping
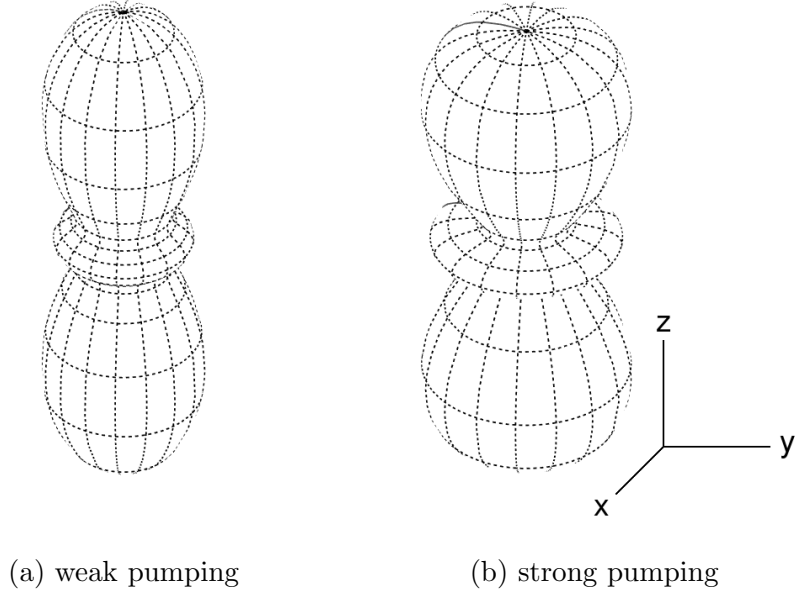
Figure 4.4: Bond angle probability distributions of $S1$ pumped multiplets for the cartwheeling molecules. The helicoptering distributions are obtained by rotating the cartwheeling distribution by $90°$ about the $\hat{y}$ axis.

From equation (4.31) then we find

$$^{\gamma}\rho_0^k = \sqrt{\frac{4\pi}{2k+1}} Y_k^q(\theta, \phi) \rho_q^k$$

After substituting in the transformed moments into equation (4.54), we then group terms by $|q|$ and apply the hermiticity condition (4.29) along with the identity $(Y_l^m)^* = (-1)^m Y_l^{-m}$ to find

$$S(\theta, \phi) \propto \sum_{k=0}^{2j} \tilde{s}_k \sum_{q=0}^{k} (2 - \delta_{q0}) \operatorname{Re}\left(Y_k^q(\theta, \phi)\rho_q^k\right)$$

where $\tilde{s}_k \equiv \frac{s_k}{\sqrt{2k+1}}$.

In terms of the cartesian multipoles defined in section 4.4.3

$$S(\theta, \phi) \propto \sum_{k=0}^{2j} \tilde{s}_k \sum_{q=0}^{k} \sqrt{2 - \delta_{q0}}(-1)^q Y_k^q(\theta, 0) \left(\rho_q^{k+} \cos q\phi + \rho_q^{k-} \sin q\phi\right) \qquad (4.55)$$

Comparing the above equation with equation (4.37) for the bond angle probability distribution (equation (4.37)) we find a superficial similarity, so that perhaps we would

86

be in some sense justified in interpreting the signal obtained at some polarization as a measure of the probability of finding a molecule with its bond parallel to that polarization. The k-dependent weights, however, differ for the two formulas[12] so that the equivalence only holds multipole-by-multipole (i.e. between varying q at fixed k).

Though equation (4.55) is valid for any probe polarization, in practice our laser propagation direction is along the $\hat{y}$-axis so that we are working at fixed $\phi = 0$. In this case (4.55) simplies to

$$
\begin{aligned}
S(\theta) &\propto \sum_{k=0}^{2j} \tilde{s}_k \sum_{q=0}^{k} \sqrt{2 - \delta_{q0}}(-1)^q Y_k^q(\theta, 0)\rho_q^{k+} \\
&= \sum_{k=0}^{2j} \tilde{s}_k \sum_{q=0}^{k} (2 - \delta_{q0})(-1)^q \left(\sum_{k'=0}^{k} y_{k'k}^q P_{k'}(\cos\theta) \right) \rho_q^{k+} \qquad (4.56) \\
&= \sum_{k'=0}^{2j} \left(\sum_{k=0}^{2j} \sum_{q=0}^{k} \left(\tilde{s}_k \sqrt{2 - \delta_{q0}}(-1)^q y_{k'k}^q \rho_q^{k+} \right) \right) P_{k'}(\cos\theta)
\end{aligned}
$$

where in the second line we've expanded the $Y_k^q(\theta, 0)$ in an orthonormal basis of Legendre polynomials $P_{k'}(\cos\theta)$, i.e. $Y_k^q(\theta, 0) = \sum_{k'=0}^{2j} y_{k'k}^q P_{k'}(\cos\theta)$.

Finally we arrive at an expression for the weight $S_{k'k}^q$ of the contribution of the moment ρ_k^{q+} to the coefficient $S_{k'}$ (dubbed the "apparent moment") of the k'^{th} Legendre polynomial in the expansion of $S(\theta)$, i.e.:

$$
S_{k'k}^q \propto \tilde{s}_k \sqrt{2 - \delta_{q0}}(-1)^q y_{k'k}^q \qquad (4.57)
$$

so that

$$
S(\theta) = \sum_{k'=0,2,4} S_{k'} P_{k'}(\cos\theta) \qquad (4.58)
$$

where

$$
S_{k'} = \sum_{k=0,2,4} \sum_{q=0}^{k} S_{k'k}^q \rho_k^{q+} \qquad (4.59)
$$

If we assume the moments ρ_q^{k+} with odd q vanish, then we need only consider even values of k' since the associated $y_{k'k}^q$ of the odd k' would vanish by parity. The justification for the neglecting odd q moments for the incident and scattered molecules

---

[12] In fact the weights for $S(\theta, \phi)$ *vanish* for any $k \neq 0, 2, 4$, while the weights for the bond angle distribution $P(\theta, \phi)$ must be nonzero for all even k since the distribution fully encodes the alignment of the density multiplet.

derives from the details of the pumping process (section 4.6) and the symmetry of the surface (section 5.3), respectively.

The $S_{k'k}^q$ for the $O3$ transition ($j = 3, \tilde{j} = 1$) are listed in table 4.2 and plotted in figure 4.5. From the table it is clear that from a single scan $S(\theta)$ it is not possible to uniquely determine the moments ρ_q^k, i.e. the matrix $S_{k'k}^q$ is 3×6 and thus not invertible[13]. From equation (4.55) we can see that a knoweldge of the ϕ dependence of the ionization signal is necessary for a complete determination of the moments. Experimentally this would require varying the propagation direction of the probe laser which is not possible for our particular arrangement (as mentioned briefly earlier we have the laser propagation direction fixed parallel to $\hat{y}$).

Alternatively the ionization signal could be monitored as the molecular ensemble is rotated about the surface normal. For the incident molecules this is in principle possible but would require varying the direction of the pump laser which is, for the same reasons as the probe, beyond our experimental capabilities. For the scattered molecules this would require a simultaneous rotation of the surface as well as the incident ensemble about the surface normal. Though this is of course for us in general not possible for the same reason as the incident molecules, complimentary information about the scattering process can none-the-less be obtained by surface rotations alone. In some circumstances unique determination of the scattered moments is even possible, though only for some subset of the moments. The details of this procedure are more appropriately presented alongside a discussion of scattering and surface symmetry and so is reserved for section 5.1.

---

[13] Though in some instances a known symmetry of the ensemble permits a full determination of the moments. For example, the ensemble produced from a SMB for any molecule (not just H_2) will be cylindrically symmetric about the beam's direction so that, with the beam axis chosen as the quantization axis, only $q = 0$ moments occur. The $S_{q'q}^k$ matrix for any k is invertible when restricted to this subspace. This allows us to verify that non-alignment of the unpumped molecules.

$$S^q_{k'k},\ j=3,\ \tilde{j}=1$$

k,q k'	0,0	2,0	2,2	4,0	4,2	4,4
0	1		$-\frac{4}{7}$		$\frac{\sqrt{\frac{22}{5}}}{21}$	$\frac{\sqrt{\frac{22}{35}}}{3}$
2		$-\frac{4\sqrt{3}}{7}$	$\frac{4}{7}$		$\frac{\sqrt{110}}{21}$	$-\frac{2\sqrt{\frac{110}{7}}}{21}$
4				$\frac{\sqrt{22}}{7}$	$-\frac{2\sqrt{\frac{22}{5}}}{7}$	$\frac{\sqrt{\frac{22}{35}}}{7}$

Table 4.2: Elements of the matrix $S^q_{k'k}$ (equation 4.57) for the $O3$ transition. The elements have been rescaled to give $S^0_{00} = 1$ and blank cells indicate a vanishing element.
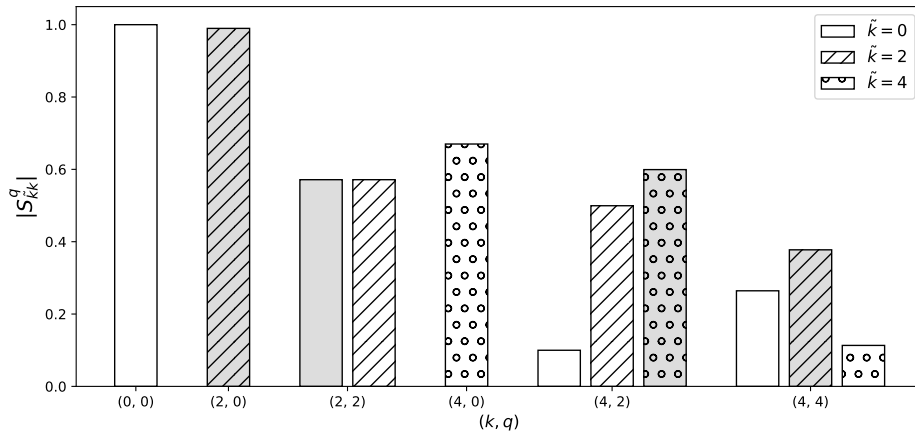
Figure 4.5: Plot of matrix elements S^q_{kk} for the $O3$ transition. Positive and negative values are filled in with white and gray, respectively.

Chapter Five: Scattering

In this chapter we develop the concepts that will aid us in the analysis of the rotational structure of scattered molecules.

The first portion (sections 5.1-5.4) of the chapter takes a look at the symmetry of our system and how the constraints arising from these symmetries allow us to extract more information from our measurements. Beginning in section 5.1 we characterize the symmetry of the surface, going on in section 5.2 to show how surface disorder effectively enlarges the symmetry group of the system (i.e. $C_{2v} \rightarrow C_{4v} \supset C_{2v}$). Then in section 5.3 we classify the symmetries of the multipoles, and then show in section 5.4 how the constraints arising from the system symmetry allow us to use our measurements to make a full determination of the moments created in the scattering of cylindrically symmetric incoming distributions. The analysis makes use of connections between the multiplets obtained by scattering off of

- surfaces whose terraces contain dimer rows running parallel to the lab-frame $\hat{x}$ and $\hat{y}$ axes,

- surfaces whose terraces contain dimer rows running at $45°$ to the lab-frame $\hat{x}$ and $\hat{y}$ axes.

In following we refer these as the *dimer-parallel* and *dimer-diagonal* cases, respectively (see figure 4.2 for an illustration).

In the second portion of the chapter we apply the model potential developed by Brenig and Pehlke (section 5.5) and derive a prediction for the scattered multiplets which can be compared to our results.

5.1   Symmetry of Si(100) Surface

The c(4x2) reconstruction of the Si(100) surface is shown in figure 5.1. In addition to the translation symmetry present on all crystalline surfaces the surface possesses a number of point (i.e. fixed-center) symmetry operations:

- O_π: Rotation by $180°$ about the surface normal.
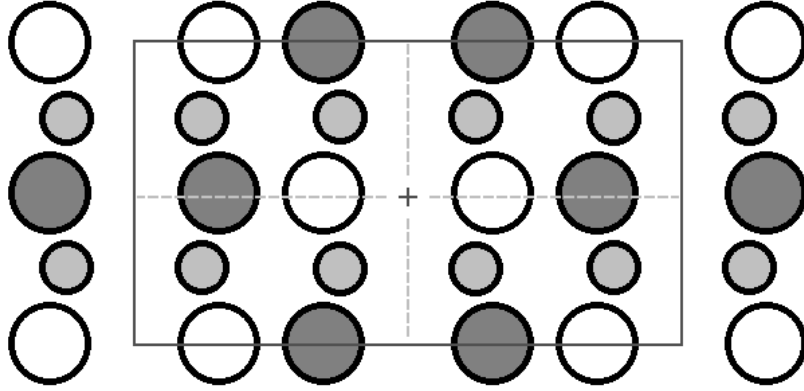
Figure 5.1: Top-view diagram of the Si(100) c(4x2) reconstruction. The surface normal points out of the page. The pairs of dark and light large circles represent the buckled dimers, and the small circles represent subsurface atoms bonded to the dimers. The rectangle represents the surface unit cell and the crosshair represents the origin of point group symmetry operations. The dashed lines denote the (011) and (01$\bar{1}$) directions and represent the two reflection planes, with the horizontal and vertical lines lying in the O_a and O_b reflection planes respectively.

- O_a: Reflection about the plane containing the surface normal and dimer bonds.

- O_b: Reflection about the plane containing the surface normal and the line running between the dimer rows.

Applying any of these operations on all the silicon nuclei simultaneously is equivalent to a permutation of the nuclei. This implies that we can apply any of these same operations to the coordinates of the scattering molecule without affecting the overall nuclei-nuclei Coulomb energy or ground-state electronic energy. Since any orthogonal transformation preserves the kinetic energy, the operators corresponding to these symmetry operations commute with the full hamiltonian H describing the molecular motion and thus also with the scattering operator S transforming the ingoing state $|\psi_o\rangle$ to the outgoing state $|\psi'\rangle$, i.e.

$$[O_\alpha, S] = 0$$

where $\alpha = \pi, x, y$ and

$$S \equiv \lim_{t_\pm \to \pm\infty} e^{\frac{H(t_+ - t_-)}{i\hbar}}$$

91

so that

$$|\psi_o\rangle \to |\psi'\rangle = S|\psi_o\rangle$$

5.2   Symmetry of the Scattering Super Operator

As discussed in section 4.3, a density operator ρ evolves according to the rule

$$\rho_o \to \rho' = S\rho_o S^\dagger$$

If we assume, however, that the terrace encountered by any given molecule has a dimer row orientation of (011) or $(01\bar{1})$) with equal probability, then the scattered density operator should be *averaged* over the orientiations in the following sense:

$$\rho' = \frac{1}{2}\left(S\rho_o S^\dagger + S'\rho_o S'^\dagger\right) \equiv \bar{S}\rho_o \tag{5.1}$$

where

$$S' = O_{\pi/2}SO^\dagger_{\pi/2}$$

where $O_{\pi/2}$ is a rotation by 90° about the surface normal, transforming dimer rows from the (011) orientation to the $(01\bar{1})$ orientation and vice versa.

At the end of equation (5.1) we define the super operator $\bar{S}$ taking $\rho_o \to \rho'$. Because of the equal-weighted averaging over dimer row orientations, $\bar{S}$ commutes with four additional symmetry operators, in addition to the operators O_π, O_a, and O_b defined earlier. These operators are:

- $O_{\pi/2}$: Rotation by 90° about the surface normal (just introduced).

- $O_{-\pi/2}$: Rotation by -90° about the surface normal.

- O_+: Reflection about the 45° diagonal.

- O_-: Reflection about the -45° diagonal.

The seven symmetry operators defined above, along with the trivial identity operator $O_e \equiv 1$, form a representation of the C_{4v} group. The invariance of the scattering super operator $\bar{S}$ implies a decomposition

$$\bar{S} = \sum_j \bar{S}_j \tag{5.2}$$

where the super operator $\bar{S}_j$ mixes operators of identical C_{4v} symmetry j.

$\diagdown\ q$ $k\ \diagdown$	0	1	2	3	4	5	6
0	$\mathbf{A_1}$						
1	A_2	E					
2	$\mathbf{A_1}$	E	$\mathbf{B_1}, B_2$				
3	A_2	E	B_2, B_1	E			
4	$\mathbf{A_1}$	E	$\mathbf{B_1}, B_2$	E	$\mathbf{A_1}, A_2$		
5	A_2	E	B_2, B_1	E	A_2, A_1	E	
6	A_1	E	B_1, B_2	E	A_1, A_2	E	B_1, B_2

Table 5.1: C_{4v} symmetries of cartesian multipoles for the dimer-parallel case. For $q = 0$ we have $T_q^{k-} = 0$ so only the + symmetry is listed. For the pairs A_1, A_2 and B_1, B_2 the first (second) symmetry of the pair corresponds to the symmetry of the + (-) multipole, respectively. The E symmetry is two-dimensional; that is, there is no basis for which the representation is diagonal. The symmetries with bold font correspond to multipoles that we can detect. For the dimer-diagonal case we exchange the B_1 and B_2 symmetries.

5.3 Symmetry of the In- and Out-going States

Consider next the subspaces V_{in} and V_{out} of in- and out-going operators

$$V_{\substack{\text{in} \\ \text{out}}} \equiv |\pm z; j_n, m\rangle\langle\pm z; j_n, m'|, \ m, m' = -j_n, \ldots, +j_n$$

where

- $+z$ and $-z$ denote the ingoing and outgoing momentum states, taken to be antiparallel and parallel to the surface normal for the ingoing and outgoing states respectively, and

- the set j_n, m with $m = -j, \ldots, +j$ comprises an angular momentum multiplet.

Since the surface normal is invariant to all the symmetry operations, and an angular momentum multiplet is invariant to *any* orthogonal transformation, these subspaces can be decomposed into a basis of operators of definite symmetry. These operators turn out to be the multiplet's cartesian multipoles $T_q^{k\pm}$ defined in section 4.4.3. For details about the symmetry classification of the multipoles the reader is referred to section B. The symmetry designations of the multipoles for the dimer-parallel case

are listed in table 5.1. The designations for the dimer-diagonal case are obtained from the dimer-parallel case by a simple modification described in the table caption.

5.4   Determination of Scattered Moments

The symmetry properties outlined in the previous section of the mulitpoles place constraints on the moments of the scattered multiplets.

The most important import constraint for our purposes concerns the scattering of cylindrically symmetric multiplets. By cylindrically symmetric we mean multiplets containing only $q = 0$ multipoles. Such examples would include the cartwheeling pumped multiplets or the trivial unaligned multiplet ($\propto T_0^0$). For such multiplets we find that T_4^{4+} is the only detectable $q \neq 0$ multipole that can be populated by surface scattering.

This can be seen by inspection of table 5.1, keeping in mind that the surface can only mix multipoles of identical C_{4v} symmetry (see equation (5.2)).

Further, the ρ_4^{4+} moments for the dimer-parallel and dimer-diagonal cases are related by negation, i.e. $\rho_4^{4+} \leftrightarrow -\rho_4^{4+}$. To see this we note that[1]

- the incoming ensemble contains only $q = 0$ multipoles which are invariant under $\pm 45°$ rotations, while

- $T_4^{4+} \rightarrow -T_4^{4+}$ under $\pm 45°$ rotations, combined with the fact that

- rotating the scattering super operator by $\pm 45°$ is the same as rotating the incoming and outgoing density operators by $\mp 45°$.

The above constraints imply that from measurements of the dimer-parallel and dimer-diagonal apparent moments[2] $\,^p S_{k'}$ and $\,^d S_{k'}$, respectively, the full scattered multiplet of cylindrically symmetric incident distributions can be determined. Explicitly, referring to equation 4.57 or table 4.2 we find that

$$\rho_0^{k+} = \frac{1}{2 S_{kk}^0} \left(\,^p S_k + \,^d S_k \right) \tag{5.3}$$

---

[1] see section B
[2] see equation (4.59)

for $k = 0, 2, 4$, and that

$$\rho_4^{4+} = \frac{1}{2S_{k'4}^4} \left({}^pS_{k'} - {}^dS_{k'} \right) \tag{5.4}$$

for $k' = 0, 2, 4$ so that in fact we have an over-determined system of equations for ρ_4^{4+}. The measured results for ρ_4^{4+} for the different k' serve as a consistency check. If the results agree then we may be confident that our assertions about the symmetry of the system are justified.

For the helicoptering molecules less can be said by symmetry considerations alone. It is interesting to note that in the dimer-parallel case we probe the B_1 component of the scattering super operator $\bar{S}$, while the dimer-diagonal case probes its B_2 component. The difference ${}^pS_{k'} - {}^dS_{k'}$ does not however allow us to compare the different components since the analysis will be complicated by a non negligible T_4^{4+} term.

5.4.1   The "Dimer-Half-Diagonal" Case

For completeness we mention here briefly that for the "dimer-half-diagonal" case where the dimer-rows run at $22.5° = \frac{\pi}{8}$ to the lab-frame $\hat{y}$ or $\hat{x}$ axes we find that the $T_4^{4\pm}$ multipoles exchange symmetries, i.e. $A_1 \leftrightarrow A_2$. In this case we expect the apparent moments ${}^{hd}S_{k'}$ for molecules scattered from a cylindrically symmetric incident distribution to contain contributions from only the $q \neq 0$ multipoles, implying

$$\rho_0^k = \frac{{}^{hd}S_{k'}}{2S_{kk}^0}$$

for $k = 0, 2, 4$. Including these equations along with the equations (5.3) from the dimer-parallel and dimer-diagonal measurements would then overdetermine of the system of equations for the $q = 0$ moments, and serve as a further consistency check.

5.5   The Brenig-Pehlke Potential

To provide context for the discussion of the results I include in this section calculations on the dynamics of hydrogen molecules scattering from the Si(100) surface. The molecule-surface interaction is described using a model potential developed by Wilhelm Brenig and Eckhard Pehlke[57]. The potential attempts to account for a number of experimental phenomena known at the time about the H_2/Si(100) system. These phenomena include:
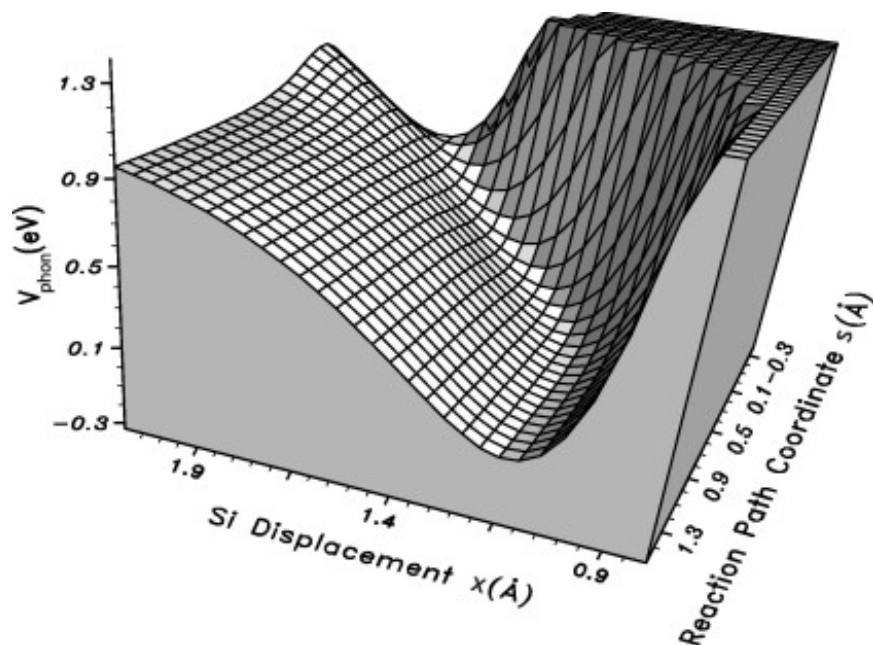
Figure 5.2: The molecule-lattice potential energy surface, from an earlier model by Brenig [58]. During a desorption event (increasing s), motion along the reaction (molecular-surface distance) coordinate s is converted to lattice vibrations x. Similarly, adsorption is strongly suppressed at low surface temperatures where displacements of the silicon atoms from their ≈ 1.2Å equilibrium positions are small.

- The *barrier puzzle*: adsorption measurements[59] of hydrogen molecules on clean Si(100) indicate large ($\sim .8$eV) adsorption barriers, in apparent disagreement with the low (.4eV) translational energies measured on desorption[60]. The Brenig-Pehlke potential attempts to account for the disagreement by allowing strong coupling of lattice and molecular motion at the transition state (see figure 5.2).

- Vibrational heating / vibrationally assisted sticking: H_2 molecules desorbing from Si(100) show a $\approx 25\times$ increase in vibrational excitation ($\nu = 1$) over that expected from a Boltzmann distribution at that surface temperature[61]. Likewise, adsorption is enhanced for molecular beams using higher temperature nozzles at equal kinetic energies[7]. This is presumably due to the higher fraction of vibrationally excited molecules at the higher nozzle temperatures. From the measurements investigators estimate a $\nu = 1$ adsorption barrier of .4eV, a reduction of .4eV from the .8eV barrier for $\nu = 0$ (compare this to the .52eV

required for vibrational excitation).

- Angular sticking dependence: Using wafers with large ($> 2°$) miscut angles, Si(100) surfaces can be prepared with dimer rows oriented in one predominant direction. Angle-resolved sticking measurements were performed using such samples and large anisotropies were observed[4], with sticking showing $\cos^3 \theta$ and $\cos^{12} \theta$ dependencies in the polar angle for the dimer-parallel and -perpendicular directions, respectively. Investigators trace this behavior to the strong directionality of the covalent bonding at the silicon surface.

- Rotational cooling: From the same desorption measurements exhibiting vibrational heating[61] investigators also find rotational state populations with effective temperatures $T_r \approx 345K$ roughly half that of the surface temperature $T_s \approx 780K$. The authors rationalize these findings by assuming an adiabatic evolution from highly frustrated rotation at the transition state to fully unhindered rotation in the gas phase. As the molecule desorbs energy in the frustrated motion is released into translational motion, resulting in cold rotational temperatures.

5.5.1 The Potential

The Brenig-Pehlke potential is a function of (a subset of) the nuclear coordinates only. The electrons are presumed to remain at all times in their collective ground state, and the corresponding ground state electronic energy contributes to the effective potential in which the nuclei move. In other words, the Born-Oppenheimer approximation is assumed to apply.

In contrast with full *ab initio* methods[28] whereby a potential energy function is constructed by interpolation of a large number of electronic structure (e.g. density functional theory) calculations, the Brenig-Pehlke potential is built around a model Hamiltonian with a small number of fitting parameters that are determined from a mixture of empirical data or density functional theory calculations.

The Hamiltonian is built from the following coordinates:

- s, the reaction coordinate. Qualitatively, as s increases (decreases) the molecule is making progress towards completing its desorption (adsorption) reaction. Large postive values of s correspond to large molecule-surface distances, while

negative values correspond to large H-H separation (i.e. bond breaking). There is a $\approx .25\text{Å}$ wide region near $s = .1\text{Å}$ where the coordinate transitions between the two limiting behaviors. The model potential is designed so that when all other coordinates vanish s follows the minimum energy path.

- v, the vibration coordinate. Mathematically this is simply the direction perpendicular to the reaction coordinate. When s is large and positive v corresponds to the bond length, and as s decreases v gradually evolves to represent the amplitude of symmetric (in-phase) vibration of the two H-Si bonds of the chemisorbed molecule.

- x, the substrate coordinate. This coordinate is intended to represent the lattice motion excited upon associative desorption of H_2. Though it requires in general many coordinates to describe the motion of surface atoms, theoretical evidence points towards the motion of dimer buckling/unbuckling as dominating participant.

- y_1 and y_2, the transverse coordinates. Corrugation in the potential in these corrugates gives rise to diffractive effects and determines the angular dependence of the sticking probability/desorption flux.

- θ and ϕ, the rotational coordinates. These are the usual spherical coordinates of the molecule bond angle, with the $\hat{z}$ axis referenced to the surface normal and the $\hat{x}$ and $\hat{y}$ axes referred to the directions parallel/perpendicular to the dimers. The variation in the potential with respect to these coordinates will be our main object of concern.

The potential couples all the coordinates together only indirectly via the reaction coordinate s. In detail:

$$V(x, \mathbf{y}, v, \theta, \phi; s) = V_t(s) + V_p(x; s) + V_v(v; s) + V_r(\theta, \phi; s) + V_c(\mathbf{y}; s)$$

For the precise form of all the different components of the potential we refer the reader to the original publication [57], but it will be worthwhile at this point to state explicitly the form of the rotational potential $V_r(\theta, \phi; s)$

$$V_r(\theta, \phi; s) = \frac{mr(s)^2}{2} \left(\omega_\theta^2(s) \cos^2 \theta + \omega_\phi^2(s) \sin^2 \theta \cos^2 \phi \right) \equiv V_\theta(s) \cos^2 \theta + V_\phi(s) \sin^2 \theta \cos^2 \phi$$

$$(5.5)$$
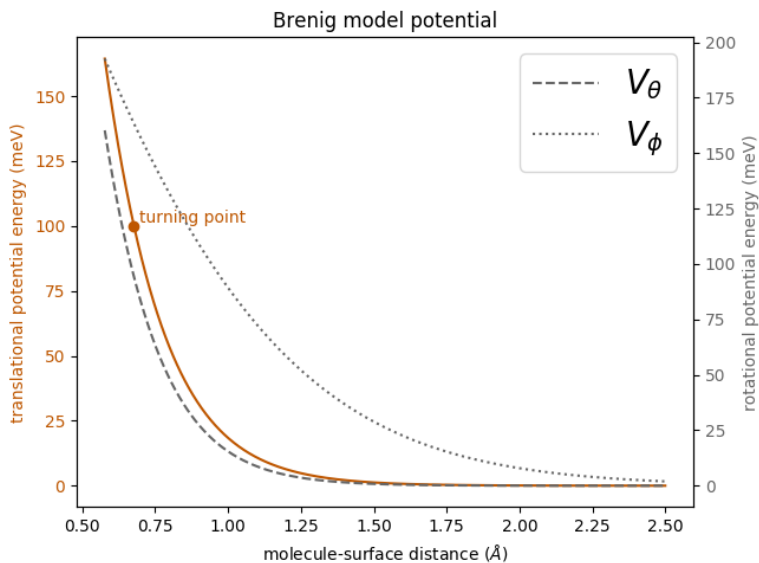
Figure 5.3: A plot of the s-dependence of the potentials $V_t(s)$ and $V_r(\theta, \phi; s)$ for the reaction coordinate s and rotational coordinates θ and ϕ, respectively. For the rotational potential V_r we have set $\theta = 0$ for the ϕ-independent component and $\theta = \pi/2$ and $\phi = 0$ for the ϕ-dependent component.

This potential, as expected, exhibits the full C_{2v} symmetry of the clean silicon surface (see section 5.1). The s-dependence of the different components of the potential is plotted in figure 5.3.

5.5.2 Dynamics Calculations

With the potential described above, along with the appropriate kinetic energy operator, a full scattering calculation could be in principle be performed to determine the scattered ensemble for a given incident ensemble. However, it is only very recently that 7D quantum dynamical calculations have even become computationally feasible[28], and, in light of the extreme simplicity of the model, it is doubtful that the necessary investment of labor and resources is justified.

With this in mind, we instead opt for very rough approximate approach to solving the scattering dyanmics, with the aim of obtaining a qualitative picture of surface-mediated realigment of our molecular ensemble. The general strategy is as follows:

1. Using the full Brenig-Pehlke Hamiltonian, determine a reasonable *classical* trajectory $s(t)$ for the reaction coordinate.

99

2. The time-evolution of the reaction coordinate then gives rise to an effective *time-dependent* potential on the other coordinates.

3. A scattering matrix relating the incoming and outgoing states is determined by solving the time dependent Schrödinger equation.

Descriptions and results of the classical trajectory and quantum mechanical scattering calculations are given separately in the following sections (5.5.2.1 and 5.5.2.2).

5.5.2.1 Classical Trajectory Calculations

To determine the classical trajectory $s(t)$ then we simply neglect all terms except for the translational potential $V_t(s)$. This choice was selected after a preliminary investigation of the magnitude of coupling between the various degrees of freedom at the incident energies used in our experiment. The main qualitative conclusion of the investigation was that the turning point occurs early enough along the reaction path that the potential energy has very little curvature, so that the motions along the different coordinates are largely independent. The quantitative results are illustrated in figure 5.4, where we have plotted the energy transfer between the phonon and vibrational coordinates as a function of beam energy (i.e. initial translational energy in the s-coordinate). The energy transfer is determined by a classical trajectory simulation[3] involving the reaction coordinate s and single transverse degree of freedom (i.e. molecular vibration v or phonon vibration x) initialized with and without quantum mechanical zero-point energy. From the plot it is clear that in all cases negligible energy is coupled out of the reaction coordinate. Coupling to the surface coordinates y_1 and y_2 can be neglected by appeal to a simple $\Delta p/\Delta t \sim \Delta V/\delta X$ argument which estimates energy transfers on the order of $\Delta E < 10^{-3}$meV. Looking again at figure 5.3, we find however that for our ≈ 100meV beam energies the corrugation in rotational potential $V_r(\theta, \phi, s)$ is comparable to the potential $V_t(s)$ along the minimum energy path. Using a $\Delta j/\Delta t \sim \Delta V/\Delta \phi$ argument similar to that applied for the surface coordinates, we might expect the molecule-surface interaction to facilitate a transfer of a full $\hbar$ unit of angular momentum to/from the rotational degrees of freedom. The implied energy transfer between the translational and rotational

---

[3] The simulations solve the appropriate Euler-Lagrange equations for the Brenig-Pehlke Hamiltonian using a Runge-Kutta method (RK4) with a time step of $.1/\omega_v^G$, where $\hbar\omega_v^G \approx 516$meV is the gas-phase H_2 vibrational quantum.
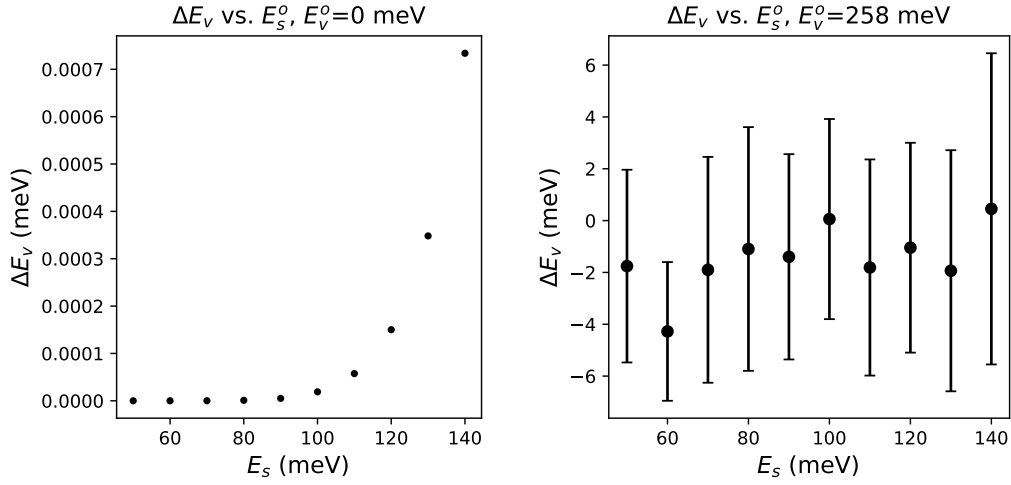
(a) vibrational coupling
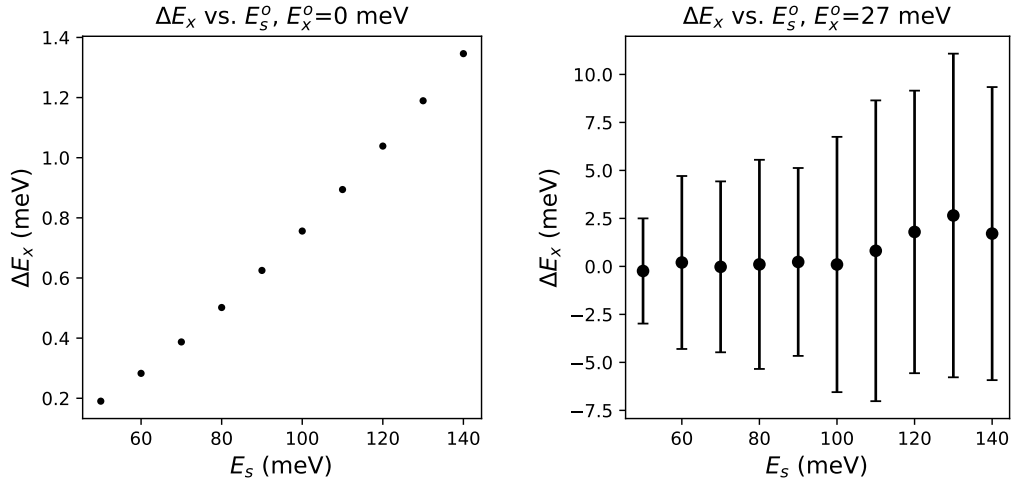
(b) phonon coupling

Figure 5.4: Classical coupling to **(a)** vibrational coordinate v and **(b)** phonon coordinate x as a function of the initial translational energy in the reaction coordinate s. The plots to the right contain zero point energy in the non-s coordinates and the error bars indicate the spread from a random sampling of $N = 10$ initial oscillation phases.

degrees of freedom would then be on the order of the incident beam translational energy. The Brenig-Pehlke potential in other words predicts strong coupling between the reaction coordinate and the rotational coordinates at our beam energies. Our approach fails to rigorously treat this correlation and this failure is perhaps most the

101

classical reaction coordinate trajectory
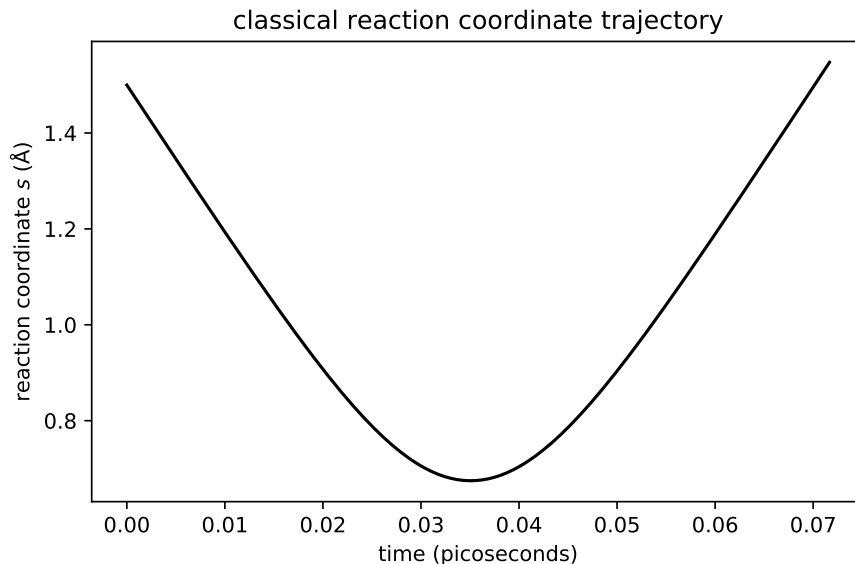
Figure 5.5: Classical trajectory for the reaction coordinate s at an incident energy of 100meV with other coordinates frozen at equilibrium geometries. Coupling to the rotational coordinates is activated for reaction coordinates $s \lesssim 1\text{Å}$ (see figure 5.3).

approach's greatest shortcoming. It is nevertheless plausible that despite this shortcoming the approach should allow for a rough picture of the *extent* of realignment (i.e. $|j, m\rangle \to |j, m'\rangle$, $m' \neq m$) incurred by scattering from the surface.

Having addressed the caveats, we present the trajectory $s(t)$ obtained by freezing all the non-reaction coordinates is shown in figure 5.5. This trajectory will be used to generate a time-dependent potential in which we can propagate a quantum mechanical ensemble of aligned molecules and obtain a prediction for the alignment of the scattered ensemble.

5.5.2.2 Quantum Mechanical Scattering Calculations

As mentioned earlier, upon substituting $s \to s(t)$ the Brenig-Pehlke potential is transformed from a time-*in*dependent seven-dimensional potential to a time-*de*pendent six-dimensional potential. Further, since the remaining degrees of freedom were all coupled indirectly via the reaction coordinate s, the potential now splits into a sum so that the rotational motion completely decouples from the other degrees of freedom[4].

---

[4] Schematically, if a Hamiltonian $H_A(t)$ scatters $|a\rangle \to |a'\rangle$ and a Hamiltonian $H_B(t)$ scatters $|b\rangle \to |b'\rangle$, then the combined Hamiltonian $H_A(t) + H_B(t)$ scatters $|a\rangle \otimes |b\rangle \to |a'\rangle \otimes |b'\rangle$. In other

To determine the effect of scattering on the rotational motion it is therefore sufficient to compute the time evolution of the incident rotational states $|j, m\rangle$ of interest under the influence of the rotational potential $V_r(\theta, \phi; s(t))$. This elimination of the non-rotational degrees of freedom massively reduces the complexity of the scattering problem, thus permitting a computationally inexpensive solution.

Since we are interested in rotationally inelastic scattering of the $j = 3$ multiplet of rotational states, they comprise our input basis. Following the suggestion in the Brenig-Pehlke publication [57] we allow for scattering into any of the $j = 0$ to $j = 7$ multiplets, though the resulting amplitudes in the $j = 3$ multiplet differ only superficially from those obtained by allowing only reorienting collisions, i.e. $|j, m\rangle \rightarrow |j', m'\rangle$, $j = j' = 3$.

The time-dependent Schrödinger equation is solved using an iterative/perturbative algorithm described in appendix C. We selected a time step of $.002/\omega \approx .01$fs where ω is the natural frequncy of a harmonic approximation to the repulsive barrier in the reaction coordinate. This choice of time step resulted, for all input states, in a sum of final state squared amplitudes that differed from unity by less than a part in a thousand. Smaller or larger times steps decreased or increased this difference in rough proportion. The results are shown in figure 5.6. For each in-state (i.e. for each $|j, m\rangle$ for fixed $j = 3$ and $m = -3, -2, \ldots, 2, 3$) the algorithm required roughly ten iterations to converge, indicating multiple reorienting collisions. This is supported by rough inspection of the scattering matrix, which, for instance, shows significant scattering from $m = -3 \rightarrow m' = +3$ despite the $\Delta m = -2, 0, +2$ selection rule enforced by the form of the perturbation.

Figure 5.7 shows the evolution of the $k = 2, q = 0$ multipole moment, i.e. the *quadrupole alignment parameter*, for three initial ensembles. Interestingly, the Brenig-Pehlke potential predicts in both the helicopter and cartwheeling cases a *reversal* of the quadrupole alignments, while predicting no induced alignment in an intially isotropic ensemble.

This same result is illustrated from a different perspective using bond-angle probability distributions, shown in figure 5.8. The elongated and narrow axes for both of the aligned ensembles shrink and grow respectively upon scattering, while the unaligned ensemble looks mostly unchanged.

words, if the two subsystems A and B begin uncorrelated they remain so.
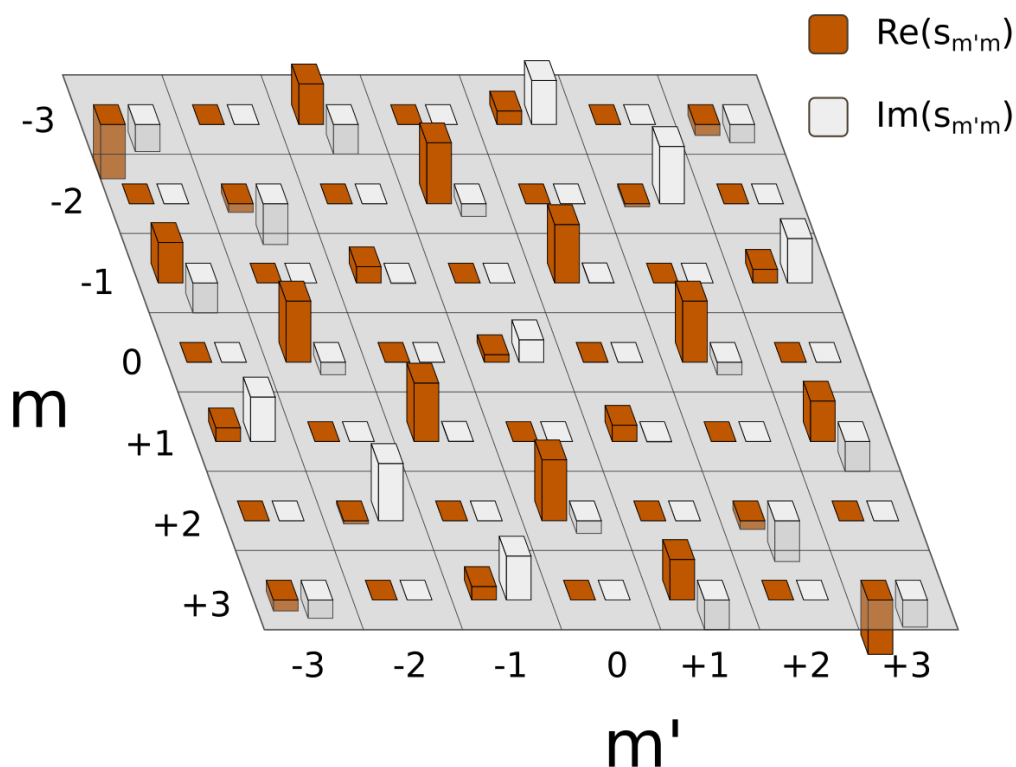
Figure 5.6: Scattering matrix $|j, m\rangle \rightarrow \sum_{m'=-j}^{+j} s_{m'm}|j, m'\rangle$ for the $j = 3$ multiplet. Bars with negative height (below the semi-transparent plane) indicate negative amplitude.

We can also look at how the individual multipole moments scatter. In figure 5.9 we have plotted the scattering matrix $s_{(k',q'),(k,q)}$ for the different cartesian multipoles with A_1 symmetry, i.e. totally symmetric with respect to the C_{4v} symmetry group. From the figure we can make a couple observations:

- unaligned molecules ($\rho \propto T_0^0$) remain unaligned, as we saw earlier in figures 5.7 and 5.8, while

- an incoming quadrupole moment is completely converted into purely $k = 4$ components upon scattering. Further,

- the $k = 4, q = 0$ (hexadecapole) moment obtains some quadrupolar character and, importantly,
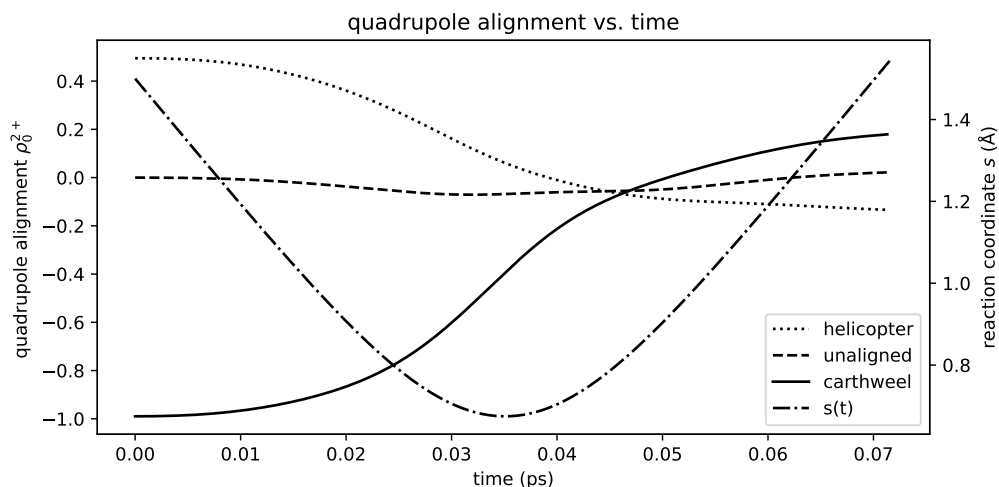
Figure 5.7: Time evolution of the quadrupole alignments for three initial ensemble alignments – unaligned, cartwheel, and helicopter. The reaction parameter $s(t)$ is also plotted to show that changes in alignment occur primarily at the classical turning point.

- both the cylindrically symmetric $k = 2$ and $k = 4$ moments "feel" the surface-parallel potential corrugation in that they generate signficant amplitude in the cylindrically assymetric $k = 4, q = 4$ moment.

As discussed at the end of section 4.7, a single ionization measurement $S(\theta)$ (equation (4.58)) can not disambiguate, for instance, a loss of quadrupole alignment from modulation of probability density in the azimuthal coordinate ϕ. In the same discussion it was found that for cylindrically symmetric incident ensembles the full scattered ensemble could be measured by taking ionization measurements at two different dimer-row orientations.

For the greatest effect the orientations should be those with the probe laser propagating at $0°$ and $45\circ$ to the dimer rows, i.e. the "dimer parallel" and "dimer diagonal" cases. The predicted ionization scans for the Brenig-Pehlke potential are shown in figure 5.10. The modulation shows qualitatively different behavior for the different dimer orientations, indicating signficant interplay between molecular rotation and the dimer-row reconstruction.

incident   scattered

cartwheels

incident   scattered

helicopters

incident   scattered

unaligned
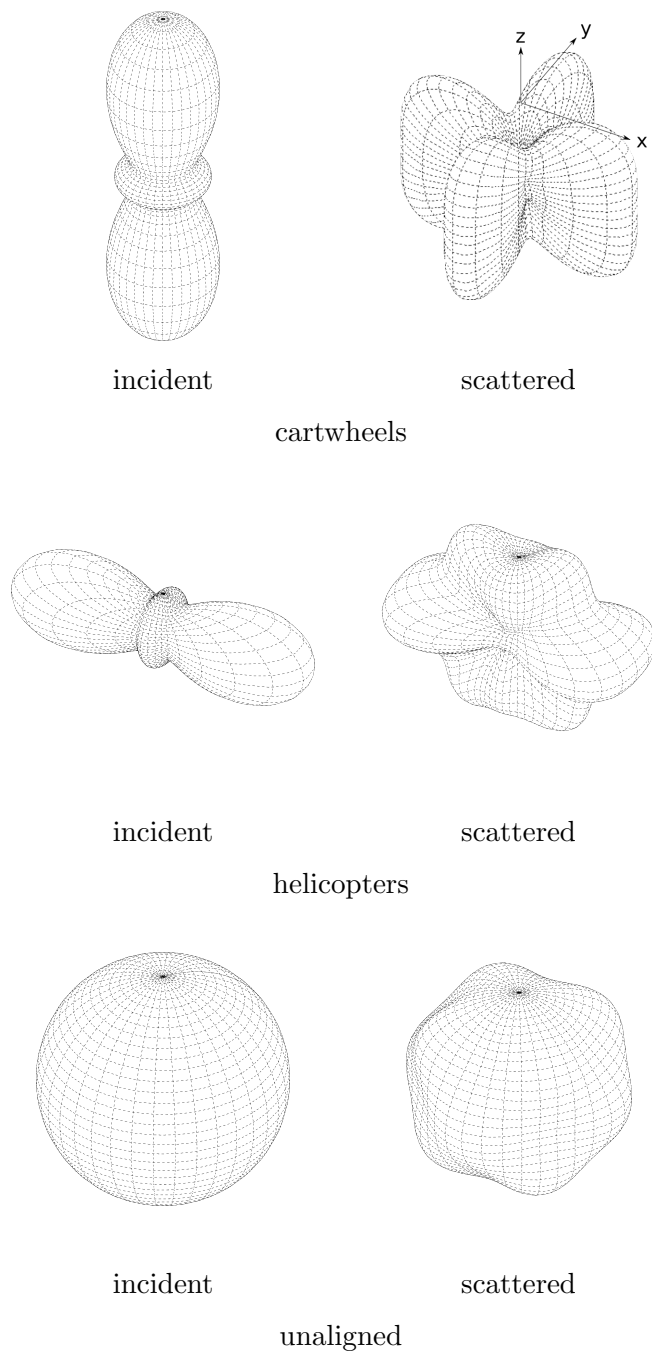
Figure 5.8: Incident and scattered bond angle probability distributions (see section 4.4.4) for three different incident ensembles. The lab frame coordinate axes (section 4.6) are superimposed on the scattered cartwheel distribution for reference.
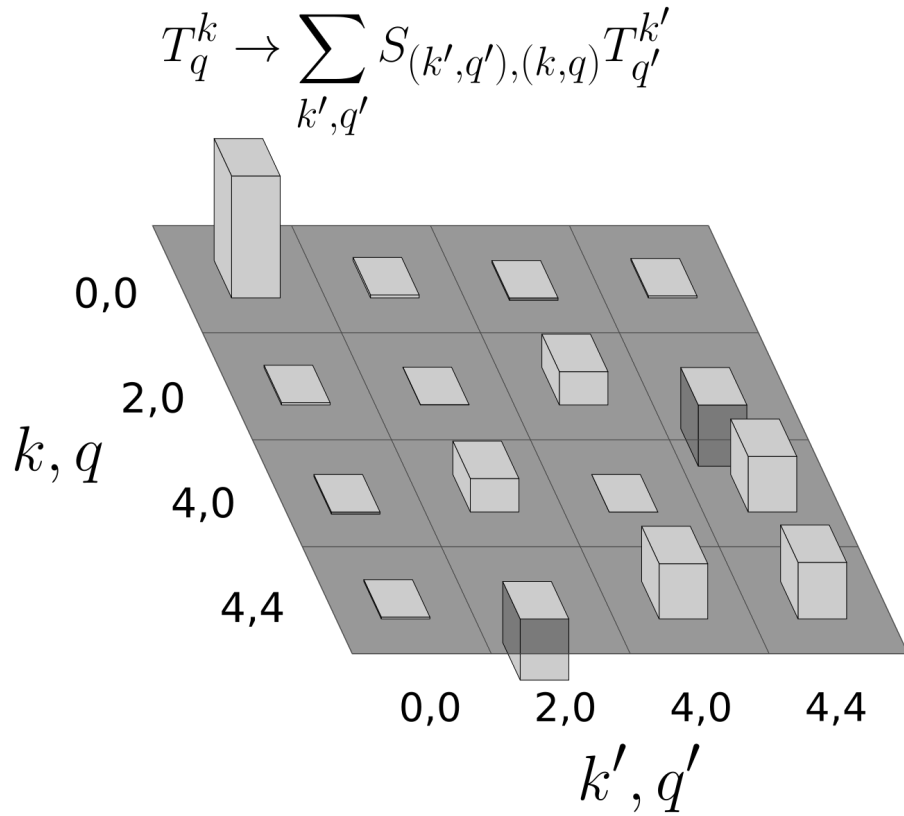
Figure 5.9: Graphical illustration of the scattering matrix $S_{(k',q'),(k,q)}$ relating incoming and outgoing multipoles of A_1 (totally symmetric) symmetry. Bars with negative height (below the semi-transparent plane) indicate negative amplitude.

predicted ionization scans, cartwheel pumping
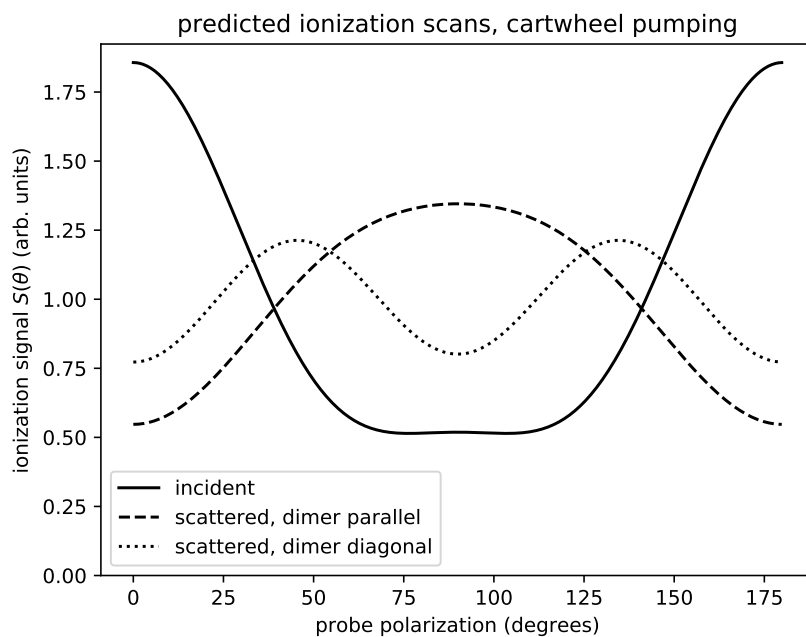
Figure 5.10: Predicted ionization signal $S(\theta)$ for cartwheeling molecules scattering from the Brenig-Pehlke potential. Corrugation of the potential energy in the ϕ coordinate leads to different ionization curves for the dimer-parallel and dimer-diagonal surface orientations.

Chapter Six: Results

6.1 Measurements

In this section we present data from a series of experiments measuring changes in the alignment of $j = 3$ H_2 molecules induced by scattering from the Si(100) surface. We begin by describing the procedure that allows us to locate the pumped molecules after they scatter from the surface. Following this measurements are shown which establish the effectiveness of the alignment preparation and detection. We then move on to the presentation of the scattered alignment measurements and the determination of the apparent moments characterizing the alignment.

6.1.1 Time of Flight Measurements

To identify the incident and scattered/reflected[1] molecules we measure the ionization signal as the pump-probe delay is increased, producing a time of flight curve. Refer to figure 6.1. At large probe-surface distances, the time of flight curve produces a single peak corresponding to those incident molecules excited by the pump laser. As the probe laser is brought closer to the surface, a distinct second peak at later pump-probe delays emerges which can be associated with the scattered molecules. Before alignment measurements are made, the surface is brought to within 1° of parallel with the probe laser. This reduces signal loss incurred from the spread in transit times due to molecules at different points along the probe's propagation ($\hat{k}$) direction. The probe laser is also brought as close as possible to the surface without introducing excessive overlap between incident and reflected molecules or deleterious scattering of laser light from the surface. This helps to reduce signal loss from the transit time spread due to velocity dispersion ($\approx 5\%$) in the incident molecules.

Figure 6.2 shows a time of flight profile for $j = 3$ pumped molecules probed on the O3 branch at conditions (probe↔surface angle/separation) typical for alignment measurements. The two traces shown were taken with all variables held fixed save for the probe half wave plate, which is oriented at angles $\theta_\parallel$ and $\theta_\perp$ corresponding to

---

[1] We use the two terms interchangeably throughout.
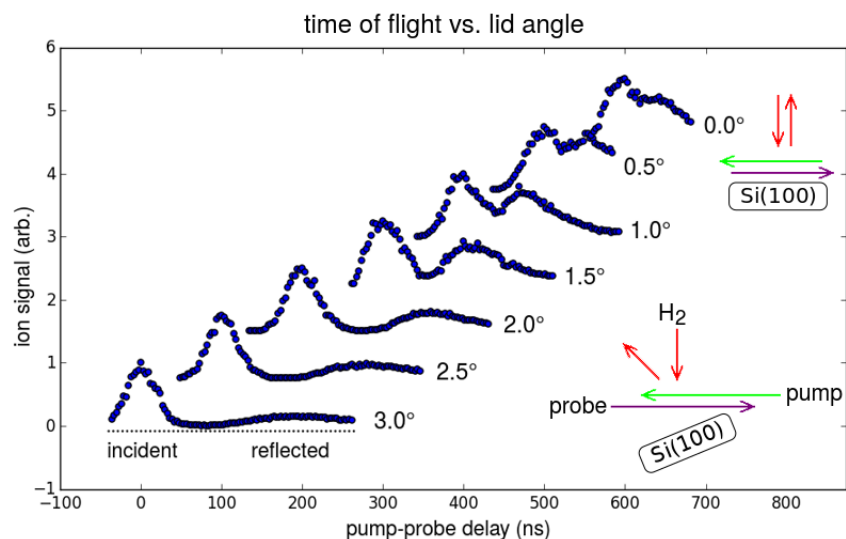
Figure 6.1: Evolution of time of flight profiles as surface is rotated to become parallel with pump and probe lasers. The molecules measured here have been excited by the pump laser to the $j = 1$ rotational level of the $\nu = 1$ excited vibrational state. This state has negligible background and was chosen for the purpose of illustration. At each lid angle, indicated to the right of each trace, the probe laser is translated as close as possible to the surface. As the angular mismatch is reduced (progressing from the lower traces upwards) the reflected peak appears closer to the incident, narrows in width and increases in integrated intensity.

maximum ($\parallel$) and minimum ($\perp$) incident signal ($\theta_\parallel - \theta_\perp = 45°$). The vertical scale of the second trace has been adjusted to illustrate the identical shape and location of the incident peaks. We take this to show that no unintended deflections occur as the waveplate is rotated. That the scattered peaks have different heights indicate a change in the alignment upon scattering[2].

6.1.2   Half Wave Plate Scans

To obtain more detailed information about the influence of scattering on alignment we monitor ionization $S(\theta)$ at fixed pump-probe delay as the probe polarization θ is rotated. The relation between $S(\theta)$ and the ensemble alignment is worked out in section 4.7.

---

[2] These traces were obtained well after the most recent cleaning procedure (section 2.2.2) so the scattered alignment can not be said to reflect the interaction with the ideal Si(100) surface.
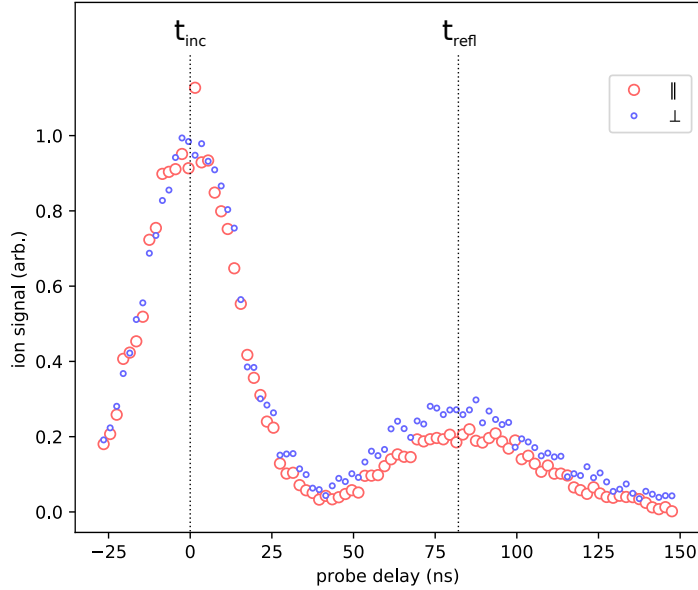
Figure 6.2: O3 time of flight profile. The $\parallel$ and $\perp$ traces were measured with the half wave plate orientated for maximum and minimum incident signal, respectively. The t_{inc} and t_{refl} markers indicate schematically the times at which half wave plate scans (section 6.1.2) are performed for the incident and scattered molecules respectively. For background subtraction we use delays t_{bg} (not shown) $\approx 50ns$ before t_{inc} or $\approx 1000ns$ after t_{refl}.

Before proceeding with discussion of the probe polarization scans at the alignment-sensitive O3 branch, we present in figure 6.3 a scan at Q0 as a sort of "control". The flatness (2% rms) demonstrates constancy in the beam's ellipticity with rotation of the half wave plate. [3] Combined with measurements at fixed half wave plate angle showing $> 100\times$ max:min ratio of reflection coeffecient from a Brewster plate, we can assert with confidence that the probe laser maintains pure linear polarization as it is rotated by the half wave plate over the full $180°$ range.

In figure 6.4 we evaluate the effectiveness of alignment and detection techniques. The plotted ionization $S(\theta)$ represents the contribution from the pumped incident $j = 3$ molecules. The background has been removed by taking at each angle the

---

[3] To see this we note that for any complex polarization vector $\hat{\epsilon}$ a basis $\hat{d}^1_0, \hat{d}^1_+, \hat{d}^1_-$ of spherical tensors can always be found where at least one of the circular components $\hat{\epsilon} \cdot \hat{d}^1_\pm$ vanishes. The magnitude of the remaining circular component goes as $\sqrt{1 - \cos 2\Delta}$, where Δ is the eccentricity of the polarization ellipse. Since circular polarized light can only contribute to the $|j = 0, m = 0\rangle \rightarrow |j = 0, m = 0\rangle'$ two-photon cross section via simualtaneous absorption of *opposite* handed photons, the nonzero circular component does not contribute either.
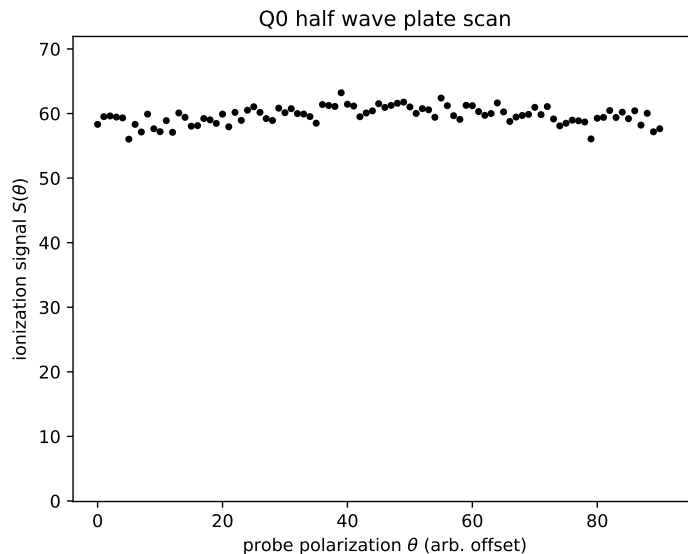
Figure 6.3: Probe polarization scan at the Q0 transition.

difference $S_{inc} - S_{bg}$ where S_{inc} is the signal obtained with the probe delay set at t_{inc} (figure 6.2), and S_{bg} the signal at some probe delay t_{bg} well before or well after the arrival of the pumped molecules, but in close enough temporal vicinity that the molecular beam density is unchanged[4].

The prediction is obtained by application of equation 4.59 to the case of strongly pumped molecules (equation 4.53). A correction due to hyperfine depolarization (section D) has also been applied. Aside from a vertical scaling factor, the only fitting parameter used was a horizontal offset to compensate for lack of knowledge of the half wave plate's fast axis[5]. The close agreement between observation and prediction gives confidence that both the alignment preparation and detection stages are working as expected.

A further necessary consistency check is shown in figure 6.5, where we have plotted two alignment measurements of the incident molecules, acquired under identical

---

[4] The values for this and all other polarization "runs" presented here are obtained by averaging of multiple "trials" (i.e. dataset = group of trials performed under identical conditions). Error bars similarly are derived by taking the standard deviation of results at each angle and dividing by the square root of the number of trials, i.e. measurements at fixed angle are presumed i.i.d. Each trial occurs within 30 minutes of the previous. Indivual trials are 20-40 minutes in duration and consist of rapid (3-5 minute) scans over the range of polarization angles with the intention of reducing error associated with long term drift (laser power/wavelength, molecular beam brightness, etc.).

[5] Though this, of course, could be determined by some Brewster-type measurement.

112

O3 ionization vs. probe polarization, 150 pump probe delay
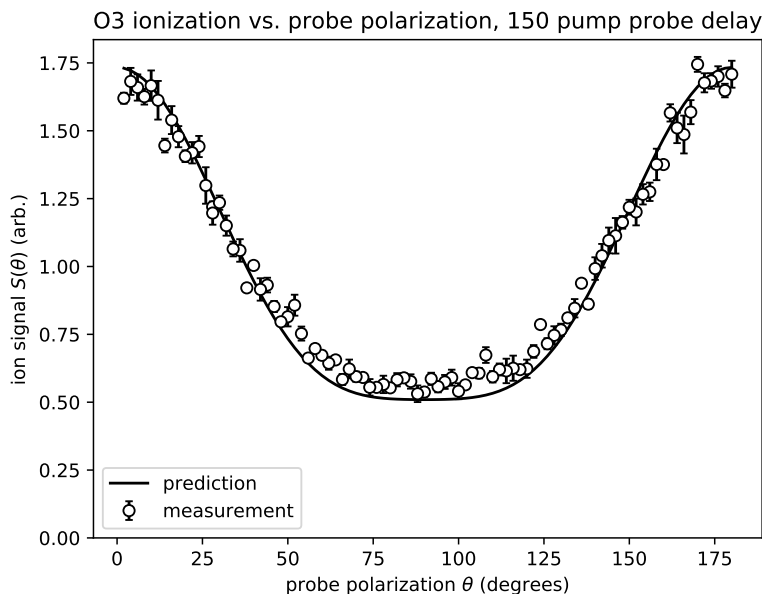
Figure 6.4: Alignment characterization. The x-axis has been offset (modulo 180°) for best agreement with prediction.

conditions save the pump polarizer orientations which differ by 90°. This 90° shift is clearly reflected in the ionization dependence $S(\theta)$, or in other words that the pumped molecules retain memory of the pump polarization. This check was perfomed for all measurements presented in this section.

6.1.3   Scattering Measurements

To ensure that we are studying the interaction of H_2 with the ideal Si(100) surface, the silicon sample is heated by a high temperature *in situ* anneal (section 2.2.2) and cooled slowly (1-2 minute) to room temperature before a measurement trial is started. Individual trial are limited to no more than 40 minutes, at which point the sampled is again cleaned and cooled down before beginning another trial. For all measurements we assume the surface temperature is between 300K and 400K. The cleanliness/well-orderedness of the surface and the orientation of its dimer rows (i.e. parallel or diagonal) are both verified using LEED (see section 2.2.3).

The results for all runs considered are plotted in figure 6.6. The incident and
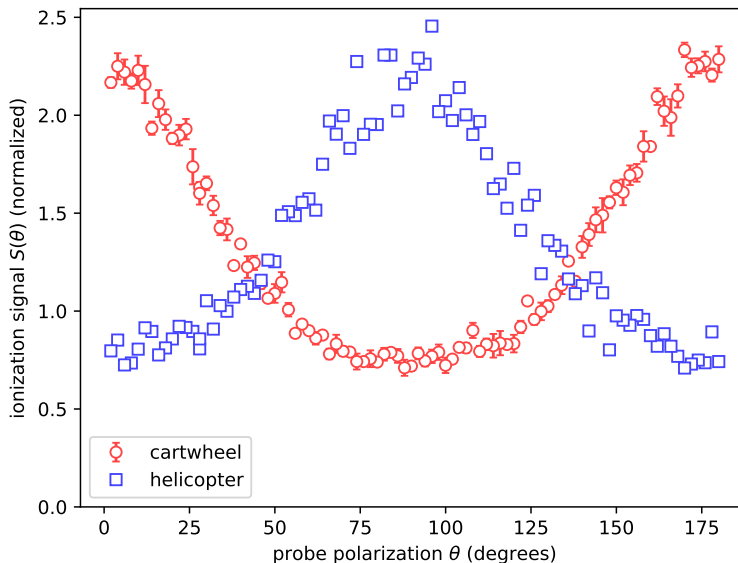
Figure 6.5: Probe polarization scans for the incident molecules pumped in the cartwheeling and helicoptering orientations. The cartwheeling trace is also shown in figure 6.4.

Helicopter data was assembled from single trial so error bars are omitted.

scattered data are fit to the following functional form:

$$S(\theta) = \sum_{k'=0,2,4} S_{k'} P_{k'} \left(\cos \theta' \right) \tag{6.1}$$

where $P_l(x)$ is the lth Legendre polynomial. For the incident molecules $\theta' = \theta - \theta_o$, where θ is the probe polarization with unknown offset. The parameter θ_o is fitting along with the apparent moments $S_{k'}^{(i)}$ to determine the offset. Ignoring for the moment the starred (*) runs, the apparent moments $S_{k'}^{(s)}$ for the scattered molecules are leaving θ_o fixed at the value determined for the incident molecules.

Runs A and C, however, exhibit a slight ($\approx 10°$) offset in the location of their symmetry axis. We suspect that this shift is unphysical as it would imply the existence of odd q moments in the scattered distribution which we do not expect to generate on account of the symmetry of the scattering potential.

This reasoning, one could argue, relies on somewhat strong assumptions concerning the ideality of the silicon surface structure. For the sake of completeness we include then, in addition to runs A and C, the runs A* and C* containing identical

114

data to their unstarred counterparts but differing in that a horizontal offset is included as a fitting parameter in the determination of the scattered apparent moments $S_{k'}^{(s)}$.

6.2   Discussion

6.2.1   Alignment Survival

A few general comments can be made regarding the results contained in table 6.1. First it is clear from inspection of the ratios $S_{k'}^{(r)}/S_{k'}^{(i)}$ that in all cases presented there is a modification of the alignment attributable to the molecule-surface interaction. Though even in free propagation there will be a decrease in alignment resulting from hyperfine depolarization (section D), we find the measured decrease in all cases well in excess of the expected $\approx 5\%$ ($\approx 20\%$) hyperfine correction to the quadrupole (hexadecapole) moments, respectively.

Concentrating momentarily on the dimer-parallel measurements we find somewhat better survival of the apparent quadrupole ($k' = 2$) moment for the cartwheels compared to the helicopters, though the spread in results from run to run make it difficult to conclude this decisively. The hexadecapole alignments are for all cases severely diminished upon scattering, and in case A (and A*) it is completely eliminated.

6.2.2   Dimer Diagonal Analysis

By analysis of the dimer-parallel results alone it is difficult to conclude much more. As discussed in section 4.7, the apparent moment $S_{k'}$ (equation 4.59) for a given k' contains contributions from not only the $k = k', q = 0$ multipole but from multipoles $k \geq k', q \neq 0$ as well. This means that two qualitatively different scattered density multiplets can give rise to identical apparent moments.

There are, however, for reasons discussed in section 5.4, strong constraints enforced by the surface symmetry on the moments that can be generated in specular scattering of a cylindrically symmetric ensemble impinging at normal incidence. Namely, the only cylindrically assymetric moments that the surface can induce are those with $q = 4$, and of the two ($k = 4, 6$) possessing this property only the $k = 4$ moment can be detected with our (2+1)REMPI process. Further, upon rotation by $45°$ the $k = 4, q = 4$ multipole is negated while the $q = 0$ moments are unaffected.

Schematically we could then take the difference of two polarization curves obtained with the dimers oriented at 0° and 45° to the laser propagation directions to isolate the contribution arising from the cylindrically assymetric component.

One requirement of course is that in both instances the incident ensemble alignment be identical. This implies that time elapsed between preparation of the alignment and scattering from the surface must be equal, otherwise the two ensembles would have undergone different degrees of hyperfine depolarization. For this reason if we are to make a comparison between the dimer-parallel and dimer-diagonal measurements we should select run A (or A*) as the dimer-parallel counterpart to the diagonal run E on account of the similarity in pump-probe delays (see t_{pi} and t_{is} in table 6.1).

To assess the similarity of the incident alignments we have plotted them together in figure 6.7. Though the precision of the dimer diagonal data is somewhat low we find the two curves to overlapped to a large extent and in rough agreement with the theoretical prediction. In light of this we consider the comparison of their scattered alignments justified.

The associated scattered polarization scans are shown superimposed in figures 6.8a and 6.8b. As explained earlier, runs A and A* are composed of the same measurements and differ in regards to the fitting technique applied to determine the apparent moments. The technique used in A* allowed for an polarization angle offset parameter θ_o different from the incident peak. This results in much better agreement with the expected form (equation (6.1)) but suffers from the unphysical shift. Ultimately which interpretation (A or A*) is to be preferred depends on the nature of the systematic error. Since this is of course unknown to us at this time, we analyze both cases, with the (hopeful) presumption that the true values lie between the two limiting cases.

From qualitative inspection we find that run A differs signficantly from the dimer-diagonal data, though the fit results are nearly identical. The situation for run A* is opposite – the agreement between the observations appears quite high while the fits reveal different ratios of quadrupole to hexadecapole moments between the parallel and diagonal dimer geometries.

In terms of the qualitative implications for the molecule-surface interaction, the run A result indicates negligible azimuthal corrugation, while from run A* might expect a significant ρ_4^{4+} component. Quantitatively, to extract the true multipole

116

moments, we find the values for the three moments $\rho_0^{2+}, \rho_0^{4+}, \rho_4^{4+}$ that best solve the following four equations:

$$S_{k'}^{(\beta)} = \frac{S_{k'k'}^0 \rho_0^{k'+} + \sigma(\beta) S_{k'4}^4 \rho_4^{4+}}{1 + \sigma(\beta) S_{k'4}^4 \rho_4^{4+}}$$

Where

- β is either $\parallel$ or $//$,

- $\sigma(\beta)$ is $+1$ $\beta =\parallel$ and -1 for $\beta = //$,

- $k' = 2, 4$,

- the $S_{k'}^{(\beta)}$ are given by the fit results tabulated in table 6.1, where $\beta =\parallel$ corresponds to runs A or A* and $\beta = //$ corresponds to run E, and

- the $S_{k'k}^q$ are as defined in equation (4.57).

A weighted least squares fit is performed to determine the scattered moments $\rho_0^{2+}, \rho_0^{4+}, \rho_4^{4+}$ for the two cases considered here (i.e. runs A + E and runs A* + E). The results are shown in table 6.2. As expected from our inspection of figure 6.8, we find that the run A analysis yields a vanishing ρ_4^{4+} while the run A* analysis finds a negative ρ_4^{4+} within statistical signficance. A qualitative "goodness of fit" can be assessed by comparing the resulting fit predictions $\bar{S}_{k'}^{(\beta)}$ for the apparent moments to the measured apparent moments. In all instances the error bars are found to overlap.

Briefly we consider the possibility suggested by the case A analysis of negligible corrugation in the molecule-surface potential with the azimuthal rotational coordinate ϕ. The observed modification of the alignment might then be attributed to corrugation in the polar coordinate θ. However, unpublished observations made in our lab on the scattering of vibrationally excited $\nu = 1$ H_2 from Si(100) indicate no significant rotational (or vibrational) inelasticity. Considering only the rotational degrees of freedom this would imply then *no change* in the alignment for the cartwheels upon scattering, since each angular momentum eigenstate $|j, m\rangle$ could only expect to incur a phase shift upon collision, so that no change occurs in the associated density matrix.

In the absence then of both rotationally elastic $|j, m\rangle \rightarrow |j, m'\rangle, m' \neq m$ reorienting collisions and rotationally inelastic excitations/de-excitations, we are led to consider an m-dependent *diffraction* probability to explain our results. In this scenario

117

our scattered alignment would be found to differ from the incident by preferential scattering of some m states away from the specular direction where we position our probe beam. Measurements of the alignment at nonzero diffraction orders could be expected to shed light on this hypothesis.

We conclude the section with a presentation in figure 6.9 of the resulting bond angle probability distributions for the two cases analyzed. In particular we note the general smoothing out of both distributions from their incident form (figure 4.4). We can also compare the distributions to figure 5.8, the distribution calculated from cartwheels scattering from the Brenig-Pehlke distribution (section 5.5). Clearly our measurements do not support the model's prediction of strong variation in the bond angle distribution with the azimuthal coordinate.
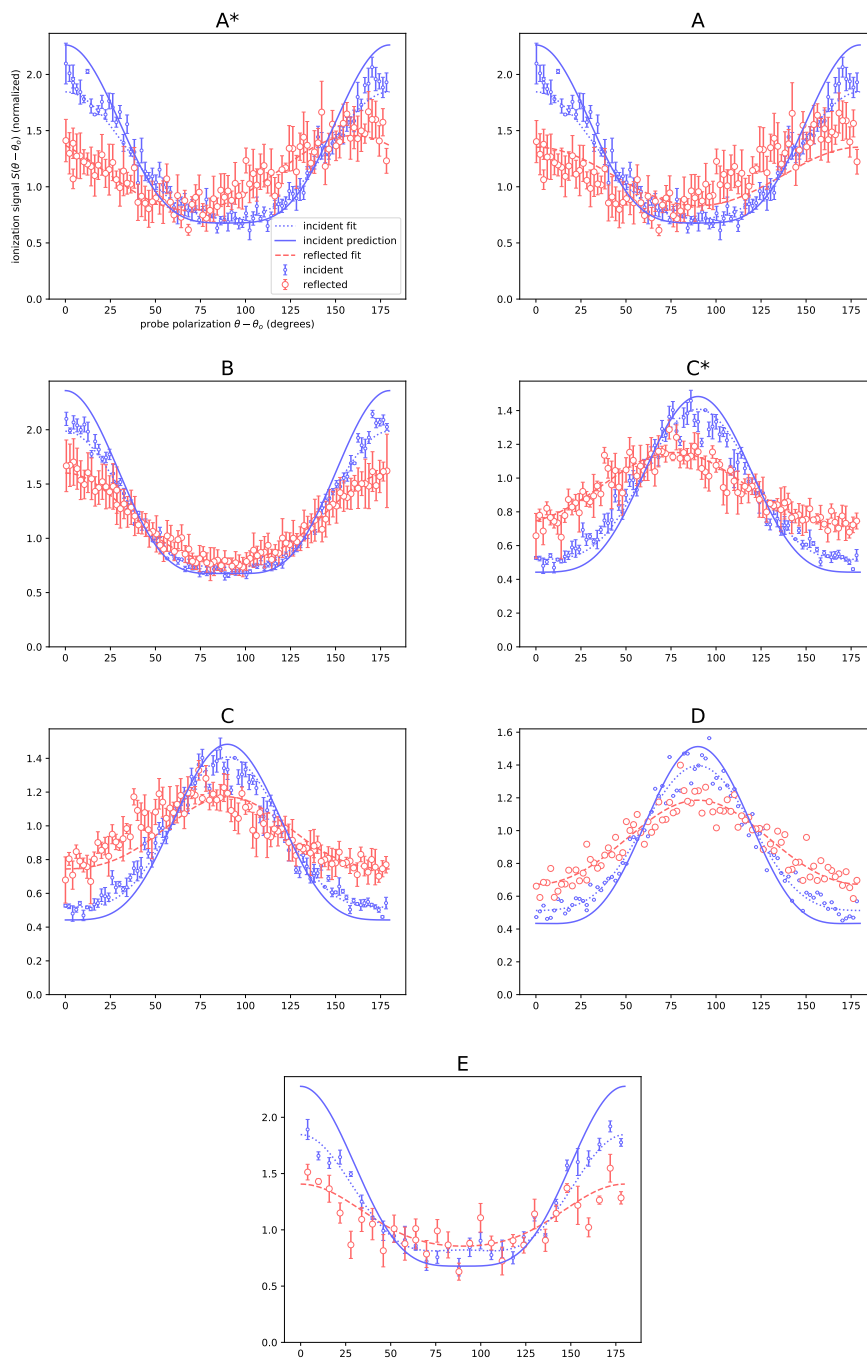
Figure 6.6: Polarization scans organized by run. See text for fitting procedure. Included along with the data and fits is the predicted curve for the incident molecules (see figure 6.4 and surrounding discussion). The incident and scattered curves are individually scaled to given an apparent moment $S_0^{(\alpha)} = 1$.

	Run						
	A*	A	B	C*	C	D	E
dimer	$\parallel$	$\parallel$	$\parallel$	$\parallel$	$\parallel$	$\parallel$	$/\!/$
alignment	C	C	C	H	H	H	C
t_{pi} (ns)	240	240	150	233	233	150	230
t_{is} (ns)	110	110	75	72	72	85	80
$S_2^{(i)}$	0.69	0.69	0.73	-0.670	-0.670	-0.66	0.57
$\delta S_2^{(i)}$	0.02	0.02	0.01	0.005	0.005	0.01	0.04
$S_2^{(r)}$	0.44	0.34	0.51	-0.29	-0.31	-0.35	0.34
$\delta S_2^{(r)}$	0.02	0.05	0.01	0.01	0.02	0.01	0.04
$\frac{S_2^{(r)}}{S_2^{(i)}}$	0.64	0.50	0.70	0.43	0.45	0.53	0.60
$\delta\frac{S_2^{(r)}}{S_2^{(i)}}$	0.04	0.07	0.02	0.01	0.02	0.03	0.09
$\frac{G_2(t_{pi}+t_{is})}{G_2(t_{pi})}$	0.93	0.93	0.96	0.95	0.95	0.95	0.95
$S_4^{(i)}$	0.16	0.16	0.26	0.19	0.19	0.17	0.28
$\delta S_4^{(i)}$	0.03	0.03	0.02	0.01	0.01	0.02	0.04
$S_4^{(r)}$	0.02	0.01	0.09	0.02	0.05	0.03	0.07
$\delta S_4^{(r)}$	0.03	0.05	0.01	0.01	0.02	0.02	0.06
$\frac{S_4^{(r)}}{S_4^{(i)}}$	0.12	0.06	0.35	0.10	0.26	0.14	0.24
$\delta\frac{S_4^{(r)}}{S_4^{(i)}}$	0.18	0.33	0.05	0.05	0.12	0.11	0.21
$\frac{G_4(t_{pi}+t_{is})}{G_4(t_{pi})}$	0.75	0.75	0.89	0.86	0.86	0.89	0.83

Table 6.1: Results for $j = 3$ aligned scattering, organized by run. For raw data and fits of results see figure 6.6. *dimer*: $\parallel$ and $/\!/$ refer to the dimer-parallel and dimer-diagonal geometries respectively. *alignment*: C and H refer to the cartwheeling and helicoptering incident alignments. t_{pi}: delay between pump laser and measurement of incident alignment. t_{is}: delay between measurement of incident and scattered alignments. $S_{k'}^{(\alpha)}$: k'th apparent moment (equation (4.59)) for the direction (α). The $S_0^{(\alpha)}$ are fixed at unity. A leading δ indicates the error in the parameter following. (i): incident. (r): reflected. $G_k(t)$: depolarization factor (section D). A $10°$ shift has been applied in the fitting procedure for the runs marked with asterisks (*) (see figure 6.6 for illustration and text body for explanation).
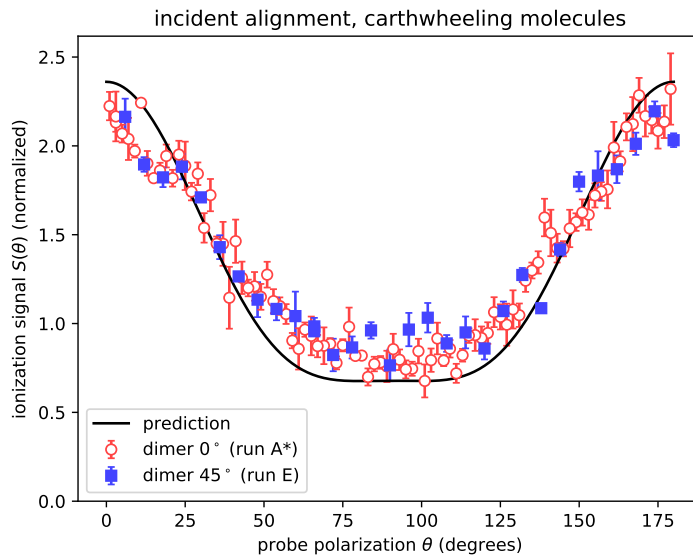
Figure 6.7: Comparison of the incident distributions for cartwheeling molecules incident on surfaces oriented in the dimer-parallel and dimer-diagonal orientation. The prediction is calculate from the same procedure described for figure 6.4.

(a)

(b)
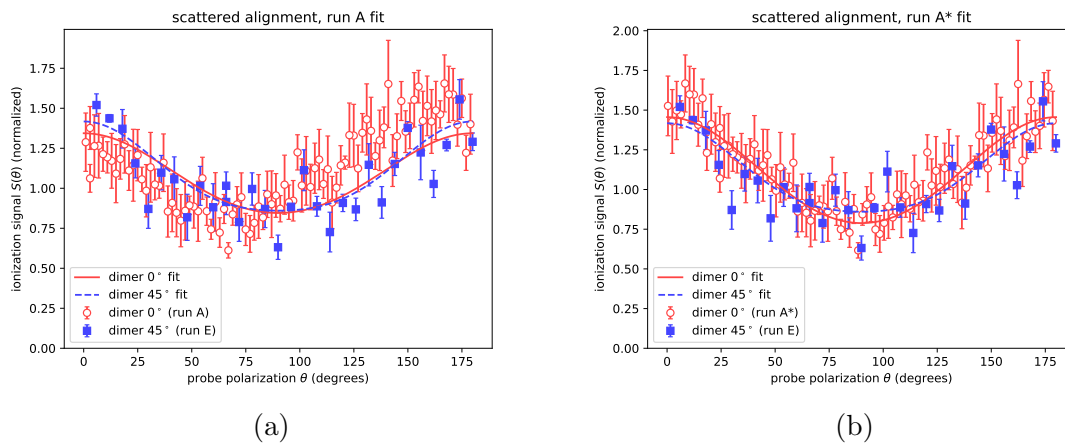
Figure 6.8: Comparison of the scattered alignments of incident cartwheeling molecules impinging on surfaces oriented in the dimer-parallel and dimer-diagonal orientation. Figure **(b)** differs from **(a)** in that a 10° shift has been applied to the dimer-parallel data to improve fit quality. Differences in the structure of the ionization curves $S(\theta)$ for the different orientations indicate azimuthal corrugation in the molecule surface potential.

	Runs	
	A + E	A* + E
ρ_0^{2+}	-0.34 ± 0.03	-0.40 ± 0.02
ρ_0^{4+}	0.04 ± 0.06	0.07 ± 0.04
ρ_4^{4+}	-0.03 ± 0.12	-0.22 ± 0.09
$\bar{S}_2^{(\|)}$	0.35 ± 0.04	0.44 ± 0.03
$\bar{S}_4^{(\|)}$	0.03 ± 0.04	0.02 ± 0.03
$\bar{S}_2^{(//)}$	0.33 ± 0.04	0.34 ± 0.03
$\bar{S}_4^{(//)}$	0.03 ± 0.04	0.07 ± 0.03

Table 6.2: Results from the analysis comparing scattered alignment for dimer-parallel and dimer-diagonal geometries. The multipole moments (section 4.4.3) ρ_q^{k+} are determined from a fitting procedure described in the text. The monopole moment ρ_0^0 is normalized to unity. The $\bar{S}_{k'}^{(\beta)}$ denote the best fit predictions for the apparent moments, where $\beta = \|$ corresponds to the dimer-parallel apparent moments (runs A or A*), while $\beta = //$ indicate the dimer-diagonal apparent moments (run E). These can be compared to the measured apparent moments $S_{k'}$ to assess goodness of fit.

Runs A + E   Runs A* + E
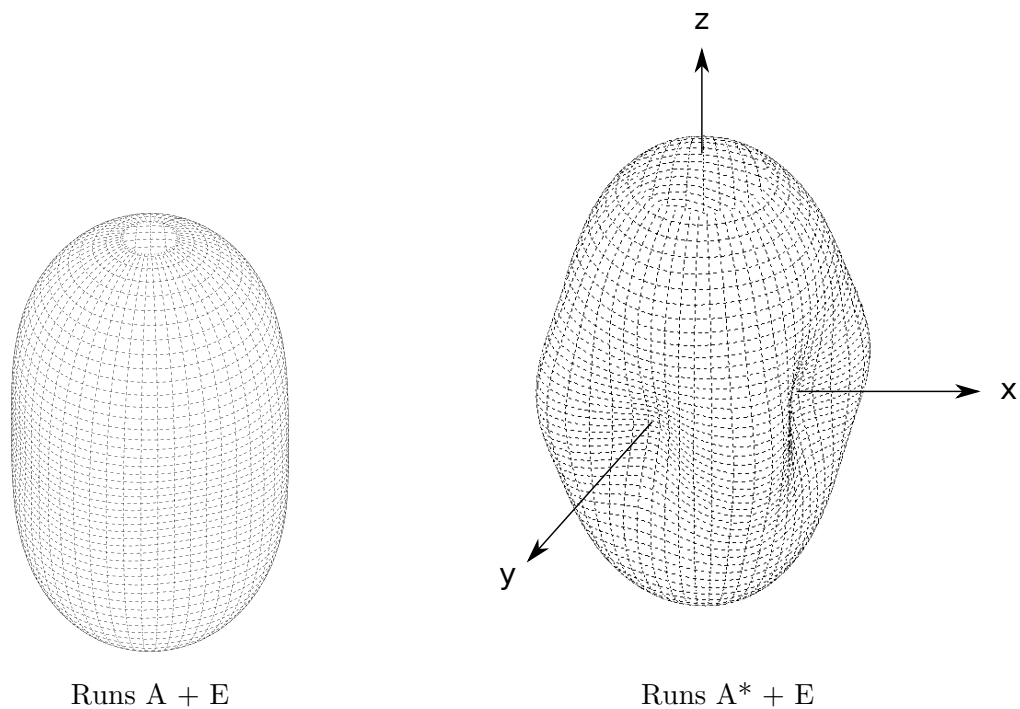
Figure 6.9: Plots of the bond angle probability distributions derived from the analysis of scattering at different surface azimuthal orientations. The coordinate axes indicate the lab frame directions (section 4.6). The distributions shown are those expected for the dimer-parallel geometry. The dimer-diagonal bond angle distributions are obtained by a rotation by 45° about the z axis.

Appendix A: Coherences in Density Operator

In this section we justify the assertion made earlier in section 4.4 concerning the neglect of coherence terms $\rho_{nm,n'm'}$, $n \neq n'$ in the density operator. This simplification is applied (and so must be justified) at each discrete step in the experiment, i.e.

$$\text{SMB} \rightarrow \text{pump} \rightarrow \text{surface} \rightarrow \text{probe}$$

We proceed from the final stage to the initial.

Detection stage:

The final measurement performed on our ensemble is the net ionization yield, which is proportional to the trace of ρ^{ion} over the subspace of ionized states, where ρ^{ion} is the state of our ensemble after the probe pulse. Since the trace can be expressed as the restricted sum of the *diagonal* elements of the matrix $\rho^{\text{ion}}_{nm,n'm'}$ it is clearly indepedent of any coherences.

Probe stage:

As discussed in section 2.4, the probe laser pulse ionizes ground electronic state ($\equiv$ X) molecules via a three photon transition. Due to the resonant nature of the intermediate transition, analysis can be broken up into the initial two photon intermediate transition sending the scattered ensemble ρ^{sc} to $\rho^{\text{E,F}}$ (named after the intermediate E,F electronic state), and the final one photon ionizing transition sending $\rho^{\text{E,F}}$ to ρ^{ion}.

Ionization:

Ionization is only accessible to molecules excited to the E,F state by the initial two photon stage. Therefore the only coherences in $\rho^{\text{E,F}}$ that can contribute to trace over the ionized subspace of ρ^{ion} are between different rovibrational levels in the E,F state. However, because the bandwidth of the probe laser is much narrower than the separation between the X- or E,F-state energy levels, only one $X \leftrightarrow E, F$ pair of levels will in general be resonant. Therefore no coherences in $\rho^{\text{E,F}}$ are expected.

E,F state excitation:

A similar argument allows us to neglect any coherences in the scattered ensemble ρ^{sc} in the determination of $\rho^{\text{E,F}}$. As explained, we are only interested in the portion of $\rho^{\text{E,F}}$ spanned by outer products of E,F states, and for a given probe laser wavelength only one X-state rovibrational level is resonant with a rovibrational level in the E,F-

state. Therefore the only outer products necessary to consider are between states in that X-state rovibrational level, permitting neglect of any coherences in ρ^{sc}.

Scattering stage:

From scattering theory[62] it is known that a system beginning in an asymptotic state, i.e. an eigenstate of the hamiltonian obtained by neglecting the scattering potential, can only scatter into asymptotic states of equal energy [1]. For our situation this implies that coherences in the density operator ρ^{in} representing the ensemble impinging on the surface couple only to the coherences of the scattered density operator ρ^{sc}, which can be neglected as previously discussed.

Pump stage:

The pump stage transforms the ensemble ρ^{SMB} produced by the supersonic molecular beam (SMB) to the ensemble ρ^{in} impinging on the surface. As concluded in the previous section, coherences in ρ^{in} can be neglected.

Finally, it only remains to show that we can neglect coherence in the SMB ensemble ρ^{SMB}. This turns out to be precluded by the stochasticity of SMB generation. Though any given molecule in the SMB is expected to in general assume some superposition of energy eigenstates, the phase between amplitudes of two states in different energy levels is expected to be distributed uniformly, resulting in a coherence-free density operator.

Note however, that the same can not in general be said of the phases in two different states in the *same* energy level. It is well known[55] that the collisional dynamics of the supersonic expansion permit *alignment* of molecules, i.e. nonzero elements $\rho^{\mathrm{SMB}}_{nm,nm'}$, $m \neq m'$.

---

[1] This assumes a *static* surface. However, even if we include the possibility of the *inelastic* scattering, i.e. energy *transfer* from the surface to the molecule, we still arrive at the conclusion that coherences in the impinging ensemble can be neglected. Suppose the surface transfers energy to a molecule originating in the nth asymptotic energy level so that it ends up in the $\tilde{n}^{\mathrm{th}}$ asymptotic energy level. Such a process will not produce interference effects for an incoming state consisting of, say, a superposition $|j_n, m\rangle + |j_{\tilde{n}}, \tilde{m}\rangle$, since the inelastic scattering process necessarily places the state of the *surface* in a different (asymptotic) energy level than would any elastic process. Though the molecule may end up in the $\tilde{n}^{\mathrm{th}}$ energy level in both processes, the total system (molecule+surface) will be in distinguishable states and therefore no intererence can occur.

Appendix B: Derivation of Multipole Symmetries

B.1 Symmetry properties of the angular momentum eigenstates

For proper rotations the symmetry operations have the same behavior for the dimer-parallel and dimer-diagonal cases (for definitions of these terms see the introduction to chapter 5. In particular we have for the identity operation

$$O_e |j, m\rangle = |j, m\rangle$$

while for rotations about the quantization axis we have from equation (4.5) that

$$O_\pi |j, m\rangle = (-1)^m |j, m\rangle$$

and

$$O_{\pm \pi/2} |j, m\rangle = (\mp i)^m |j, m\rangle$$

In contrast with proper rotations, the action of the reflection symmetry operations on angular momentum eigenstates is not determined by the defining relations (4.2), (4.4) and must be worked out for the particular multiplet and dimer row orientation under consideration.

In the following we work out the dimer-parallel case. The dimer-diagonal case works out similarly, and the differences are discussed at the end of this appendix in section B.3.

In the chosen reference frame we associate with the operation O_b a coordinate transformation $y \to -y$ with x and z fixed, so that $\theta \to \theta' = \theta$ while $\phi \to \phi'$ where $\sin \phi' = -\sin \phi$ and $\cos \phi' = \cos \phi$ which implies $\phi' = -\phi$. Since the ϕ dependence of the spherical harmonics is fully contained in the factor $e^{im\phi}$ we find that

$$\begin{aligned}
\left(O_b Y_j^m\right)(\theta, \phi) &= Y_j^m (\theta, -\phi) \\
&= Y_j^{m*} (\theta, \phi) \\
&= (-1)^m Y_j^{-m}(\theta, \phi)
\end{aligned} \tag{B.1}$$

or in other words

$$O_b|j, m\rangle = (-1)^m |j, -m\rangle$$

and similarly

$$O_a|j, m\rangle = |j, -m\rangle$$

For the reflections about the diagonals we use the fact that $O_\pm = O_x O_{\pm\pi/2}$ that

$$O_\pm|j, m\rangle = (\mp i)^m |j, -m\rangle$$

B.2   Symmetry properties of the state multipoles

Since the state multipoles are angular momentum eigenstates in the vector space of operators we get the same behavior under proper rotations as we did for the $|j, m\rangle$, i.e.:

$$O_e T_q^k O_e^\dagger = T_q^k$$

as well as

$$O_\pi T_q^k O_\pi^\dagger = (-1)^q T_q^k$$

and

$$O_{\pm\pi/2} T_q^k O_{\pm\pi/2}^\dagger = (\mp i)^q T_q^k$$

while for the reflections we must explicitly calculate their transformation properties by expanding the state multipoles in terms of angular momentum eigenstates (equation (4.27)) and using the reflection properties of the angular momentum eigenkets stated

just above, i.e.

$$O_a T_q^k O_a^\dagger = O_a \sum_{m,m'=-j}^{+j} (-1)^{j-m'} c(j,m;j,-m'|k,q)|j,m\rangle\langle j,-m'|O_a^\dagger$$

$$= \sum_{m,m'=-j}^{+j} (-1)^{j-m'} c(j,m;j,-m'|k,q) O_a|j,m\rangle \left(O_a|j,-m'\rangle\right)^\dagger$$

$$= \sum_{m,m'=-j}^{+j} (-1)^{j-m'} c(j,m;j,-m'|k,q)|j,-m\rangle\langle j,+m'|$$

$$= \sum_{m,m'=-j}^{+j} (-1)^{j+m'} c(j,-m;j,+m'|k,q)|j,m\rangle\langle j,-m'| \tag{B.2}$$

$$(!) = \sum_{m,m'=-j}^{+j} (-1)^{j+m'}(-1)^k c(j,m;j,-m'|k,-q)|j,m\rangle\langle j,-m'|$$

$$= (-1)^k \sum_{m,m'=-j}^{+j} (-1)^{j-m'} c(j,m;j,-m'|k,-q)|j,m\rangle\langle j,-m'|$$

$$= (-1)^k T_{-q}^k$$

where in the line marked (!) we use the well known property

$$c(j_1,m_1;j_2,m_2|j_3,m_3) = (-1)^{j_1+j_2-j_3} c(j_1,-m_1;j_2,-m_2|j_3,-m_3)$$

. Similarly,

$$O_b T_q^k O_b^\dagger = (-1)^{k-q} T_{-q}^k$$

and finally

$$O_\pm T_q^k O_\pm^\dagger = (-1)^k (\pm i)^q T_{-q}^k$$

The above calculations establish that the state multipoles of fixed k and $|q|$ transform amongst themselves under the C_{4v} symmetry operations. To determine the symmetries contained in the $\pm q$ pairs, we construct their character table, shown in table B.1.

The rows in the table can be formed by appropriate sums of rows from the character table of the irreducible representations B.2. We find that

- $q = 0 \cong \begin{cases} A_1 & k \text{ even} \\ A_2 & k \text{ odd} \end{cases}$, else

128

class |q|	O_e	$O_{\pm\pi/2}$	O_π	O_{b}^{a}	$O_\pm$
0	1	1	1	$(-1)^k$	$(-1)^k$
1	2	0	-2	0	0
2	2	-2	2	0	0
3	2	0	-2	0	0
4	2	2	2	0	0
5	2	0	-2	0	0
6	2	-2	2	0	0

Table B.1: C_{4v} character table for the $T_{|q|}^{k} \equiv (T_{-q}^{k}, T_{+q}^{k})$ representations. Results apply to the dimer-parallel case.

- q odd $\cong E$, else

- $2q$ odd $\cong B_1 + B_2$, else

- $2q$ even $\cong A_1 + A_2$

For the reducible $T_{|q|}^{k}$ representations (i.e. even $q \neq 0$) we can determine the states of definite symmetry by applying a projection operators P_f to one of the T_q^k. The operators P_f project a vector onto the subspace of states of definite f symmetry, where f is an irreducible representation, and are constructed by the rule

$$P_f \equiv \sum_{g \in G} \chi_f(g) O_g$$

where χ_f is the character of the group operation g for the f irreducible representation.

class / irrep	O_e	$O_{\pm\pi/2}$	O_π	O_b^a	$O_\pm$
A_1	1	1	1	1	1
A_2	1	1	1	-1	-1
B_1	1	-1	1	1	-1
B_2	1	-1	1	-1	1
E	2	0	-2	0	0

Table B.2: C_{4v} character table for the irreducible representations (irreps).

For instance, to determine what vector in the $|q| = 4$ subspace is a state of definite A_1 symmetry we could take $q = +4$ and apply the projection operator P_{A_1}, giving

$$
\begin{aligned}
P_{A_1} T_4^k =& T_4^k + (-i)^4 T_4^k + (+i)^4 T_4^k + (-1)^4 T_4^k \\
& + (-1)^k (T_{-4}^k + (-1)^4 T_{-4}^k + (-i)^4 T_{-4}^k + (+i)^4 T_{-4}^k) \\
\propto & T_4^k + (-1)^k T_{-4}^k \\
\propto & \begin{cases} T_4^{k+} & k \text{ even} \\ T_4^{k-} & k \text{ odd} \end{cases}
\end{aligned}
\tag{B.3}
$$

from which we immediately obtain

$$
P_{A_2} T_4^k \propto \begin{cases} T_4^{k-} & k \text{ even} \\ T_4^{k+} & k \text{ odd} \end{cases}
\tag{B.4}
$$

and similarly for $T_{|2|}^k$:

$$P_{B_1} T_2^k = T_2^k - (-i)^2 T_2^k - (+i)^2 T_2^k + (-1)^2 T_2^k$$
$$+ (-1)^k (T_{-2}^k + (-1)^2 T_{-2}^k - (-i)^2 T_{-2}^k - (+i)^2 T_{-2}^k)$$
$$\propto T_2^k + (-1)^k T_{-2}^k \tag{B.5}$$
$$\propto \begin{cases} T_2^{k+} & k \text{ even} \\ T_2^{k-} & k \text{ odd} \end{cases}$$

and likewise

$$P_{B_2} T_2^k \propto \begin{cases} T_2^{k-} & k \text{ even} \\ T_2^{k+} & k \text{ odd} \end{cases} \tag{B.6}$$

The reduction of the $q = |6|$ representation is identical to the $|q| = 2$ case.

B.3   Dimer-Diagonal Case

The symmetries of the multipoles for the dimer-diagonal case can be obtained by a $45° = \frac{\pi}{4}$ rotation. Using again equation (4.5) we find that:

- the T_0^k are invariant, while

- for $q = 2$ or 6 we have $T_q^{k\pm} \rightarrow -T_q^{k\mp}$, i.e. $B_1 \leftrightarrow B_2$, and

- for $q = 4$ we have $T_q^{k\pm} \rightarrow -T_q^{k\pm}$ so that the symmetries are unchanged, and

- for q odd there is no change in the symmetry classification since the $\pm q$ together span a 2-dimensional irreducible representation.

so that the dimer-parallel and dimer-diagonal cases are related by the simple exchange $B_1 \leftrightarrow B_2$.

Appendix C: Iterative Solution to Time-Dependent Schrödinger Equation

Suppose we have a system evolving under a time dependent hamiltonian $H(t)$, and we are seeking a solution to the time-dependent Schrödinger equation:

$$i\hbar\partial_t|\psi(t)\rangle = H(t)|\psi(t)\rangle$$

Given an N-dimensional basis $|n\rangle$ we can decompose the hamiltonian into

- a diagonal component

$$H_o(t) := \sum_n^N h_n(t)|n\rangle\langle n|$$

  where

$$h_n(t) := \langle n|H(t)|n\rangle$$

  and

- an off-diagonal component

$$V(t) := \sum_{n',n=1}^N v_{n'n}(t)|n'\rangle\langle n|$$

  where

$$v_{n'n}(t) := (1 - \delta_{n'n})\,\langle n'|H(t)|n\rangle$$

so that

$$H(t) = H_o(t) + V(t)\ .$$

We then consider a perturbation expansion of the state vector

$$|\psi(t)\rangle = |\psi^{(0)}(t)\rangle + \lambda|\psi^{(1)}(t)\rangle + \lambda^2|\psi^{(2)}(t)\rangle + \ldots + \lambda^k|\psi^{(n)}(k)\rangle + \ldots$$

where we require at some initial time t_o that

$$|\psi^{(k)}(t_o)\rangle = \delta_{k0}|\psi_o\rangle$$

Treating $V(t)$ as a perturbation, i.e.

$$V(t) \to \lambda V(t)$$

and matching terms in the time-dependent Schrodinger equation of equal order in λ, we get an iterative set of equations for the coefficients $c_n^{(k)}(t) \equiv \langle n | \psi^{(k)}(t) \rangle$:

$$i\hbar \dot{c}_n^{(k)}(t) = h_n(t) c_n^{(k)}(t) + \sum_{n'} v_{nn'} c_{n'}^{(k-1)}(t)$$

This equation can be cast in the following integral form:

$$c_n^{(k)}(t) = e^{i\phi_n(t)} \left(\delta_{k0} c_n^o + (i\hbar)^{-1} \int_{t_o}^{t} dt' e^{-i\phi_n(t')} \sum_{n'} v_{nn'}(t') c_{n'}^{(k-1)}(t') \right)$$

where $c_n^o \equiv \langle n | \psi_o \rangle$

$$\phi_n(t) \equiv -\frac{1}{\hbar} \int_{t_o}^{t} dt' h_n(t')$$

To handle the $k = 0$ case we must set $c_n^{(-1)}(t) = 0$ so that we find

$$c_n^{(0)}(t) = e^{i\phi_n(t)} c_n^o$$

The solution as it is formulated here admits a simple interpretation in terms of the scattering processes we are trying to model. The kth term $|\psi^{(k)}(t)\rangle$ in the perturbation expansion of $|\psi(t)\rangle$ contains k factors of $V(t)$, the off-diagonal component of the hamiltonian. We can interpret $|\psi^{(k)}(t)\rangle$ then as the portion of the state arising from k distinct "scattering events", i.e. k transitions between the different $|n\rangle$. The minimum number of iterations $k_{\min}$ required to achieve convergence can then serve as a measure of how often the we say the state "collided" with the perturbation $V(t)$.

The diagonal term $H_o(t)$, in contrast, acts to shift the energy levels of the different $|n\rangle$. If for some n', n the transition frequency $\nu_{n'n}(t) \equiv \frac{h_{n'}(t) - h_n(t)}{h}$ matches the rate at which the perturbation $v_{n'n}(t)$ oscillates, then we expect a resonant enhancement in the scattering between the two states.

To validate the solution and illustrate its behavior we apply it to a two-state $(|+\rangle, |-\rangle)$ system subjected to a "Rabi-flopping" hamiltonian

$$H(t) = \begin{bmatrix} \hbar\omega_1 & \frac{1}{2}\hbar\Omega e^{-i\omega_2 t} \\ \frac{1}{2}\hbar\Omega e^{i\omega_2 t} & -\hbar\omega_1 \end{bmatrix}$$

133

where the driving frequency is set to resonance, i.e. $\omega_2 = 2\omega_1$ and the Rabi frequency is set to a small fraction of the precession frequency, i.e. $\Omega = \frac{\omega_1}{10}$. The resulting evolution of the probabilities $|c_\pm(t)|^2$ for different iterations are shown in figure C.1. Note how multiple iterations are necessary to capture the characteristic Rabi oscillations.
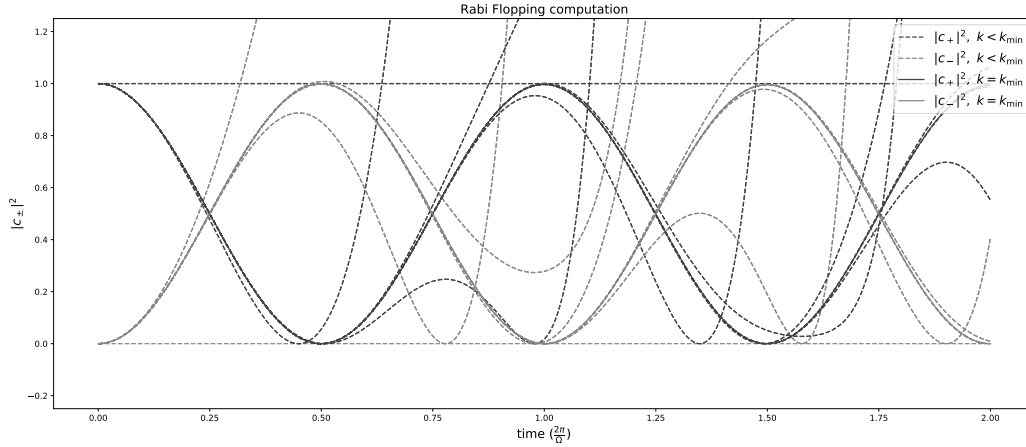

Figure C.1: Probabilities vs. time for two state system computed using perturbative scheme described in this section. All $k_{\min} = 20$ iterations are plotted to illustrate convergence. Curves corresponding to early iterations "peel off" from the true curve at earlier times than later iterations.

Appendix D: Hyperfine Depolarization

The hydrogen molecule contains, in addition to the rotational angular momentum which we have been denoting by $\vec{J}$, an angular momentum $\vec{I}$ associated with the combined spin of its nuclei. These angular momenta couple to one another[63], with the result that it is not in general $\vec{J}$ and $\vec{I}$ that are individually conserved, but rather their sum $\vec{F} \equiv \vec{J} + \vec{I}$ (see section 4.2).

To a high degree of accuracy the effect at low j can be considered to couple states of equal rotational angular momentum j. The population of a (see section 4.4) density multiplet ρ (i.e. ρ_0^0) is thus unaffected by the coupling but the remaining moments ρ_q^k will in general evolve. This phenomenon is known as *hyperfine depolarization.*

In our experiment we study H_2 molecules in the $j = 3$ rotational state. By the requirement of antisymmetry the odd states j rotational states have non-zero net nuclear spin[1] and will therefore depolarize. Rutkowski and Zacharias [64][2] have worked out the evolution $\rho_0^k(t) \equiv G^{(k)}(j,t)\rho_0^k(t = 0)$ of the cylindrically symmetric moments for arbitrary j and k assuming an initially isotropic distribution of nuclear spin. The "depolarization factor" $G^{(k)}(j,t)$ as applied to H_2 for $j = 3$ and times $0 < t < 500$ns are shown for the quadrupole ($k = 2$) and hexadecapole ($k = 4$) moments in figure D.1. The colored regions indicate time intervals over which the significant experiments events occur. From the figure we see that the spread in depolarizations from measurement to measurement is mild ($\approx 5\%$) for the quadrupole alignments and somewhat worse ($\approx 10 - 15\%$) for the hexadecapole.

---

[1] The even j states, however, are spin zero, and thus are immune to hyperfine depolarization.

[2] Note that Rutkowski [64] uses $\vec{N}$ to denote the rotational angular momentum, while here we use $\vec{J}$.
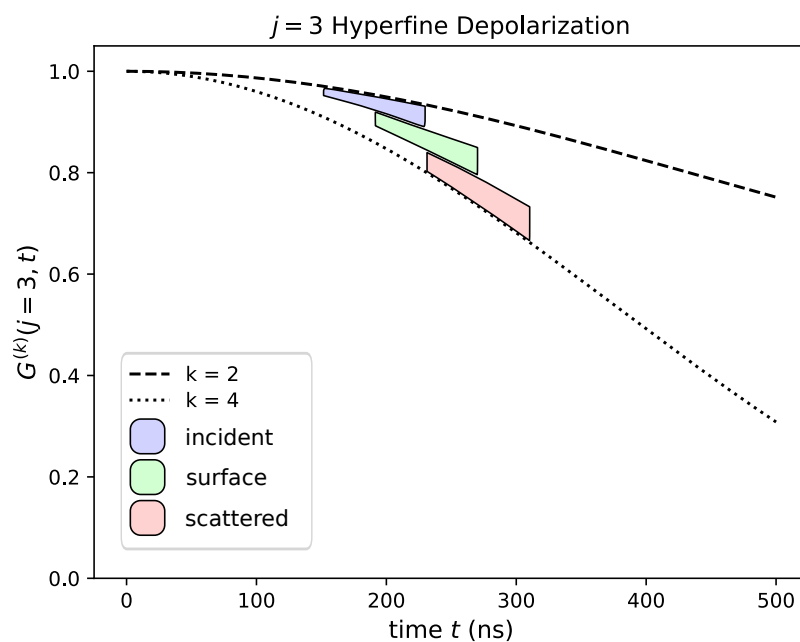
Figure D.1: The H_2 quadrupole ($k = 2$) and hexadecapole ($k = 4$) hyperfine depolarization factors for $j = 3$. The shaded regions indicate the spread in times between the pump and the probing of incident molecules and the following events: **blue**: measurement of incident alignment, **green**: impact of molecules with surface, **red**: measured of scattered alignment.

Bibliography

[1]   G. Scoles *et al.*, *Atomic and Molecular Beam Methods: Vol. 1*. Jan. 1998, ISBN: 0 -10-504280-8 (cit. on p. 2).

[2]   J. E. Pollard, D. J. Trevor, Y. T. Lee, and D. A. Shirley, "Rotational relaxation in supersonic beams of hydrogen by high resolution photoelectron spectroscopy," *The Journal of Chemical Physics*, vol. 77, no. 10, pp. 4818–4825, 1982, ISSN: 00219606. DOI: `10.1063/1.443722` (cit. on p. 5).

[3]   Q. Liu and R. Hoffmann, "The Bare and Acetylene Chemisorbed Si(001) Surface, and the Mechanism of Acetylene Chemisorption," *J. Am. Chem. Soc*, vol. 117, pp. 4082–4092, 1995. DOI: `10.1021/ja00119a024`. [Online]. Available: `https://pubs.acs.org/doi/10.1021/ja00119a024`. (cit. on pp. 7, 9).

[4]   M. Dürr and U. Höfer, "Stereochemistry on Si(001): Angular Dependence of H_2 Dissociation," *Physical Review Letters*, vol. 88, no. 7, p. 4, 2002, ISSN: 10797114. DOI: `10.1103/PhysRevLett.88.076107` (cit. on pp. 7, 97).

[5]   J. J. Boland, "Scanning tunnelling microscopy of the interaction of hydrogen with silicon surfaces," *Advances in Physics*, vol. 42, no. 2, pp. 129–171, Apr. 1993, ISSN: 0001-8732. DOI: `10.1080/00018739300101474`. [Online]. Available: `http://www.tandfonline.com/doi/abs/10.1080/00018739300101474` (cit. on p. 9).

[6]   J. Yoshinobu, "Physical properties and chemical reactivity of the buckled dimer on si(100)," *Progress in Surface Science*, vol. 77, no. 1-2, pp. 37–70, Nov. 2004, ISSN: 0079-6816. DOI: `10.1016/J.PROGSURF.2004.07.001`. [Online]. Available: `https://www.sciencedirect.com/science/article/pii/S0079681604000516` (cit. on p. 8).

[7]   M. Dürr and U. Höfer, "Molecular beam investigation of hydrogen dissociation on Si(001) and Si(111) surfaces," *Journal of Chemical Physics*, vol. 121, no. 16, pp. 8058–8067, Oct. 2004, ISSN: 00219606. DOI: `10.1063/1.1797052` (cit. on pp. 8, 11, 96).

[8] K. Hata, T. Kimura, S. Ozawa, and H. Shigekawa, "How to fabricate a defect free si(001) surface," *Journal of Vacuum Science & Technology A*, vol. 18, no. 4, pp. 1933–1936, 2000. DOI: `10.1116/1.582482`. eprint: `https://doi.org/10.1116/1.582482`. [Online]. Available: `https://doi.org/10.1116/1.582482` (cit. on p. 8).

[9] S. Y. Guo, "Dissociative attachment and reaction on silicon," dissertation, University of Toronto, 2015 (cit. on p. 8).

[10] G. O. Sitz, "Gas surface interactions studied with state-prepared molecules," *Reports on Progress in Physics*, vol. 65, no. 8, pp. 1165–1193, Aug. 2002, ISSN: 0034-4885. DOI: `10.1088/0034-4885/65/8/202`. [Online]. Available: `http://stacks.iop.org/0034-4885/65/i=8/a=202?key=crossref.b37b65642057ba19e671cc9e15596b69` (cit. on p. 13).

[11] G. O. Sitz and R. L. Farrow, "Pump-probe measurements of state-to-state rotational energy transfer rates in N2 (v=1)," *The Journal of Chemical Physics*, vol. 93, no. 11, pp. 7883–7893, 1990, ISSN: 00219606. DOI: `10.1063/1.459370` (cit. on pp. 15, 51).

[12] R. W. Minck, R. W. Terhune, and W. G. Rado, "Laser-stimulated raman effect and resonant four-photon interactions in gases h2, d2, and ch4," *Applied Physics Letters*, vol. 3, no. 10, pp. 181–184, 1963, ISSN: 00036951. DOI: `10.1063/1.1753840` (cit. on p. 16).

[13] N. Bloembergen, "The Stimulated Raman Effect," *American Journal of Physics*, vol. 35, no. 11, pp. 989–1023, Nov. 1967, ISSN: 0002-9505. DOI: `10.1119/1.1973774` (cit. on p. 16).

[14] K. P. Huber and G. H. Herzberg, "Nist chemistry webbook, nist standard reference database number 69," in, P. Linstrom and W. Mallard, Eds. 2019, ch. Constants of Diatomic Molecules (cit. on pp. 17, 22).

[15] R. W. Minck, E. E. Hagenlocker, and W. G. Rado, "Stimulated pure rotational raman scattering in deuterium," *Physical Review Letters*, vol. 17, no. 5, pp. 229–231, 1966, ISSN: 00319007. DOI: `10.1103/PhysRevLett.17.229` (cit. on p. 16).

[16] A. E. Siegman, *Lasers*. University Science Books, 1986 (cit. on p. 18).

[17] R. W. Boyd, *Nonlinear Optics, Third Edition*, 3rd. Orlando, FL, USA: Academic Press, Inc., 2008, ISBN: 0123694701, 9780123694706 (cit. on p. 18).

[18] M. N. R. Ashfold and J. D. Howe, "Multiphoton spectroscopy of molecular species," *Annual Review of Physical Chemistry*, vol. 45, no. 1, pp. 57–82, 1994. DOI: `10.1146/annurev.pc.45.100194.000421`. eprint: `https://doi.org/10.1146/annurev.pc.45.100194.000421`. [Online]. Available: `https://doi.org/10.1146/annurev.pc.45.100194.000421` (cit. on p. 18).

[19] M. Born and R. Oppenheimer, "Zur quantentheorie der molekeln," *Annalen der Physik*, vol. 389, no. 20, pp. 457–484, 1927. DOI: `10.1002/andp.19273892002`. eprint: `https://onlinelibrary.wiley.com/doi/pdf/10.1002/andp.19273892002`. [Online]. Available: `https://onlinelibrary.wiley.com/doi/abs/10.1002/andp.19273892002` (cit. on pp. 22, 35).

[20] J. I. Steinfeld, *Molecules and radiation : an introduction to modern molecular spectroscopy.* MIT Press, 1978, p. 348, ISBN: 9780262690591 (cit. on p. 22).

[21] T. E. Sharp, "Potential-energy curves for molecular hydrogen and its ions," *Atomic Data and Nuclear Data Tables*, vol. 2, no. C, pp. 119–169, Dec. 1970, ISSN: 10902090. DOI: `10.1016/S0092-640X(70)80007-9`. [Online]. Available: `https://www.sciencedirect.com/science/article/pii/S0092640X70800079` (cit. on p. 22).

[22] E. R. Davidson, *First excited $^1\Sigma_g^+$ state of H2. A double-minimum problem*, 1960. DOI: `10.1063/1.1731444` (cit. on p. 23).

[23] F. Duarte, "NARROW-LINEWIDTH PULSED DYE LASER OSCILLATORS," in *Dye Laser Principles*, Elsevier, 1990, pp. 133–183. DOI: `10.1016/b978-0-12-222700-4.50009-7` (cit. on p. 27).

[24] N. K. Sinha, "Normalised dispersion of birefringence of quartz and stress optical coefficient of fused silica and plate glass," *Physics and Chemistry of Glasses*, vol. 19, no. 4, pp. 69–77, 1978 (cit. on p. 30).

[25] "Physical Constants of Organic Compounds," in CRC Handbook of Chemistry and Physics, 100th Edition (Internet Version 2019), John R. Rumble, ed., CRC Press/Taylor & Francis, Boca Raton, FL. (cit. on p. 32).

[26] G. R. Darling and S. Holloway, "The dissociation of diatomic molecules at surfaces," *Reports on Progress in Physics*, vol. 58, no. 12, pp. 1595–1672, Dec. 1995. DOI: `10.1088/0034-4885/58/12/001`. [Online]. Available: `https://doi.org/10.1088%2F0034-4885%2F58%2F12%2F001` (cit. on p. 42).

[27] I. Estermann and O. Stern, "Beugung von molekularstrahlen," *Zeitschrift für Physik*, vol. 61, no. 1, pp. 95–125, Jan. 1930, ISSN: 0044-3328. DOI: `10.1007/BF01340293`. [Online]. Available: `https://doi.org/10.1007/BF01340293` (cit. on p. 34).

[28] G. J. Kroes and C. Díaz, *Quantum and classical dynamics of reactive scattering of H2 from metal surfaces*, Jul. 2016. DOI: `10.1039/c5cs00336a` (cit. on pp. 34, 35, 97, 99).

[29] A. M. Wodtke, "Electronically non-adiabatic influences in surface chemistry and dynamics," *Chem. Soc. Rev.*, vol. 45, pp. 3641–3657, 13 2016. DOI: `10.1039/C6CS00078A`. [Online]. Available: `http://dx.doi.org/10.1039/C6CS00078A` (cit. on p. 35).

[30] J. C. Polanyi and W. H. Wong, "Location of energy barriers. i. effect on the dynamics of reactions a + bc," *The Journal of Chemical Physics*, vol. 51, no. 4, pp. 1439–1450, 1969. DOI: `10.1063/1.1672194`. eprint: `https://doi.org/10.1063/1.1672194`. [Online]. Available: `https://doi.org/10.1063/1.1672194` (cit. on p. 36).

[31] R. R. Smith, D. R. Killelea, D. F. DelSesto, and A. L. Utz, "Preference for vibrational over translational energy in a gas-surface reaction," *Science*, vol. 304, no. 5673, pp. 992–995, 2004, ISSN: 0036-8075. DOI: `10.1126/science.1096309`. eprint: `https://science.sciencemag.org/content/304/5673/992.full.pdf`. [Online]. Available: `https://science.sciencemag.org/content/304/5673/992` (cit. on pp. 38, 39).

[32] A. JOSHI, L. DAVIS, and P. PALMBERG, "Chapter 5 - auger electron spectroscopy," in *Methods of Surface Analysis*, ser. Methods and Phenomena, A. CZANDERNA, Ed., Amsterdam: Elsevier, 1975, pp. 159–222. DOI: `https://doi.org/10.1016/B978-0-444-41344-4.50012-4`. [Online]. Available: `http://www.sciencedirect.com/science/article/pii/B9780444413444500124` (cit. on p. 38).

[33] D. R. Killelea, V. L. Campbell, N. S. Shuman, and A. L. Utz, "Bond-selective control of a heterogeneously catalyzed reaction," *Science*, vol. 319, no. 5864, pp. 790–793, 2008, ISSN: 0036-8075. DOI: `10.1126/science.1152819`. eprint: `https://science.sciencemag.org/content/319/5864/790.full.pdf`.

[Online]. Available: `https://science.sciencemag.org/content/319/5864/790` (cit. on pp. 38, 40).

[34] A. D. Johnson, S. P. Daley, A. L. Utz, and S. T. Ceyer, "The chemistry of bulk hydrogen: Reaction of hydrogen embedded in nickel with adsorbed ch3," *Science*, vol. 257, no. 5067, pp. 223–225, 1992, ISSN: 0036-8075. DOI: `10.1126/science.257.5067.223`. eprint: `https://science.sciencemag.org/content/257/5067/223.full.pdf`. [Online]. Available: `https://science.sciencemag.org/content/257/5067/223` (cit. on p. 38).

[35] H. L. Abbott, A. Bukoski, and I. Harrison, "Microcanonical unimolecular rate theory at surfaces. ii. vibrational state resolved dissociative chemisorption of methane on ni(100)," *The Journal of Chemical Physics*, vol. 121, no. 8, pp. 3792–3810, 2004. DOI: `10.1063/1.1777221`. eprint: `https://doi.org/10.1063/1.1777221`. [Online]. Available: `https://doi.org/10.1063/1.1777221` (cit. on p. 39).

[36] C. Crespos, H. F. Busnengo, W. Dong, and A. Salin, "Analysis of H2 dissociation dynamics on the Pd(111) surface," *Journal of Chemical Physics*, vol. 114, no. 24, pp. 10 954–10 962, Jun. 2001, ISSN: 00219606. DOI: `10.1063/1.1375153` (cit. on p. 45).

[37] M. Gostein and G. O. Sitz, "Rotational state-resolved sticking coefficients for H2 on Pd(111): Testing dynamical steering in dissociative adsorption," *The Journal of Chemical Physics*, vol. 106, no. 17, pp. 7378–7390, May 1997, ISSN: 0021-9606. DOI: `10.1063/1.473699` (cit. on pp. 46, 47).

[38] W. A. Diño, H. Kasai, and A. Okiji, *Orientational effects in dissociative adsorption/associative desorption dynamics of H2(D2) on Cu and Pd*, 2000. DOI: `10.1016/S0079-6816(99)00019-2` (cit. on p. 47).

[39] R. H. Fowler and E. A. Milne, "A note on the principle of detailed balancing," *Proceedings of the National Academy of Sciences*, vol. 11, no. 7, pp. 400–402, 1925, ISSN: 0027-8424. DOI: `10.1073/pnas.11.7.400`. eprint: `https://www.pnas.org/content/11/7/400.full.pdf`. [Online]. Available: `https://www.pnas.org/content/11/7/400` (cit. on p. 46).

[40] H. A. Michelsen, C. T. Rettner, D. J. Auerbach, and R. N. Zare, "Effect of rotation on the translational and vibrational energy dependence of the dissociative adsorption of D2 on Cu(111)," *The Journal of Chemical Physics*, vol. 98, no. 10, pp. 8294–8307, 1993, ISSN: 00219606. DOI: 10.1063/1.464535 (cit. on p. 47).

[41] S. F. Shane, K. W. Kolasinski, and R. N. Zare, *Recombinative desorption of H2 on Si(100)-(2X1) and Si(111)-(7X7): Comparison of internal state distributions*, 1992. DOI: 10.1063/1.463228 (cit. on pp. 48, 49).

[42] D. Wetzig *et al.*, "Rotational Alignment in Associative Desorption of D2 ($v'' = 0$ and 1) from Pd (100)," *Physical Review Letters*, vol. 76, no. 3, pp. 463–466, 1996, ISSN: 10797114. DOI: 10.1103/PhysRevLett.76.463 (cit. on pp. 48–50).

[43] S. J. Gulding *et al.*, " Alignment of D 2 (v , J) desorbed from Cu(111): Low sensitivity of activated dissociative chemisorption to approach geometry," *The Journal of Chemical Physics*, vol. 105, no. 21, pp. 9702–9705, Dec. 1996, ISSN: 0021-9606. DOI: 10.1063/1.472979 (cit. on pp. 48–50).

[44] G. O. Sitz and R. L. Farrow, "Preparation and decay of alignment in n2 (v=1)," *The Journal of Chemical Physics*, vol. 101, no. 6, pp. 4682–4687, 1994. DOI: 10.1063/1.467457. eprint: https://doi.org/10.1063/1.467457. [Online]. Available: https://doi.org/10.1063/1.467457 (cit. on pp. 50, 51).

[45] M. Kurahashi and Y. Yamauchi, "Production of a single spin-rotational state [(J,M) = (2,2)] selected molecular oxygen ($3\Sigma g$ -) beam by a hexapole magnet," *Review of Scientific Instruments*, vol. 80, no. 8, 2009, ISSN: 00346748. DOI: 10.1063/1.3206299 (cit. on p. 51).

[46] ——, "Huge steric effects in surface oxidation of Si(100)," *Physical Review B*, vol. 85, no. 16, p. 161 302, Apr. 2012, ISSN: 1098-0121. DOI: 10.1103/PhysRevB.85.161302. [Online]. Available: https://link.aps.org/doi/10.1103/PhysRevB.85.161302 (cit. on pp. 52, 53).

[47] D. A. King and M. G. Wells, "Molecular beam investigation of adsorption kinetics on bulk metal targets: Nitrogen on tungsten," *Surface Science*, vol. 29, no. 2, pp. 454–482, Feb. 1972, ISSN: 0039-6028. DOI: 10.1016/0039-6028(72)90232-4. [Online]. Available: https://www.sciencedirect.com/science/article/pii/0039602872902324 (cit. on p. 53).

[48] B. L. Yoder, R. Bisson, P. Morten Hundt, and R. D. Beck, "Alignment dependent chemisorption of vibrationally excited CH 4(3) on Ni(100), Ni(110), and Ni(111)," *Journal of Chemical Physics*, vol. 135, no. 22, Dec. 2011, ISSN: 00219606. DOI: 10.1063/1.3665136 (cit. on pp. 52, 54).

[49] O. Godsi *et al.*, "A general method for controlling and resolving rotational orientation of molecules in molecule-surface collisions," *Nature Communications*, vol. 8, no. 1, p. 15 357, Aug. 2017, ISSN: 2041-1723. DOI: 10.1038/ncomms15357. [Online]. Available: http://www.nature.com/articles/ncomms15357 (cit. on pp. 53, 55).

[50] G. H. Condon E. U. & Shortley, "Angular momentum," in *The Theory of Atomic Spectra*. Cambridge University Press, 1935, ch. 3, p. 48 (cit. on p. 59).

[51] Vazirani, Umesh, *Hilbert spaces, tensor products*, 2019. [Online]. Available: http://www-inst.eecs.berkeley.edu/~cs191/sp05/lectures/lecture3.pdf (cit. on p. 60).

[52] J. J. Sakurai and J. Napolitano, "Theory of angular momentum," in *Modern Quantum Mechanics*, 2nd ed. Cambridge University Press, 2017, pp. 157–261. DOI: 10.1017/9781108499996.007 (cit. on p. 60).

[53] C. Eckart, "The application of group theory to the quantum dynamics of monatomic systems," *Rev. Mod. Phys.*, vol. 2, pp. 305–380, 3 Jul. 1930. DOI: 10.1103/RevModPhys.2.305. [Online]. Available: https://link.aps.org/doi/10.1103/RevModPhys.2.305 (cit. on p. 65).

[54] B. R. Judd, "Tensor algebra," in *Angular Momentum Theory for Diatomic Molecules*. Academic Press, Jan. 1975, ch. 1, pp. 1–25, ISBN: 978-0-12-391950-2. DOI: 10.1016/B978-0-12-391950-2.50004-9. [Online]. Available: https://www.sciencedirect.com/science/article/pii/B9780123919502500049 (cit. on p. 66).

[55] L. Vattuone *et al.*, "Interaction of rotationally aligned and of oriented molecules in gas phase and at surfaces," *Progress in Surface Science*, vol. 85, no. 1-4, pp. 92–160, Jan. 2010, ISSN: 0079-6816. DOI: 10.1016/J.PROGSURF.2009.12.001. [Online]. Available: https://www.sciencedirect.com/science/article/pii/S0079681609000781 (cit. on pp. 79, 125).

[56] W. R. Sanders and J. B. Anderson, "Alignment of molecular iodine rotation in a seeded molecular beam," *The Journal of Physical Chemistry*, vol. 88, no. 20, pp. 4479–4484, Sep. 1984, ISSN: 0022-3654. DOI: `10.1021/j150664a006`. [Online]. Available: `http://pubs.acs.org/doi/abs/10.1021/j150664a006` (cit. on p. 79).

[57] W. Brenig and E. Pehlke, "Reaction dynamics of H2 on Si. Ab initio supported model calculations," *Progress in Surface Science*, vol. 83, no. 5-6, pp. 263–336, 2008, ISSN: 00796816. DOI: `10.1016/j.progsurf.2008.06.001` (cit. on pp. 95, 98, 103).

[58] W. Brenig, A. Gross, and R. Russ, "Detailed balance and phonon assisted sticking in adsorption and desorption of H2/Si," *Zeitschrift für Physik B Condensed Matter*, vol. 96, no. 2, pp. 231–234, Jun. 1994, ISSN: 07223277. DOI: `10.1007/BF01313289` (cit. on p. 96).

[59] M. Dürr, M. B. Raschke, and U. Höfer, "Effect of beam energy and surface temperature on the dissociative adsorption of H2 on Si(001)," *Journal of Chemical Physics*, vol. 111, no. 23, pp. 10 411–10 414, Dec. 1999, ISSN: 00219606. DOI: `10.1063/1.480395` (cit. on p. 96).

[60] T. Matsuno, T. Niida, H. Tsurumaki, and A. Namiki, "Coverage dependent desorption dynamics of deuterium on Si(100) surfaces: Interpretation with a diffusion-promoted desorption model," *Journal of Chemical Physics*, vol. 122, no. 2, 2005, ISSN: 00219606. DOI: `10.1063/1.1829994` (cit. on p. 96).

[61] K. W. Kolasinski, S. F. Shane, and R. N. Zare, "Internal-state distribution of recombinative hydrogen desorption from Si(100)," *The Journal of Chemical Physics*, vol. 96, no. 5, pp. 3995–4006, 1992, ISSN: 00219606. DOI: `10.1063/1.461849` (cit. on pp. 96, 97).

[62] S. Weinberg, "General scattering theory," in *Lectures on Quantum Mechanics*, Cambridge: Cambridge University Press, 2015, pp. 282–324. DOI: `10.1017/CBO9781316276105.010` (cit. on p. 125).

[63] N. Ramsey, "Molecular beams," in. Oxford University Press, 1956, vol. 20, ch. 8 (cit. on p. 135).

[64] M. Rutkowski and H. Zacharias, "Depolarisation of the spatial alignment of the rotational angular momentum vector by hyperfine interaction," *Chemical Physics*, vol. 301, no. 2-3, pp. 189–196, Jun. 2004, ISSN: 0301-0104. DOI: 10.1016/J.CHEMPHYS.2004.01.009. [Online]. Available: https://www.sciencedirect.com/science/article/pii/S0301010404000308 (cit. on p. 135).